



UNIVERSIDAD NACIONAL  
AUTÓNOMA DE  
MÉXICO

**UNIVERSIDAD NACIONAL AUTÓNOMA DE MÉXICO**

---

---

**PROGRAMA DE MAESTRÍA Y DOCTORADO EN INGENIERÍA**

**FACULTAD DE QUÍMICA**

**HYDRODYNAMIC STUDY OF  
MULTIPLE-PHASE FERMENTATIVE  
SYSTEMS**

**T E S I S**

QUE PARA OBTENER EL GRADO DE:

**DOCTOR EN INGENIERÍA**

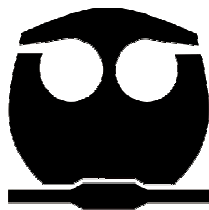
INGENIERÍA QUÍMICA – INGENIERÍA DE PROCESOS

P R E S E N T A :

**M. A. RENÉ SANJUAN GALINDO**

TUTOR:

DR. GABRIEL ASCANIO GASCA



México, D. F. Enero 2012



Universidad Nacional  
Autónoma de México



**UNAM – Dirección General de Bibliotecas**  
**Tesis Digitales**  
**Restricciones de uso**

**DERECHOS RESERVADOS ©**  
**PROHIBIDA SU REPRODUCCIÓN TOTAL O PARCIAL**

Todo el material contenido en esta tesis esta protegido por la Ley Federal del Derecho de Autor (LFDA) de los Estados Unidos Mexicanos (México).

El uso de imágenes, fragmentos de videos, y demás material que sea objeto de protección de los derechos de autor, será exclusivamente para fines educativos e informativos y deberá citar la fuente donde la obtuvo mencionando el autor o autores. Cualquier uso distinto como el lucro, reproducción, edición o modificación, será perseguido y sancionado por el respectivo titular de los Derechos de Autor.

## **JURADO ASIGNADO**

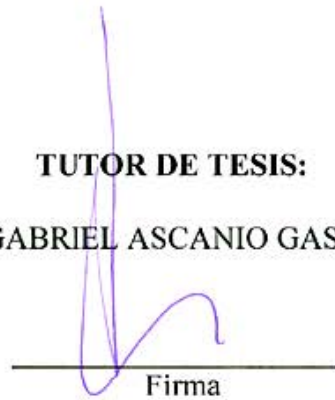
Presidente: DR. BARRAGÁN AROCHE FERNANDO  
Secretario DR. GIMENO SECO MIQUEL  
Vocal DR. FRADETTE LOUIS  
1er. Suplente: DR. ZENIT CAMACHO JOSÉ ROBERTO  
2do. Suplente: DR. ASCANIO GASCA GABRIEL

Lugar donde se realizó la tesis:

CIUDAD DE MÉXICO.

**TUTOR DE TESIS:**

GABRIEL ASCANIO GASCA



Firma

# *Agradecimientos*

*Con gran satisfacción presento esta tesis que resulta del esfuerzo diario y del interés por crecer como profesional y como persona. Expreso mi mayor agradecimiento a la Universidad Nacional Autónoma de México. Agradezco a Dios, de donde emana mi fuerza, mi esperanza, mi libertad y mi luz. Gracias por no agotar las oportunidades.*

Gracias a la Facultad de Química, institución participante en el Programa de Maestría y Doctorado en Ingeniería de la Universidad Nacional Autónoma de México (UNAM) por permitirme escalar un peldaño más en mi vida académica.

Gracias a la dirección del Dr. Gabriel Ascanio Gasca, adscrito al Centro de Ciencias Aplicadas y Desarrollo Tecnológico (CCADET) de la UNAM, gracias por la motivación, por su liderazgo y apoyo invaluable, gracias por ser visionario y estratégico.

Gracias al Consejo Nacional de Ciencia y Tecnología por haberme otorgado la beca de posgrado Número 210390. Agradezco el financiamiento de la DGAPA-UNAM a través del proyecto IN-117908.

Durante el desarrollo de mi formación doctoral, conté con la crítica de los investigadores Dr. Enrique Galindo y Dr. Alberto Tecante, adscritos al Instituto de Biotecnología (IBT) y a la Facultad de Química, respectivamente. Gracias a ellos aprendí que debo tener presentes los conceptos más elementales para avanzar en el proceso del aprendizaje. Gracias al Dr. E. Galindo por la confianza y por dejarme ser parte de su equipo de trabajo en el IBT.

En mi estancia en la *École Polytechnique de Montréal* (EPM) en Canadá tuve la guía y el invaluable apoyo del Dr. Philippe Tanguy y del Dr. Mourad Heniche, con ellos aprendí los conceptos más elementales de los procesos de mezclado, el modelado por computadora de fluidos en tanques agitados y el análisis crítico para la escritura de un artículo científico. También aprendí a sobrevivir en el invierno canadiense!

El Dr. Roberto Zenit del Instituto de Materiales (IM) de la UNAM me brindó su apoyo, y me incorporó a su equipo de trabajo. En el IM aprendí el proceso de visualización de fluidos y el manejo de datos. Gracias por enseñarme a ser autocrítico y persistente.

Conté con el apoyo y enseñanza académica de la Dra. Soledad Córdova del CCADET y del Dr. Gabriel Corkidi del IBT. Gracias por guiar mi desempeño en el IBT y por guiarme en el uso del equipo de visualización de alta velocidad y en el procesamiento de imágenes por computadora.

En el CCADET, tuve el apoyo técnico de: Dr. Enrique Soto, M. I. Benjamín Valera, M. C. Miguel Bazán, Dr. Antonio Hidalgo. Agradezco también el apoyo y gestión de Claudia, Lulú, Nancy, Jaime, Patricia Delgado, Jesús Ramírez y Rocío Sandoval.

Mi participación oral en el *XXIV Congreso de la Sociedad Mexicana de Instrumentación* fue posible gracias al financiamiento de la Coordinación de Posgrado de Ingeniería, gracias a la gestión de la Ing. María Antonieta Teyssier. Gracias también al apoyo recibido a través del CCADET, que hizo posible asistir y participar en el *61st* y *63rd Annual Meeting* de la *American Physics Society-Division Fluid Dynamics*.

Algunos de los colegas que me apoyaron y que no puedo dejar de citarlos:

- En el IBT: Ing. Axel Falcón, M. C. Martha Alicia, M. C. María Eugenia, M. C. Celia, M. C. Eliane Guevara, Lety, Dr. Carlos Peña, en la planta piloto de Ing. Mario, M. C. Raunel Tinnoco y Dr. Leobardo Serrano, así como la asistencia bibliográfica de S. Ainsworth.
- En el CCADET: M. C. Servando, Ing. Ricardo, Oscar Urrutia y personal del taller.
- Desde el Tecnológico de Tamaulipas: Ing. Amós.
- Del IM: M. C. Ernesto Mancilla, Dr. Carlos Palacios, Ing. Enrique Sandoval, Dr. Enrique Guzmán e Ing. Diego Samano.
- De la EPM: Ing. André Fontaine, Ing. Florence, M. C. Vincent Stobiac, Dr. Magda Brito, Dr. Lionel Mendez, Dr. Christian Rivera, Ing. Xavier, Diane Pimparé.
- En la Facultad de Química tuve el apoyo de Susana, de Bety López, Gloria García y de Paty Vargas.
- Desde el CIQA de Saltillo, Coa. tuve el apoyo bibliográfico de Brunilda.

Agradezco el apoyo de mi familia, amigos, directivos, maestros, compañeros, alumnos, y a quienes son todo ello. Ruego porque siempre existan sus nombres en mi recuerdo y porque siempre les guarde el aprecio que merecen.

Sin el apoyo y colaboración de todos ellos, este trabajo se habría demorado quizá no un día sino muchos años.

*Rene Sanjuan Galindo*

# Resumen

La motivación para desarrollar esta investigación fue el poco número de estudios que se han hecho para conocer los efectos hidrodinámicos en los elementos de una dispersión de características similares a los sustratos usados en fermentaciones líquidas. El objetivo es el estudio de la hidrodinámica que se produce en un recipiente cilíndrico utilizando un impulsor Scaba agitado a un número alto de Reynolds (*i.e.*  $Re = 24,000$ ) y a un consumo de potencia volumétrica de  $P/V_L = 0.46 \text{ W}\cdot\text{m}^{-3}$ . Mediante mediciones de velocimetría de imágenes de partículas (PIV por sus siglas en inglés) se determinaron el campo vectorial de la velocidad, el campo de vorticidad y la tasa de disipación de energía turbulenta que permitieron conocer los efectos que se producen en los elementos de una dispersión. La magnitud de la velocidad se encuentra en el rango  $0.05 \text{ m s}^{-1} < v < 0.5 \text{ m s}^{-1}$  y la máxima fluctuación de la velocidad en el centro del flujo del impulsor es  $v' \approx 0.45 \text{ m s}^{-1}$ . En el seno del líquido, el campo vectorial de la velocidad da evidencias de la formación clásica de dos remolinos característicos para el flujo de impulsores radiales. Estos remolinos representan zonas de baja presión y sugieren la segregación de los elementos en dispersión. En el centro del flujo del impulsor se forman dos vórtices de la misma magnitud ( $0.1 \text{ s}^{-1}$ ) pero con rotación en sentido opuesto. El número de flujo que se produce para este impulsor es  $N_Q = 0.46$ . Este parámetro, que puede compararse con el que reportan otros trabajos, explica el bombeo que se produce en el interior del líquido y que favorece la suspensión de la biomasa y la inmersión de las fases que por su baja densidad tienden a escaparse de la fase continua.

Los elementos usados en la dispersión son parte de fermentaciones líquidas; *i.e.* aire, aceite de Castor o biomasa (aglomerados de hongo), a bajas concentraciones (menos del 1%  $v/v$ ), se dispersaron en agua (uno a la vez). Se tomaron videos de alta velocidad como evidencia *in situ* a tiempo real de la dinámica de eventos como la formación de estructuras filamentosas

viscosas, el alargamiento de los elementos y las inestabilidades desarrolladas por los filamentos de aceite que son expulsados por el impulsor debido a la intermitencia de la intensidad del flujo del impulsor. Hasta ahora, la producción de filamentos no se ha documentado para tanques agitados; el desarrollo de proceso se identificó como la primera etapa de la dispersión del aceite y ocurre antes que se formen las gotas y que éstas saturen el sistema. Se propone una descripción del mecanismo de cuatro etapas para explicar la fragmentación de los elementos de la dispersión. Esta hipótesis se basa en el hecho de que el flujo que descarga el impulsor es altamente turbulento y contiene la mayor tasa de disipación, la velocidad fluctuante y su vorticidad influye en el rompimiento de las gotas de aceite, las burbujas de aire y los agregados de hongo.

Las gotas de aceite se rompen más fácilmente que las burbujas de aire debido a la relación que hay en la tensión interfacial (*i.e.*  $\sigma_{a-w}/\sigma_{o-w} = 3.4$ ). El diámetro promedio correspondiente a las burbujas de aire es de  $d_{32-Air} = 1.82$  mm. El tamaño de las gotas de aceite es menor y la precisión de su determinación requirió que se hicieran mediciones en dos perspectivas; en una visión global y en una zona local situada cerca de la pared del tanque. El diámetro promedio para las gotas de aceite es de  $d_{32-Oil} = 0.94$  mm en estado estacionario. El diámetro promedio permitió la estimación del área interfacial específica, *i.e.* para el sistema agua-gas  $a_{Air-H_2O} = 548$  m<sup>-1</sup> y para el sistema agua-aceite  $a_{Oil-H_2O} = 64$  m<sup>-1</sup>. El coeficiente global de transferencia de masa para la dispersión de gas-líquido fue  $k_L a = 0.007$  s<sup>-1</sup>.

El equilibrio entre las fuerza inerciales, de superficie y de tensión determinan la ruptura o la recuperación de los elementos mientras que el número adimensional de Weber define la ruptura o la estabilidad, el cual estuvo en el intervalo de  $0.15 < We < 3$  para las burbujas de gas y  $0.2 < We < 4$  para las gotas de aceite. Los valores más grandes corresponden a la zona en el flujo del impulsor, mientras que los valores más pequeños corresponden a los alrededores. En el flujo que descarga el impulsor, la máxima tasa de disipación de la energía de turbulencia es  $\varepsilon_{max} \approx 18$  m<sup>2</sup> s<sup>-3</sup>, mientras que en la vecindad de la pared del tanque  $\varepsilon \approx 0.6$  m<sup>2</sup> s<sup>-3</sup>.



# Abstract

This research was motivated by the scarce studies reported in the literature for the understanding of the hydrodynamic effects in the elements of a dispersion containing the substrates used in liquid fermentations. The goal of this work is the study of the hydrodynamics produced in a cylindrical vessel using a Scaba impeller agitated at high Reynolds number (i.e.  $Re = 24,000$ ), with a volumetric power consumption of  $P/V_L = 0.46 \text{ W}\cdot\text{m}^{-3}$ . The flow patterns and the turbulent flow properties like the velocity vector field, the vortex field and the turbulent energy dissipation rate were determined from the particle image Velocimetry measurements (PIV), which were useful for the understanding about the effects produced in the elements contained in dispersion. The velocity magnitude are in the range of the  $0.05 \text{ m s}^{-1} < v < 0.5 \text{ m s}^{-1}$  and the maximum velocity fluctuations are in the core of the impeller flow  $v' \approx 0.45 \text{ m s}^{-1}$ . In the liquid bulk, the velocity vector field evidences the formation of two classical eddies featuring the flow of radial impellers. These eddies represent low pressure zones and suggest the segregations of the elements in dispersion. In the core of the impeller flow two vortices of the same magnitude ( $0.1 \text{ s}^{-1}$ ) but rotating in different senses are formed. The pumping number produced by the impeller is  $N_Q = 0.46$ . This parameter, which can be compared with those values reported by other authors, explains the pumping produced inside the system that keeps the biomass in suspension as well as the immersion of the low density phases whose tendency is to become separated from the continuous phase.

The elements set in the dispersion are part of liquid fermentations; i.e. air, Castor oil or biomass (fungus pellets), at low concentration (less than 1% v/v), were dispersed in water (once at time). High-speed video recordings were taken to have evidences *in situ* in real time of the dynamic events like the formation of the viscous filamentous structures, the fluid elements stretching and the instabilities exhibited by the oil filaments expelled from the

impeller due to the periodicity of the intensity of the impeller flow. Until now, the filament generation and breakage has not been documented in stirred tanks; this process was identified as the first stage of oil dispersion and happens before oil drops form and saturate the system. It is proposed a description to explain a four-step mechanism by which the elements in the dispersion are fragmented. This hypothesis is supported by the fact that the flow located in the impeller discharge is highly turbulent and contains the major dissipation rate and its velocity fluctuations and vorticity influences breakup of oil drops, air bubbles and fungus pellets.

Oil drops are more easily fragmented than air bubbles due to the ratio in the interfacial tension (i.e.  $\sigma_{a-w}/\sigma_{o-w} = 3.4$ ). The corresponding mean diameter for the air bubbles is  $d_{32-Air} = 1.82$  mm. The oil drops size is lower and its accurate determination required measurements in two perspectives; a global view and a local zone located near the tank wall. The mean diameter for the oil drops is  $d_{32-Oil} = 0.94$  mm in the steady state. The average perimeter for the fungus pellets was 2.1 mm after stirring for 5 hours. The mean size allowed the estimation of the specific interfacial area, i.e. for the gas phase  $a_{Air-H_2O} = 548 \text{ m}^{-1}$  and for the oil phase  $a_{Oil-H_2O} = 64 \text{ m}^{-1}$ . The overall mass transfer coefficient for the gas-liquid dispersion was  $k_L a = 0.007 \text{ s}^{-1}$ .

The equilibrium between the inertial, superficial and tensile forces determines the fragmentation or recoiling of the elements, while the dimensionless Weber number, which defines the rupture or the stability, was found between  $0.15 < We < 3$  for the gas bubbles, and  $0.2 < We < 4$  for the oil drops. The largest values for the Weber number correspond to the zone of the impeller flow, while the smallest values correspond to the surroundings. In the impeller flow, the turbulence energy dissipation rate is  $\varepsilon_{max} \approx 18 \text{ m}^2 \text{ s}^{-3}$ , while in the neighborhood of the tank wall  $\varepsilon \approx 0.6 \text{ m}^2 \text{ s}^{-3}$ .

# Résumé

La motivation derrière cette recherche provient d'une lacune en connaissances des effets hydrodynamiques au sein d'une dispersion formulée avec des substrats utilisés en fermentation liquide. L'objectif de ce travail de recherche est l'étude de l'hydrodynamique à l'intérieur d'une cuve de mélange munie d'un agitateur Scaba pour un nombre de Reynolds élevé ( $Re = 24,000$ ). La consommation de puissance volumétrique est  $P/V_L = 0.46 \text{ W}\cdot\text{m}^{-3}$ . À partir des mesures obtenues avec la technique de velocimétrie par des images de particules (PIV acronyme en anglais), les champs de vitesse permettent de calculer les propriétés de la turbulence comme le champ de vorticité et le taux de dissipation de l'énergie turbulente pour mieux comprendre les effets produits à l'intérieur les éléments dispersés. L'amplitude de la vitesse est  $0.05 \text{ m s}^{-1} < v < 0.5 \text{ m s}^{-1}$  et la fluctuation maximale de la vitesse au cœur de l'agitateur est  $v' \approx 0.45 \text{ m s}^{-1}$ . Le champ de vitesse dans la phase liquide met en évidence la formation de deux tourbillons caractéristiques des écoulements produits par les agitateurs radiaux. Ces tourbillons représentent des zones de basse pression qui ségrégent les éléments de la dispersion. Dans l'écoulement situé au cœur de l'agitateur, deux vortex de même amplitude ( $0.1 \text{ s}^{-1}$ ) sont produits, mais de direction inverse. Le nombre de pompage de cet agitateur est  $N_Q = 0.46$ , le quel peut être confronté aux valeurs reportées par d'autres auteurs, explique le pompage créé à l'intérieur du volume liquide qui provoque la suspension de la biomasse et l'immersion des phases moins denses qui ont tendance à se séparer de la phase liquide.

Les éléments inclus dans la dispersion font partie des fermentations liquides; par exemple, l'air, l'huile de castor ou la biomasse (copeaux ou petites pelotes de champignons), à de faibles concentrations (moins de 1%  $v/v$ ), ont été dispersés dans l'eau (un à la fois). Des vidéos hautes vitesses ont été enregistrées pour expliquer la dynamique de formation des

structures filamenteuses visqueuses, l'étirement des éléments et les instabilités provoquées par l'expulsion de filaments d'huile qui sont causé par les fluctuations de l'intensité de l'écoulement provoquées par le mobile d'agitation. À ce jour, aucun travail n'a documenté la génération et la rupture de filaments en milieu agité. Ce processus est la première étape dans le procédé de dispersion et précède la formation de gouttes d'huile qui par la suite sature le système. Dans ce travail, un mécanisme en quatre étapes est proposé pour décrire la fragmentation des éléments de la dispersion. Cette hypothèse est soutenue puisque l'écoulement directement provoqué par l'agitateur, hautement turbulent, dissipe la majorité de l'énergie. De plus, les fluctuations de vitesse et les vortex présents influencent la fragmentation des gouttes d'huile, des bulles d'air et des copeaux.

Les gouttes d'huile se sont divisées plus facilement que les bulles d'air à cause du ratio entre les tensions interfaciales (i.e.  $\sigma_{a-w}/\sigma_{o-w}=3.4$ ). Le diamètre moyen correspondant aux bulles d'air est  $d_{32-Air} = 1.82$  mm. La taille des gouttes d'huile est plus petite et la mesure précise de sa taille a nécessité une mesure dans deux perspectives différentes; une complète et une seconde proche la paroi du réservoir. Le diamètre moyen des gouttes d'huile est  $d_{32-Oil} = 0.94$  mm en état stationnaire. Le diamètre moyen a permis l'estimation de la surface interfaciale, par exemple pour le système eau-gaz  $a_{Air-H_2O} = 548$  m<sup>-1</sup> et pour le système eau-huile  $a_{Oil-H_2O} = 64$  m<sup>-1</sup>. Le coefficient de transfert de masse de la dispersion eau-air est  $k_L a = 0.007$  s<sup>-1</sup>.

L'équilibre entre les forces inertielles et la tension de surface détermine le sort des éléments : soit leur division ou leur récupération. Le nombre adimensionnel de Weber indique la division ou la stabilité. Il a été obtenu  $0.15 < We < 3$  pour les bulles d'air et  $0.2 < We < 4$  pour les gouttes d'huile. La plus grande valeur des intervalles correspond à la zone d'expulsion de l'agitateur, tandis que la plus petite valeur correspond au restant de la cuve. Le taux de dissipation de l'énergie turbulente au cœur de l'agitateur est  $\varepsilon_{max} 18$  m<sup>2</sup> s<sup>-3</sup>, tandis qu'il est de  $\varepsilon \approx 0.6$  m<sup>2</sup> s<sup>-3</sup> au niveau de la paroi.

# *Contents*

<b>Agradecimientos</b>	<i>i</i>
<b>Resumen</b>	<i>iv</i>
<b>Abstract</b>	<i>vi</i>
<b>Résumé</b>	<i>viii</i>
<b>Contents</b>	<i>x</i>
List of Figures	<i>xv</i>
List of Tables	<i>xvii</i>
Nomenclature	<i>xviii</i>
Abbreviations	<i>xviii</i>
Variables	<i>xix</i>
Constants	<i>xx</i>
Dimensionless numbers	<i>xxi</i>
Units	<i>xxi</i>
Greek characters	<i>xxii</i>
Prefixes	<i>xxiii</i>
Subscripts	<i>xxiii</i>
<b>Introduction</b>	<b>1</b>
<b>Chapter I LITERATURE SURVEY</b>	<b>4</b>
<b>1.1 Study of multiphase systems</b>	<b>5</b>
<b>1.1.1 Multiphase systems</b>	<b>5</b>
<b>1.1.2 Fermentation broths, complex multiphase systems</b>	<b>7</b>
<b>1.2 Hydrodynamics in stirred tanks</b>	<b>9</b>
<b>1.2.1 Experimental and numerical studies on stirring</b>	<b>9</b>
<b>1.2.2 Nature of turbulence</b>	<b>11</b>
<b>1.2.3 Energy dissipation in turbulent flows</b>	<b>12</b>

1.2.4	Vorticity	13
1.3	Flow visualization in stirred tanks	13
1.3.1	Flow visualization techniques	13
1.3.2	Visualization of viscous structures and drops in stirred tank	14
1.4	Summary of the literature survey	15
1.4.1	Comparison of previous works	15
1.5	<b>Objective</b>	16
Chapter II	<b>MATERIALS and METHODS</b>	22
2.1	Studied dispersions	23
2.1.1	<i>Liquid-liquid dispersion</i>	23
2.1.2	<i>Gas-liquid dispersion</i>	23
2.1.3	<i>Gas hold-up</i>	24
2.1.4	<i>Biomass-liquid dispersion</i>	24
2.2	Experiment set-up	26
2.2.1	<i>Mixing equipment</i>	26
2.2.2	<i>Power consumption</i>	26
2.3	Video recordings and velocity measurements	28
2.3.1	<i>High speed video recordings</i>	28
2.3.2	<i>PIV measurements</i>	28
2.4	Reduced scale visualizations	28
2.4.1	<i>Individual drops visualized with high speed video</i>	28
2.4.2	<i>PIV measurements for the oil phase</i>	30
2.4.3	<i>Streamlines</i>	30
2.5	Variables of study	31
2.5.1	<i>Pumping characterization</i>	31
2.5.2	<i>Turbulence intensity</i>	31

2.5.3	<i>Vorticity</i>	32
2.5.4	<i>Sauter diameter</i>	32
2.5.5	<i>Interfacial area</i>	32
2.5.6	<i>Probability Density Function (PDF)</i>	33
2.5.8	<i>Volume-related liquid-side mass transfer coefficient (<math>k_{LA}</math>)</i>	34
2.5.9	<i>Turbulence energy rate dissipation</i>	34
2.5.10	<i>Kolmogorov micro-scale</i>	35
2.6	Dimensional analysis	35
2.6.1	<i>Reynolds number</i>	35
2.6.2	<i>"<math>g</math>" force</i>	35
2.6.3	<i>Froude number</i>	36
2.6.4	<i>Weber number</i>	36
Capítulo III	<b>HYDRODYNAMICS AND VISCOUS STRUCTURES FORMATION</b>	37
3.1	Flow field and oil filaments	38
3.1.1	<i>Velocity patterns</i>	38
3.1.2	<i>Oil dragging</i>	40
3.1.3	<i>Filamentous structures</i>	42
3.2	Turbulent flow effects	45
3.2.1	<i>Turbulence intensity</i>	45
3.2.2	<i>Vorticity field</i>	46
Chapter IV	<b>MASS TRANSFER AND FRAGMENTATION</b>	48
4.1	Stretching, breakage and mass transfer	49
4.1.1	<i>Air bubbles and distribution</i>	49



4.1.2	<i>Gas-liquid mass transfer coefficient</i>	52
4.1.3	<i>Time dependence of drop size</i>	52
4.1.4	<i>Biomass</i>	55
4.2	Mechanism to describe the particle size reduction	58
4.2.1	<i>Force competition</i>	58
4.2.2	<i>Turbulence energy dissipation rate</i>	59
4.2.3	<i>Mechanism to describe the elements size reduction</i>	61
<b>Chapter V</b>	<b>DROPS FLOW PATTERN</b>	<b>63</b>
5.1	Oil droplet dynamics	64
5.1.1	<i>Oil droplets velocity comparison</i>	64
5.1.2	<i>Oil phase velocity</i>	68
5.1.3	<i>Isotropy and energy dissipation rate in the tank wall region</i>	70
	<b>CONCLUSIONS AND FUTURE WORK</b>	<b>72</b>
	<b>BIBLIOGRAPHY</b>	<b>76</b>
	<b>APPENDIX</b>	<b>86</b>
A-1	Matlab programs	86
A-2	Statistical tools	89
A-3	Published work	90

## LIST OF FIGURES

<b>Figure 1.1</b>	Scheme of the mass transport process in a gas-liquid system according to the Two-film theory.	<b>7</b>
<b>Figure 1.2</b>	Performance and main features of liquid fermentations in stirred tank.	<b>8</b>
<b>Figure 1.3</b>	(a) Supersonic sound free-shear flows (Freund <i>et al.</i> , 2011) and (b) Symmetrical wake structure behind two uniformly rotating cylinders (Kumar <i>et al.</i> , 2011).	<b>11</b>
<b>Figure 1.4</b>	(a) Turbulent inertial regime. (b) Turbulent viscous regime. (Vankova <i>et al.</i> , 2007).	<b>13</b>
<b>Figure 2.1</b>	Procedure for the analysis of the fungus pellet shape (the bar length equals 2 mm). (a) A real image showing the fungus pellets. (b) Characterization of the pellet shapes as regular ellipses. (c) Major ( <i>a</i> ) and minor ( <i>b</i> ) radius of the ellipse considered for the perimeter estimation.	<b>25</b>
<b>Figure 2.2</b>	(a) Geometry and main dimensions of the impeller (mm), scheme no to scale. (b) Top view of the setup used for the capture of high-speed video and PIV. Nomenclature: <i>T</i> , tank diameter; <i>d<sub>I</sub></i> , impeller diameter; <i>c</i> , bottom clearance and <i>H</i> , liquid height.	<b>27</b>
<b>Figure 2.3</b>	(a) Experimental setup to investigate the instantaneous displacement for the individual oil droplets. (b) Circles traced with a continuous line represent the initial droplet position ( <i>t</i> <sub>1</sub> ) and pointed circles represent the droplet position at <i>t</i> <sub>2</sub> . Symbols: <i>v</i> , <i>X</i> , and <i>t</i> represent the velocity vector, the position vector and time, respectively. <i>r</i> , <i>ω</i> and <i>z</i> represent the radial, the angular and the axial coordinates, respectively. <i>θ</i> represents the tangential direction.	<b>29</b>
<b>Figure 2.4</b>	Orientation of the normal planes ( <i>rz</i> and <i>θz</i> ) to investigate the local hydrodynamics.	<b>30</b>
<b>Figure 2.5</b>	Interfacial area estimated for different diameters at different concentrations accordingly to Eq. 2.9.	<b>33</b>
<b>Figure 3.1</b>	(a) Velocity vector field and (b) Scalar field of velocity magnitude. <i>Re</i> = 24,000. Both cases represent the time average of the flow.	<b>39</b>

<b>Figure 3.2</b>	Axial velocity profiles along the $z$ axis for selected radii ( $r/R$ ). $v_{tip}$ and $H$ refer to the impeller tip velocity and the liquid maximum height, respectively.	<b>40</b>
<b>Figure 3.3</b>	Oil dragged from the surface to the impeller tips. ( $t_1 = 0$ ms, $t_2 = 195$ ms, $t_3 = 210$ ms and $t_4 = 385$ ms). In the last photograph, the mean velocity pattern governing the process is also shown.	<b>41</b>
<b>Figure 3.4</b>	Deformation process of a hairpin filament. Time difference between frames is 5 ms.	<b>42</b>
<b>Figure 3.5</b>	Schematic representation of the intermittent flow produced by the rotation of the impeller (top view).	<b>43</b>
<b>Figure 3.6</b>	(a) Normalized velocity of two filament points displaced in the plane $rz$ measured during 60 ms ( $v_{tip}$ refers to the impeller tip velocity, and $R$ represents the tank radius). (b) Velocity intermittence effect in the filament stability.	<b>44</b>
<b>Figure 3.7</b>	(a) Turbulence intensity and velocity fields. (b) Filament instability.	<b>45</b>
<b>Figure 3.8</b>	(a) Vorticity and velocity field, (b) Filament expelled by the impeller blades	<b>47</b>
<b>Figure 4.1</b>	(a) A typical image of air-water dispersion showing deformed bubbles and (b) PDF distribution of air bubble diameters. (c) Overlapped images showing air distribution produced during 1.5 s in a stirred tank at $Re = 24,500$ for an aeration rate of 0.5 vvm.	<b>51</b>
<b>Figure 4.2</b>	Image sequence of the deformation of an oil droplet near the impeller discharge.	<b>53</b>
<b>Figure 4.3</b>	(a) High-speed images of an oil-in-water dispersion produced in a stirred tank. Pictures were taken at $t_1 = 2$ min and $t_2 = 60$ min after the agitation process started. (b) PDF of drop diameter obtained at $t_1$ and $t_2$ .	<b>54</b>
<b>Figure 4.4</b>	(a) Gray-scaled images of the pellets in agitation taken at $t_1 = 15$ min, $t_2 = 60$ min and $t_3 = 300$ min after the agitation process started and (b) the corresponding PDF to compare the pellet perimeter in the three cases.	<b>57</b>
<b>Figure 4.5</b>	Free body diagram showing the presence of the forces acting in a stirred tank.	<b>59</b>

<b>Figure 4.6</b>	Turbulence energy dissipation rate in the impeller flow discharge.	<b>60</b>
<b>Figure 4.7</b>	Schematic representation of the process of object size reduction (1) A large object enters the high shear region. (2) The large object deforms and elongates. (3) The large object fragments. (4) Two objects of smaller size are produced.	<b>62</b>
<b>Figure 5.1</b>	(a) A typical image of the sequence obtained on-line for the study of the oil-water dispersion in a stirred tank. (b) Map to compare the drops size and the instantaneous velocities for each drop that crossed the zone in 0.4 s. (c) Scheme to explain the droplet distribution visualized in the map. Symbols: $z$ for the axial coordinate, $r$ for the radial coordinate, $\omega$ for the angular coordinate and $\theta$ for the tangential orientation.	<b>65</b>
<b>Figure 5.2</b>	Probability density function (PDF) versus the (a) drop diameter and (b) instantaneous velocities for individual oil droplets. Measurements were made in a local region at $Re = 24,500$ .	<b>66</b>
<b>Figure 5.3</b>	Overlapped images captured in dispersions agitated in different regimens: (a) Constant viscosity continuous phase. (b) Non-Newtonian dispersion (CMC solution).	<b>68</b>
<b>Figure 5.4</b>	Contour maps for the velocity magnitude and vector field for the oil phase in the planes: (a) $\theta z$ and (c) $rz$ . Streamlines for the oil phase velocity in the plane: (b) $z\theta$ and (d) $rz$ .	<b>69</b>
<b>Figure 5.5</b>	(a) Contour map for the velocity fluctuation ( $v'_{oil}$ ) and vector field for the oil phase. (b) Turbulence energy rate dissipation ( $\varepsilon_{oil}$ ) experienced by the oil phase.	<b>71</b>

## LIST OF TABLES

<b>Table 1</b>	Comparison of the published works prepared to investigate hydrodynamics in stirred tanks in single or multiple phases agitated with radial or axial impellers.	<b>17</b>
<b>Table 2</b>	Maximum values reported in the literature for the turbulent energy dissipation rate.	<b>60</b>

# NOMENCLATURE

## Abbreviations

<b>Abbreviation</b>	<b>Meaning</b>
2D	Two dimensions
CARPT	Computer-Automated Radioactive Particle Tracking
CCD	Charge-coupled device
CFD	Computational Fluid Dynamics
CMC	Carboxymethylcellulose
CPU	Central Process Unit
DNA	Deoxyribonucleic acid
DO	Dissolved Oxygen
FPIV	Fluorescent Particle Image Velocimetry
pfs	Frames per second
IBT	Instituto de Biotecnología
LDA	Laser Doppler Anemometry
LDV	Laser Doppler Velocimetry
NMR	Nuclear Magnetic Resonance
<i>P.</i>	<i>Pleorotus</i>
PBT	Pitched Blade Turbine
PDF	Probability Density Function
PIV	Particle Image Velocimetry
UDV	Ultrasonic Doppler Velocimetry
UNAM	Universidad Nacional Autónoma de México
USA	United States of America

## Variables

Symbol	Meaning	Unit
$\nabla$	Nabla operator	$m^{-1}$
$a$	Ellipse's major radius	m
$A, a$	Area	$m^2$
$b$	Ellipse's minor radius	m
$c$	Bottom clearance	m
$d_{32}$	Sauter diameter	m
$d_b$	Drop diameter	m
$d_b$	Bubble diameter	m
$d_I$	Impeller diameter	m
$e$	eccentricity	dimensionless
$H$	Liquid height	m
$H_g$	Height of the gassed liquid	m
$i$	Counting number, reference	dimensionless
$k$	Fluid consistency index	$Pa\ s^n$
$k$	Turbulent kinetic energy	$m^2\ s^{-2}$
$k_G$	Mass transfer coefficient for the gas phase	$m\ s^{-1}$
$k_L$	Mass transfer coefficient for the liquid phase	$m\ s^{-1}$
$k_{La}$	Overall volume-related liquid-side mass transfer coefficient	$s^{-1}$
$l$	Integral length scale	m
$N$	Rotational impeller speed	rps
$N_Q$	Pumping number	rps
$n$	Fluid thinning index	dimensionless
$n$	Number of blades	dimensionless
$P$	Power	W
PDF	Probability Density Function	dimensionless
$p$	Perimeter	m

pH	Hydrogen potential	dimensionless
$Q_G$	Volumetric gas flow rate	$\text{m}^3 \text{s}^{-1}$
$Q_k$	Volumetric gas flow rate in the $k$ direction	$\text{m}^3 \text{s}^{-1}$
$R, r$	Impeller radius	m
$r$	Radius	m
$r$	Radial coordinate	-
$T$	Tank diameter	m
$t$	Time	s
$V_L$	Liquid volume	$\text{m}^3$
$\mathbf{v}$	Velocity vector	$\text{m s}^{-1}$
$v_{tip}$	Impeller tip velocity	$\text{m s}^{-1}$
$v$	Velocity magnitude	$\text{m s}^{-1}$
$v_s$	Superficial gas velocity	$\text{m s}^{-1}$
$\bar{v}$	Average velocity	$\text{m s}^{-1}$
$u', v'$	Components of the mean fluctuating velocity	$\text{m s}^{-1}$
$\overline{v^2}$	Mean square spatial velocity fluctuation	$\text{m}^2 \text{s}^{-2}$
$v_z$	Axial velocity	$\text{m s}^{-1}$
$\mathbf{X}$	Position vector	m
$\mathbf{x}$	Undefined variable	-
$z$	Axial position	m
$z$	Axial coordinate	-

## Constants

Symbol	Meaning	Magnitude	Units
$A$	Constant used in Eq 2.14	1	dimensionless
$c$	Constant used in Eq 2.10	0.6	dimensionless
$D$	Oxygen diffusivity in water at 20°C	$2.11 \times 10^{-9}$	$\text{m}^2 \text{s}^{-1}$
$\rho_{H_2O}$	Water density	1000	$\text{kg m}^{-3}$

$\rho_{Oil}$	Oil density	960	$\text{Kg m}^{-3}$
$g$	Gravity acceleration	9.81	$\text{m s}^{-2}$
$\mu$	Water viscosity at 20°C	$10^{-3}$	Pa s
$\mu$	Castor oil viscosity at 20°C	$560 \times 10^{-3}$	Pa s
$\pi$	Pi number	3.1416	Dimensionless
$\sigma_{H_2O}$	Water surface tension at 20°C	0.072	$\text{N m}^{-1}$
$\sigma_{Oil}$	Oil surface tension at 20°C	0.039	$\text{N m}^{-1}$
$\sigma_{o-w}$	Oil-water interfacial tension at 20°C	0.021	$\text{N m}^{-1}$
$\sigma_{a-w}$	Oil-water interfacial tension at 20°C	0.072	$\text{N m}^{-1}$
$\nu$	Water kinematic viscosity	$1 \times 10^{-6}$	$\text{m}^2 \text{s}^{-1}$

### Dimensionless numbers

Symbol	Meaning
$Re$	Reynolds
$We$	Weber
$Fr$	Froude
" $g$ "	" $g$ " force

### Units

Symbol	Meaning
°C	Celsius
cm	Centimeters
L	Liter
m	Meters
N	Newton



min	Minutes
Pa	Pascal
rpm	Revolutions per minute
rps	Revolutions per second
s	Second
vvm	Gas flow per liquid volume
W	Watt

## Greek characters

Simbolo	Significado	Units
$\rho$	Density	$\text{Kg m}^{-3}$
$\Delta$	increment	dimensionless
$\varepsilon$	Specific local energy dissipation, Turbulent energy dissipation rate	$\text{m}^2 \text{s}^{-3}$
$\epsilon$	Hold-up	dimensionless
$\lambda$	Kolmogorov micro-scale	m
$\mu$	Mean value	variable
$\mu$	Dynamic viscosity	Pa s
$\varphi_V$	Volume of the dispersed phase	dimensionless
$\pi$	Pi number	dimensionless
$\omega$	Angular velocity	$\text{s}^{-1}$
$\omega$	Angular coordinate	dimensionless
$\omega$	Vorticity	$\text{s}^{-1}$
$\sigma^2$	Variance	variable
$\sigma$	Standard deviation	variable
$\sigma$	Surface tension, Interfacial tension	$\text{N m}^{-1}$
$\theta$	Tangential direction	-
$\nu$	Kinematic viscosity	$\text{m}^2 \text{s}^{-1}$

## Prefixes

Symbol	Meaning	Multiplication factor
k	Kilo	$10^3$
m	Mili	$10^{-3}$

## Subscripts

Symbol	Meaning
<i>av</i>	Average
<i>b</i>	Gas bubble
<i>G</i>	Gas phase
<i>L</i>	Liquid phase
<i>I</i>	Impeller
<i>max</i>	Maxima
<i>o</i>	Oil drop
<i>Q</i>	Volumetric flow
<i>s</i>	Superficial gas velocity
$\theta$	Tangential direction
<i>x,y,z</i>	Cartesian coordinates
<i>r, <math>\omega</math>, z</i>	Cylindrical coordinates
$\infty$	Infinite

# *I*NTRODUCTION

Dispersions are a kind of systems where several phases are in contact, by interacting between them and promoting mass and heat transfer. Dispersions of different nature are very common elsewhere. In the environment, pollutants are dispersed in the air due to pressure and temperature gradients. Water bodies like rivers or lakes are typical examples of wild dispersions. In industry, dispersions are commonly produced in stirred tanks. The elements of major interest to disperse are solid particles, gases or immiscible liquids. The mass transfer process is favored if the size of the elements in the dispersion is reduced as much as possible. For this purpose, several agitators have been proposed like Pitched Blade Turbines, Rushton turbines and Scaba impellers. Such impellers are usually operated in the turbulent regime, producing radial or axial flow and promoting inflow or outflow depending on the rotation sense. The use of baffles is needed to avoid the formation of vortex cavities and to pass from merely flow to vertical pumping.

The hydrodynamics produced in stirred tanks has been the center of many works, especially for single phase flows. Several authors have analyzed some macroscopic variables; for instance, they have focused in the measurement the power consumption, the effects of the impeller design, the effects of the rotational speed, mixing and circulation times, or the geometrical relationships between the impeller and the vessel. A number of works dealing with the comparison of the hydrodynamics produced by different type of impellers has been reported in the literature.

Advanced computational models have been developed to understand the flow field in the laminar, transitional or turbulent regimen. In these works, authors have tried to explain the flow behavior of certain in stirred tanks by using several concepts, which complicate the experimental work, for instance, the stretching efficiency, shear stress, shear rate or the particle tracking. Although the modeling of dispersed phases increases the number of equations and requires longer computational times, they have described the cavities formed in aerated flows, or the dispersion of the gas phase. Numerical models have been experimentally validated by using techniques based on the monitoring of radioactive particles, or the light reflected by brilliant trackers.

Several experimental techniques such as Laser Doppler Anemometry (LDA), Laser Doppler Velocimetry (LDV), Particle Image Velocimetry (PIV) or Nuclear Magnetic Resonance (NMR) have been used to determine velocity fields and the turbulence properties such as velocity fluctuations, vortex fields or the turbulence energy dissipation rate. Such properties explain the nature of the flow and play an important role in the elements of the dispersion; for instance, mixing at micro-scale, coalescence, vorticity, stretching, and fragmentation. Visualization techniques are useful tools recently applied in the study of dispersions. Photographic techniques have been used for exploring the flow behavior of dispersions at real time. It has been possible to determine the size of the fluid elements and other phenomena like the formation of complex drops, where phase inversion takes place.

Even though literature is vast for the study of single phase flows, the exploration of multiple-phase flows stills scarce. Fermentation processes are a special case of multiphase systems, because a gas phase, an oil phase, biomass and other substrates are dispersed in water. The physical properties of the organic phase used in biochemical processes are very different to those liquids already reported in the literature; for instance, they discuss with frequency aromatic oils or silicone oils. Such fluids are not used as substrates in fermentations processes; moreover, the viscosity of these liquids diverges from the viscosity of the organic liquids used in fermentation processes. Furthermore, they have studied oil-water dispersions at steady state; once drops are formed. The process where drops are formed is not documented.

This research exposes the formation of filamentous viscous structures and proposes the mechanism through which drops form and break. The present study deals with the stirring of a two-phase dispersion produced in a cylindrical vessel using a Scaba impeller agitated at high Reynolds number (i.e.  $Re = 24,000$ ). Air, Castor oil or biomass (fungus pellets) were dispersed in water (once at time).

The organization of this work is divided into six chapters distributed as follows.

The first chapter presents a brief summary of the previous research concerned with the study of the hydrodynamics generated in stirred tanks; it compares those works found in the literature prepared for radial or axial impellers and highlights the most common variables of interest and the

techniques utilized. As mentioned above, this chapter concludes that few works deal with the hydrodynamics study of those phases used as substrates in liquid fermentations.

The second chapter describes the experimental setup as well as the operating conditions and procedures followed along the study.

The third chapter presents the results obtained from the experimental work, basically the flow patterns, determined from PIV measurements, in the liquid bulk. Turbulent flow properties like the velocity fluctuation, the vorticity field and the turbulence energy dissipation rate are described. It is also described the possible relation of such variables with the formation of filamentous structures, which were registered with high speed video recordings. It was found that the flow located in the impeller discharge is highly turbulent, so as a consequence it contains the major dissipation rate.

The fourth chapter describes the rupture mechanism experienced by air bubbles, fungal clusters and oil drops. Velocity fluctuations and the vorticity field produce breakup of oil drops, air bubbles and fungus pellets. The evolution of the size of such elements is compared and the effect of the inertial, the interfacial and the fungal tensile forces are explored through the dimensionless Weber number. This parameter is defined as the ratio of the inertial forces to the superficial forces, which is useful to determine the elements stability or rupture. At the end of the chapter, it is proposed an explanation to describe the fragmentation mechanism in agreement with the turbulent flow properties. The turbulence energy rate dissipation was estimated using the dimensional analysis as a parameter involved in the mass transfer process in the micro-scale.

Chapter five was dedicated to describe the hydrodynamics generated in a small local region located in the neighborhood of the tank wall, where the impeller flow loses influence. Visual recordings were obtained using a magnification lens to explore small drops dimensions, which are difficult to consider in the global perspective. The flow structure in this zone is compared for two different rheological conditions. PIV measurements in this zone were made directly with the light reflected by the oil phase and produced the turbulence flow properties of the flow in this zone.

Conclusions, future work, bibliography and the appendix are presented in the final part of this thesis.

CHAPTER 1

*Literature  
survey*

This chapter explores the background concerned with the study of mechanically agitated systems. Fermentation liquid cultures are described by, considering these systems as a complex model of multiphase systems produced in stirred vessels. Several tools applied in the study of the hydrodynamics produced in agitated systems are mentioned, such as numerical simulations and visualization techniques. The most common variables monitored in published works are listed and the nature of turbulence is revisited considering its large influence on agitated dispersions. A comparison of those contributions related with the hydrodynamics of axial or radial impellers is presented. The objective of this research is mentioned at the end of this chapter.

## 1.1 Study of multiphase systems

*Multiphase systems are present everywhere, they are part of the wild wonders, they have a diversified nature but they still unexplored. Emulsions called our sense attention since childhood and they surprise us for all our life.*

### 1.1.1 Multiphase systems

Dispersions are conformed by a liquid phase enriched with gas, solid particles or another non-miscible liquid. Since men started to elaborate their meals, paintings or potions they tried to mix immiscible phases. Nowadays, dispersions are commonly produced in stirred tanks and they part in many industrial processes such as pharmaceuticals, biochemistry and food processing, among others. The energy supplied through the agitator induces a stretched flow, promotes the size reduction of the dispersion components, improves its distribution and promotes their contact (Armenante and Huang, 1992). Although dispersions offer good transfer of mass and energy, they are thermodynamically unstable and sometimes the use of surfactants is advised.

The mass transfer process is promoted by stirring, and depends on the physical properties of the fluids involved, temperature, pressure, concentration, agitation regimen, superficial gas velocity and the configuration of the reactor. The dispersion process of two non-miscible liquids, such as oil dispersed in water, or the dispersion of a gas phase in water is not trivial due to several factors, such as the density differences, low water capacity to dissolve the gas phase, the hydrophobic

behavior and buoyancy. Part of these difficulties is overcome by increasing the agitation regimen because the inflow generated by the impeller maintains such phases submerged and the flow forces promote both dispersion and fragmentation. The mass transfer process between the fluid elements and the continuous phase is a function of the gas content (hold-up), the oil fraction, the size distribution of these elements, the velocity at which they are transported and the good dispersion in the liquid bulk.

The gas-liquid mass transfer process is a limiting step in many biochemical processes. Some authors have studied the gassed-flow patterns in stirred vessels (Aubin *et al.*, 2004; Khopkar *et al.*, 2006; Bhattacharya *et al.*, 2007; Jahoda *et al.*, 2009), but the treatment of the mass transfer variables like the bubble size and the gas-liquid mass transfer coefficient were not exposed.

The Two-film theory predicts the overall mass transfer in gas-liquid dispersions ( $k_L a$ ). This theory considers the two mass transfer coefficients:  $k_G$  and  $k_L$ , for the gas phase and for the liquid phase, respectively. Both coefficients are defined for their respective diffusion within the film thickness depending upon the nature of the flow conditions, see Fig. 1.1 (Dumont and Delmas, 2003). However, the gaseous transport resistance ( $1/k_G$ ) is negligible compared with the liquid transport resistance ( $1/k_L$ ), which considers only the mass transfer liquid film coefficient  $k_L$  in the mass transfer analysis. The volume-related liquid-side mass transfer coefficient ( $k_L a$ ) relates the  $k_L$  coefficient with the area available for the mass transfer process ( $a$ ), which is determined by the size of the gas particles ( $d_b$ ). Several methods have been proposed to determine the  $k_L a$  (Zhao *et al.*, 1994; Zlokarnik, 2001; Alves *et al.*, 2004; Zieverink *et al.*, 2006; Clarke and Correia., 2008). Some methods are based on the extraction of samples, others have considered empirical equations correlated with the power input per unit volume and the gas superficial velocity; however, these methods discard the influence of certain factors like the size of the fluid elements in the dispersion. The use of such techniques may result in inadequate quantification of the particle sizes, except in the case of pure and dilute liquid-liquid systems. Photographic methods overcome in part, this weakness (Galindo *et al.*, 2000).



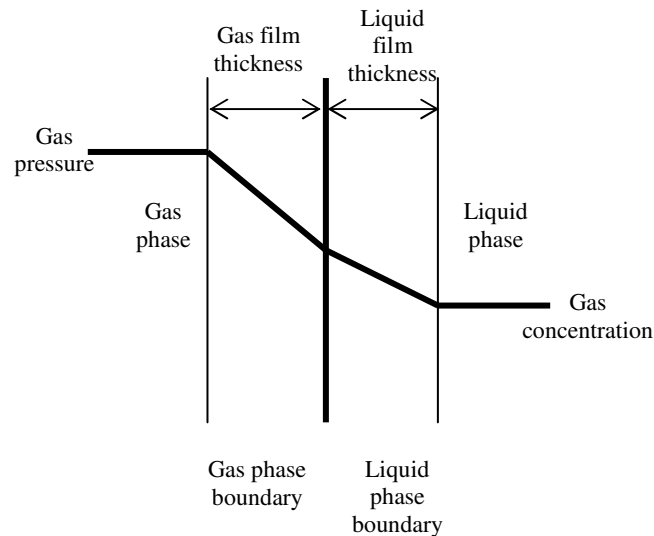


**Figure 1.1.** Scheme of the mass transport process in a gas-liquid system according to the Two-film theory.

### 1.1.2 Fermentation broths, complex multiphase systems

Fermentations carried out in bioreactors are an excellent example of multiphase systems. The number of products obtained by liquid fermentation has been considerably increased in the last decades; bacterial, insect, fungus, mammalian or plant cells as well as several multi-cellular microorganisms are grown *in-vitro* and *in-liquid* cultures. The products of interest include bioinsecticides, drugs, proteins, enzymes, vitamins, recombinant cell metabolites and many raw substances required in the human health care, fine and bulk chemicals, pharmaceutical, food, textiles, pulp and paper, minerals or energy sectors (Demain, 200).

A typical culture consists of collecting together a small fraction of nutritive substrates (solid phase) and a volume percentage of an organic oil (non-miscible liquid phase) in water or saline solutions, then, the microbial organism is inoculated. A stream of a gas phase is supplied (for example, air or pure oxygen in the case of aerobic organisms), then, the agitation speed and temperature are both controlled. The culture maturity is reached in periods that last up to 20 days (Sanjuan-Galindo, 2008). Fig. 1.2 shows a scheme of a fermentation process in a batch bioreactor.

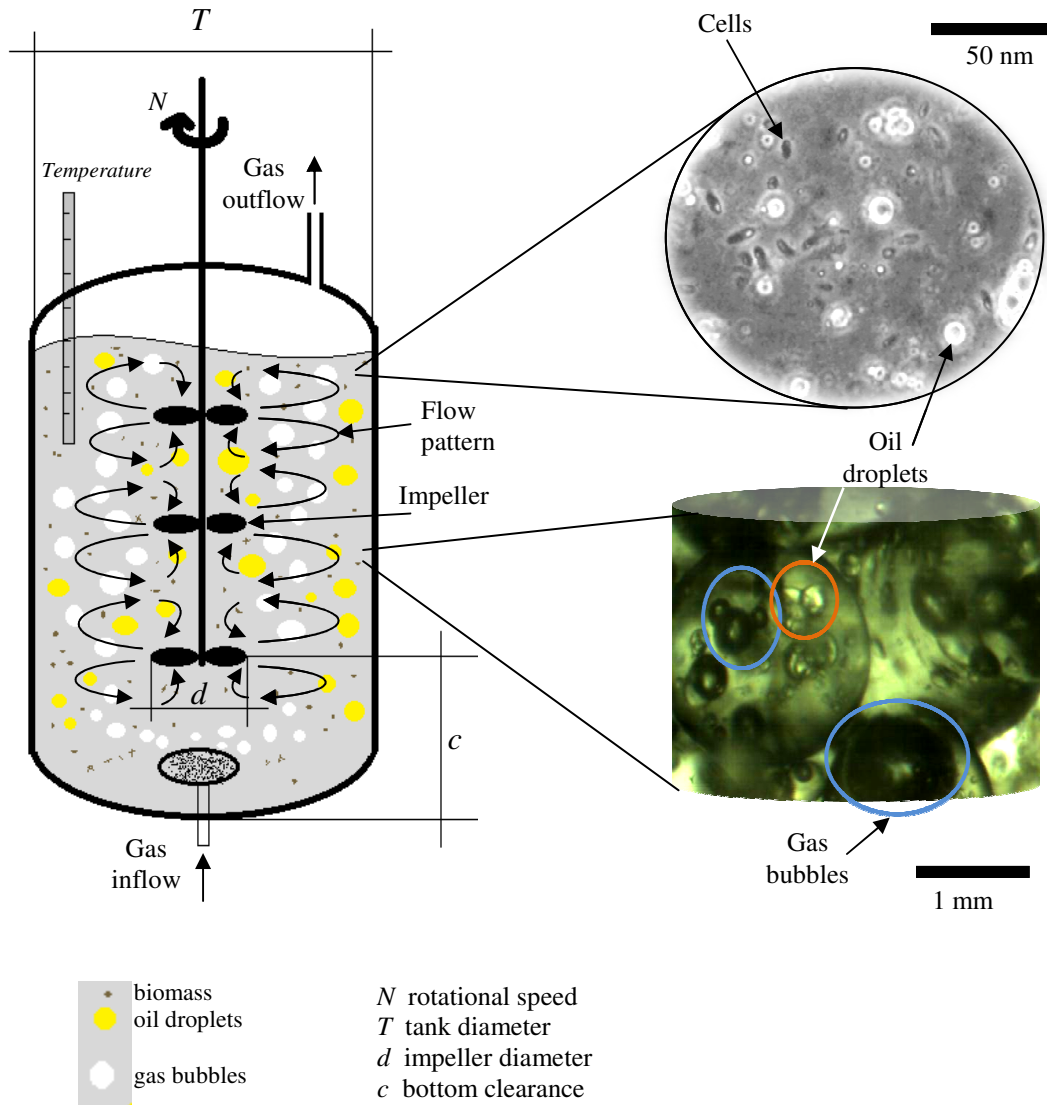


**Figure 1.2.** Performance and main features of liquid fermentations in stirred tank.

The study of the hydrodynamics in fermentations becomes complicated due to the heterogeneity of the phases, because they are thermodynamically unstable and because of the changeability of their rheological properties. To overcome the difficulty of such factors, the hydrodynamics of fermentation broths has been studied in simplified model dispersions (Benchapattarapong *et al.*, 2005; Guevara-López *et al.*, 2008). Several experimental or numerical reports are available for solid-liquid, liquid-liquid or gas-liquid dispersions (see Table 1 at the end of this chapter); however, they have used components, such as glass beads, silicon oils or petroleum products, which are not demanded as fermentation substrates and whose physicochemical properties are different.

## 1.2 Hydrodynamics in stirred tanks

*Stirring is an ancient unifying process. Man has practiced mixing since immemorial times for having fun or in the preparation process of his meals, drinks or formulas. Industry demands improved knowledge in mixing more and more; however, just few decades ago they started to study the stirring hydrodynamics.*

### 1.2.1 Experimental and numerical studies on stirring

The flow regime produced in a stirred tank is determined from a dimensionless quantity, expressed by the Reynolds number (Ec. 1.1). This scalar magnitude relates the inertial forces ( $\rho N d_I^2$ ) with respect to the viscous forces ( $\mu$ ):

$$Re = \frac{\rho N d_I^2}{\mu} \quad (1.1)$$

where  $\rho$  refers to the fluid density,  $N$  refers to the impeller speed and  $d_I$  refers to the impeller diameter. Depending on the impeller type, the flow around the impeller is still laminar typically for  $Re < 10$ , and stagnant away from it; there is a wide transition region between the laminar and the turbulent flow defined for the range  $10 < Re < 10^4$ ; fully turbulent flow is developed for  $Re > 10^4$  (Sajjadi *et al.*, 2002). Gas dispersions produced in stirred tanks are possible only in turbulent regimes (i.e. Reynolds higher than 10,000) (Cooke *et al.*, 2005).

Early research concerned with the hydrodynamics produced in stirred vessels was focused to know the influence of the impeller-tank geometric parameters such as the ratio of the impeller diameter to the tank diameter, the impeller type, the bottom clearance, the number of agitators, the direction of the impeller rotation, the presence of baffles and the tank bottom shape (Murthy *et al.*, 2007; Vakili and Esfahany, 2009). The performance of the Rushton turbine (a radial impeller) and the pitch blade turbine (PBT) (an axial impeller) have concentrated the major discussions, especially for single-phase flows (as shown in Table 1 at the end of this chapter).

The study of macroscopic variables such as power consumption, pumping capacity and pumping efficiency has been estimated to assess the mixing performance or the influence of a gas flow rate (Li *et al.*, 2005, Khopkar *et al.*, 2005). The recording of variables like temperature, solute concentration, pH or color homogenization has served to estimate the mixing time or the circulation time (Zwietering, 1958; Bourne *et al.*, 1981; Amanullah *et al.*, 2004). The impeller rotation speed has been studied experimentally and numerically to know the total dispersion of solid particles (Bao *et al.*, 2005; Murthy *et al.*, 2007). Furthermore, important advances have been also obtained for the mixing of Newtonian or Non-Newtonian fluids (Cooke and Heggs, 2005; Montante *et al.*, 2005).

Computational Fluid Dynamics (CFD) is an advanced tool to study the stirring performance. CFD is based on the resolution of the Navier-Stokes equations. This technique allows modeling the flow patterns and it is useful to predict variables like the pumping capacity, power consumption, circulation time, mixing time, the stretching efficiency, the mean shear rate and, monitoring the clusters migration or the pathlines of massless tracers (Table 1) (Sanjuan-Galindo *et al.*, 2011). Some of these variables are difficult to be estimated experimentally. CFD is a very good option to simulate the scaling-up of the lab mixing performance to pilot and industrial scales; besides, it results a cheap technique to compare several mixing conditions. Numerical models have been also applied in the study of Newtonian or Non-Newtonian fluids but the modeling of multiphase dispersions is computationally expensive (i.e. too many equations and large CPU time).

The flow patterns produced by radial impellers are well known. Campolo *et al.* (2003) described the trajectories of tracer generated by a Rushton turbine at  $Re = 48,000$ , and Rivera *et al.* (2004) reported the formation of two segregated zones symmetrically for  $Re = 18$ . Cooke and Heggs (2005) determined that the Scaba impeller produces higher axial flow than the Rushton impeller and Kovács *et al.* (2001) concluded that the Scaba impeller draws less power in comparison with the Rushton turbine. Attempts to model gas-liquid dispersions were made by Khopkar *et al.* (2006), Lane *et al.* (2002) and Kerdouss *et al.* (2006) while solid dispersions were simulated by Fradette *et al.* (2007). The modeling of liquid-liquid dispersions stills scarce (Laurenzi *et al.*, 2009), hence, more experimental work is required.

### 1.2.2 Nature of turbulence

Turbulence is difficult to be defined exactly, but the nature of turbulence has been described by several authors (Mathieu and Scott, 2000; Roberts and Webster, 2002; Tsinober, 2009). Turbulent flows are strongly diffusive, they exhibit strongly enhanced transport processes of momentum, energy, passive objects (scalars: heat, salt, particles of gradients of passive scalars). Turbulent flows also present rapid diffusivity and high levels of fluctuating vorticity. Visual features of turbulence are shown in Fig. 1.3.

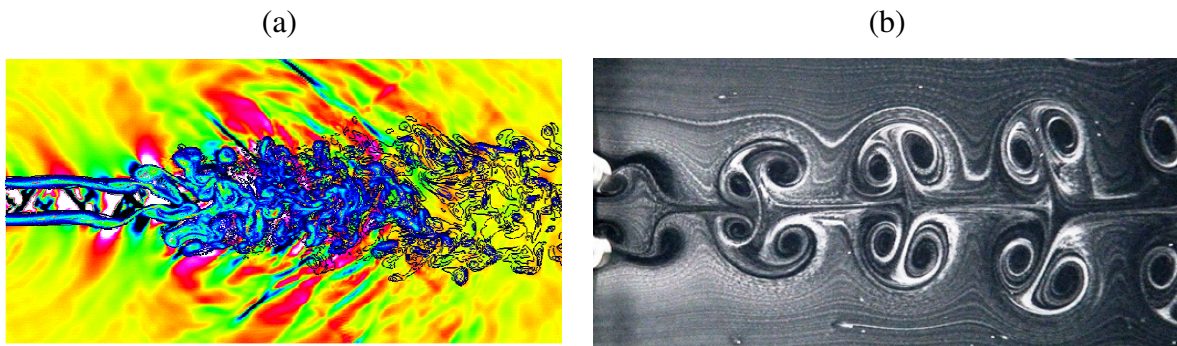


**Figure 1.3** (a) Supersonic sound free-shear flows (Freund *et al.*, 2011) and (b) Symmetrical wake structure behind two uniformly rotating cylinders (Kumar *et al.*, 2011).

Turbulent flows are chaotic and non linear, they are developed completely in three dimensions and are time and space dependent with random fluctuations. Turbulent flows are statistically irreversible and unpredictable; however, it is fruitful to consider statistical properties for the study of turbulent flows, which have reproducible information (i.e. turbulence intensity) (Sharp and Adrian, 2001, Roberts and Webster, 2002). The turbulent intensity characterizes time-fluctuating flows; it is defined as the mean squared of the velocity fluctuations (Mathieu and Scott, 2000).

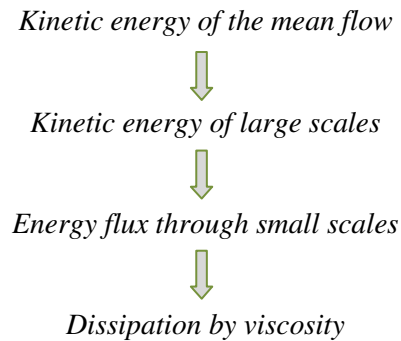
$$v' = \left\{ \overline{v^2} \right\}^{\frac{1}{2}} \quad (1.2)$$

The influence of turbulence has not been fully addressed in events occurring in the dispersion elements inside stirred tanks; for instance, the bubble or drop elongations, deformation or breakage. Velocity fluctuations increase efficiently the momentum and heat transport, which results more effective than molecular diffusion. Antecedents of the fluid-elements breakage occurring in fully developed turbulent flow ( $Re = 66,000$ ) in a straight pipe were presented by

Andersson and Andersson (2006), who compared the number and size of the fragments that result from the rupture of a viscous drop or a gas bubble.

### 1.2.3 Energy dissipation in turbulent flows

Kolmogorov's theory postulates that motion in turbulent flows exists over a broad range of length and time scales. Turbulence produced at high Reynolds numbers produces numerous eddies at different scales. The major part of the turbulent energy is contained in the largest scales, although these eddies are insensitive to the viscosity they are unstable and feed the energy to the smaller eddies via cascade, and so on, until viscosity becomes important at the smallest scales (Mathieu and Scott, 2000). Schematically:



At the smallest scale of a turbulent flow, the rate of dissipation of turbulent kinetic energy ( $\varepsilon$ ) dominate processes like collisions rate, mass transfer, cellular activity, cell damage, mass transfer, mixing and particles fragmentations (Villermaux, 1988; Ducci and Yianneskis, 2005). The energy dissipation rate is a property independent on the fluid viscosity, it depends on the velocity fluctuations as well as the integral scale ( $l$ ). For instance,  $\varepsilon \propto v'^3 l^{-1}$ .

According to the Kolmogorov's theory, the energy of the smallest eddies is directly converted into heat due to viscosity, the scale at which it happens is known as the Kolmogorov micro-scale of turbulence ( $\eta$ ): it combines the dissipation rate ( $\varepsilon$ ) and the kinematic viscosity ( $\nu = \mu/\rho$ ):

$$\lambda = \left( \frac{\nu^3}{\varepsilon} \right)^{\frac{1}{4}} \quad (1.3)$$

Turbulent flows exhibit two regimes: Turbulent inertial and Turbulent viscous. In the former one, dispersed elements are larger than the smallest turbulent eddies and deform under the action of the fluctuations of the hydrodynamic pressure (Fig 1.4a). In the second case, dispersed elements are smaller than the smallest turbulent eddies and, therefore, deform under the action of viscous stress inside and between the eddies (Fig 1.4b).

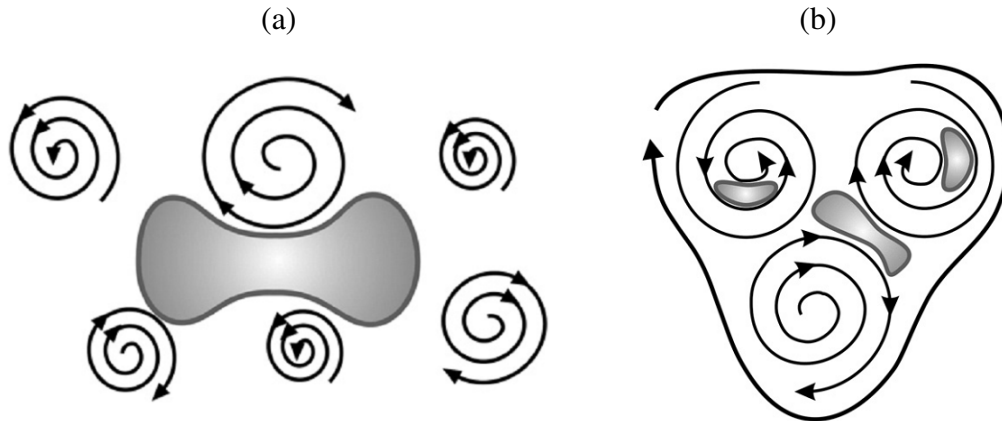


**Figure 1.4.** (a) Turbulent inertial regime. (b) Turbulent viscous regime. (Vankova *et al.*, 2007).

#### 1.2.4 Vorticity

Turbulent flows are characterized for having vorticity, which measures the rotation of a fluid element (Wu *et al.*, 2006). High Reynolds flows are also featured by vorticity, this property deforms fluid elements and influences breakage. Few studies have been conducted under the conditions here tested (i.e. liquid-liquid phases, turbulent regime and rotational agitation condition). Vorticity is computed according to

$$\omega = \nabla \times \vec{v} \quad (1.4)$$

### 1.3 Flow visualization in stirred tanks

*Visualization simplifies our understanding of phenomena described by fluid mechanics.*

#### 1.3.1 Flow visualization techniques

Some useful techniques are used to visualize and investigate the flow structure in stirred tanks, namely: Laser Doppler Anemometry (LDA), Nuclear Magnetic Resonance (NMR), Computer-Automated Radioactive Particle Tracking (CARPT), among others. In such techniques, fine optical registers are obtained from brilliant or radioactive small trackers that follow the flow faithfully (Khopkar *et al.*, 2005; Li *et al.*, 2005; Pakzad *et al.*, 2008; Kamankhan, 2009). Particle Image Velocimetry (PIV) is another visualization technique used frequently for the study of the flow fields in stirred tanks. PIV provides multi-point instantaneous measurements of the velocity field that leads the estimation of the turbulence intensity, the vorticity field or the energy dissipation rate, etc. (Sheng *et al.*, 2000). In most of the cases, the techniques just mentioned have been limited to visualize single phase flows. In a recent study presented by Laurenzi *et al.* (2009), PIV was used to compare the flow properties of a single phase flow and a liquid-liquid dispersion in a stirred tank.

Suitable *in situ* descriptions of dispersions containing up to four phases (including the water phase) have been achieved applying images analysis (Galindo *et al.*, 2005). The technique has allowed the study of low concentrated dispersions in small regions close to the tank wall. Image analysis has been used to determine and compare the drop diameters and the instantaneous displacement of drops in a local region (Taboada *et al.*, 2006; Guevara *et al.*; 2008).

### **1.3.2 Visualization of viscous structures and drops in stirred tank**

Until now, the study of oil dispersions produced in agitated vessels has been limited for a stage where the process reaches a quasi-steady state; for instance, once the drops sizes compared in a Probability Density Function (PDF) exhibit unimportant changes (Zhou and Kresta, 1998a; Lovick *et al.*, 2005). However; the mechanism occurred in the early time of the process has received less importance; in this stage, oil viscous structures and filament-like shapes are formed. The present work discusses more about it.

Viscous filaments can be described as time-dependent fluid threads moving into a surrounding fluid; the phenomenon is known as tangential separation and it is present in many day to day activities, for instance, honey threads falling in air into a piece of bread. One of the first theories is the Plateau-Rayleigh instability, which consists of undulations produced by capillary effects. Other



studies have described confined filaments (Hagedorn *et al.*, 2004), the effects of gravity, inertial or viscous forces as well as phenomena like folding, bending, coiling and rupture produced by viscous forces were reported by Ribe (2004) and Duclaux *et al.* (2006). Eggers and Villermaux (2008) summarized other perturbations like the transition from dripping to jetting, a coflowing liquid stream, and the effect of the velocity differences between the filament and its surroundings. Yarin (1997) reported a computational study, in which the dynamics of stretched vortex filaments exposed to shear flow was described. External flow, gravity or axial forces elongate threads and their cross-area becomes reduced heterogeneously causing longitudinal rearrangements or breakage (Oliveira and McKinley, 2005). In a recent work, Shingho and Umemura (2010) studied in detail the influence of the vortices in the drop generation in an atomization process. Nonetheless the wide background, filaments produced in a stirred tank remain unexplored.

## 1.4 Summary of the literature survey

### 1.4.1. *Comparison of previous works*

Table 1 summarizes the works reported in the literature dealing with the hydrodynamics in stirred vessels by using axial or radial impellers without considering chemical reaction kinetics. It is noticeable the amount of works published for single phase flows. The performance of pitched blade turbines (PBT) and Ruston turbines has been classically studied, particularly to understand the hydrodynamics of stirred vessels in terms of macroscopic variables such as the power consumption and mixing times. The application of CFD or visualization techniques like PIV has allowed improve the knowledge of flow structures, the turbulent flow properties and the vorticity fields. Indeed, the influence of these flow properties has not been entirely investigated as determinant factors to improve the product quality and the scaling-up of fermentation process.

Although there is a wide research concerned in the hydrodynamics of gassed flows in stirred tanks, few contributions have been produced to deep more in the mass transfer process. On the other side, the quantification of oil drop size has been the main objective of numerous publications but there is a lack of knowledge in the early stage of a dispersion process; before drops saturate the system. The hydrodynamics of the castor oil as a dispersion component has not been reported until now.

Summarizing, more advances are needed to know more about the hydrodynamics of fermentative liquid cultures.

In the present work the flow patterns, the turbulent flow properties and the vorticity fields generated by a Scaba impeller (a radial discharge impeller) have been obtained looking to explain their influence on the dispersion mechanism of three elements: an immiscible viscous liquid, a gas flow and biomass as a solid phase. Castor oil, used as second liquid phase, is an organic substrate required in liquid fermentations. Evidences of viscous structures like filaments are analyzed as a part of the dispersion process. Such detailed visualization has not been reported up to date, at least for the particular case of stirred tanks. The techniques used were PIV and high-speed video recordings.

## **1.5 Objective**

To investigate the influence of the flow fields in the dispersion process of non-miscible phases under turbulent conditions in stirred tank.

**Table 1.** Comparison of the published works prepared to investigate hydrodynamics in stirred tanks in single or multiple phases agitated with radial or axial impellers.

<b>Impeller type</b>	<b>Variables discussed</b>	<b>Phase (s)</b>	<b>Rheology of the continuous phase</b>	<b>Reynolds number (-)</b>	<b>Methods utilized</b>	<b>Reference</b>
Axial flow impeller	Velocity field, turbulent flow properties	Liquid phase	Newtonian	Undefined	CFD	Sahu <i>et al.</i> , 1998
No specified	Drop size distribution, phase inversion	Water-oil dispersions (aromatic oil)	Newtonian	320	Video camera connected to an optical microscope	Sajjadi <i>et al.</i> , 2002
Hydrofoil	Flow field and turbulence energy dissipation rate	Liquid phase	Newtonian	$40 \times 10^3$	PIV	Baldi and Yianneskis, 2003
Retreat curve impeller	Flow field	Liquid phase	Newtonian	$4.55 \times 10^3 < Re < 2.5 \times 10^5$	LDA and CFD	Li <i>et al.</i> , 2005
Marine propeller and Helical Ribbon	Effect of the impeller type and the solids concentration in the solid particles dispersion	Solid dispersion (for the solid phase: glass beads)	Newtonian and a shear-thinning fluid	$Re < 3$	CFD and photographic visualization	Fradette <i>et al.</i> , 2007
Impeller blades	Effects of the geometrical features on the flow field.	Liquid phase	Newtonian	$1.3 \times 10^4 < Re < 11.4 \times 10^4$	CFD	Vakili and Esfahany, 2009
Disk and Flat blade turbines and PBT.	The minimum agitation speed to have a complete dispersion of the immiscible liquid phase	Heptane or mineral oil dispersed in water	Newtonian	$1.7 \times 10^4 < Re < 13 \times 10^4$	Dispersion sampling	Armenante and Huang, 1992
PBT	Multidrops formation and phase inversion	Oil dispersions (aromatic and silicon oils)	Newtonian	$37 \times 10^3 < Re < 47 \times 10^3$	High speed video recordings	Pacek and Nienow, 1995
PBT	Turbulence dissipation rate	Liquid phase	Newtonian	$10 \times 10^3$	PIV	Sheng <i>et al.</i> , 2000
PBT	Velocity fields, up and down pumping effects	Gas-liquid dispersion	Newtonian	$45 \times 10^3$	PIV	Aubin <i>et al.</i> , 2004
PBT	Tracer concentration, Mixing variables	Liquid phase	Newtonian and pseudoplastic fluids	$2.5 \times 10^3 < Re < 10 \times 10^3$	CFD	Montante <i>et al.</i> , 2005
PBT	Velocity fields, gas hold-up distribution	Gas-liquid dispersion	Newtonian	$20 \times 10^3 < Re < 60 \times 10^3$	CFD	Khopkar <i>et al.</i> , 2006

PBT	Velocity fields, turbulent kinetic energy, dissipation of kinetic energy.	Liquid phase	Newtonian	$47.5 \times 10^3$	Angle resolved PIV measurements	Khan <i>et al.</i> , 2006
PBT	Velocity field, minimum impeller speed for the onset of surface aeration (Up and down pumping), effects of the impeller clearance, the baffle geometry and liquid properties	Liquid phase and surface aeration	Newtonian	$480 < Re < 130 \times 10^3$	LDV	Bhattacharya <i>et al.</i> , 2007
PBT	Velocity field, mixing time, gas dispersion and the time evolution of the tracer's concentration.	Gas dispersions	Newtonian	$4.6 \times 10^4$	Conductivity measurements and CFD	Jahoda <i>et al.</i> , 2009
PBT, Paddle type, Rushton, Marine propeller	The effects of the impeller type and position in the mean size of air bubbles.	Air in water	Newtonian	$7 \times 10^3 < Re < 26 \times 10^3$	High speed camera and CFD	Martín <i>et al.</i> , 2008
PBT	Influence of the solid phase concentration in the turbulence levels, the turbulent kinetic energy and dissipation rate.	Solid-liquid dispersions (for the solid phase: Soda-lime glass spheres 1000 $\mu$ m sized)	Newtonian	$30 \times 10^3$	FPIV	Unadkat <i>et al.</i> , 2009
Rushton	Sauter mean diameter and drop size distribution, effects of the viscosity and interfacial tension	Oil in methanol solutions (Silicone oil)	Newtonian	$14 \times 10^3 < Re < 83 \times 10^3$	Photographic system	Wang and Calabrese, 1986
Rushton	Drop size distribution and coalescence frequencies, effects of the impeller rotational speed	Oil in water (aromatic oils)	Newtonian	$30 \times 10^3 < Re < 60 \times 10^3$	Flash photomicrographic system	Coulaloglou and Tavlarides, 1976
Rushton	Velocity fluid measurements.	Liquid phase	Newtonian	$39 \times 10^3 < Re < 46 \times 10^3$	LDA	Shoot and Calabrese, 1995
Rushton	Sauter mean diameter and drop size distribution	Oil in water (aromatic oil, 0.5 % v/v < $\phi$ < 10 % v/v)	Newtonian	$16 \times 10^3 < Re < 45 \times 10^3$	Video recordings	Pacek <i>et al.</i> , 1998
Rushton, PBT, HE3 and Fluidflow turbine	Drop size distribution and minimum drop size as function of the type of impeller, the impeller rotational speed and the energy dissipation	Oil in water (silicone oil, $\phi = 0.03$ % v/v)	Newtonian	$42 \times 10^3 < Re < 144 \times 10^3$	LDA and PDPA	Zhou and Kresta, 1998a

Rushton, PBT, HE3 and Fluidflow turbine	Drop size distribution as function of time, the type of impeller and the impeller rotational speed	Oil in water (silicone oil)	Newtonian	$35 \times 10^3 < Re < 80 \times 10^3$	Aerometric PDPA	Zhou and Kresta, 1998b
PBT, Rushton and Scaba	Comparison of the gas holdup up- and the down-pumping mode. Estimation of the mass transfer.	Air dispersions	Newtonian	$45 \times 10^3 < Re < 75 \times 10^3$	Liquid level and power consumption measurements	Sardeing <i>et al.</i> , 2004
PBT and Rushton	Effects of the impeller type and other geometrical parameters in the velocity profiles for single phase of in the presence of solids or gas, as well as the critical impeller speed for the solid suspension	Gas-liquid, solid-liquid and gas-solid-liquid dispersions (for the solid phase: glass and quartz particles)	Newtonian	$2.5 \times 10^5 < Re < 5.2 \times 10^5$	CFD	Murthy <i>et al.</i> , 2007
Rushton	Effects of the temperature (23°C to 60°C) and the impeller speed in the drop size.	Styrene dispersed in water.	Newtonian	$20 \times 10^3 < Re < 58 \times 10^3$	Laser diffraction.	Chatzi <i>et al.</i> , 1991
Rushton	Floculation of colloidal particles, effects of the pH, agitation speed, particle size and electrostatic forces	Solids in water (Polymer particles)	Newtonian	$8 \times 10^3 < Re < 17 \times 10^3$	Light-scattering	Chin <i>et al.</i> , 1998
Rushton	Root mean square (rms) velocities, vorticity and energy dissipation in the impeller tip	Water	Newtonian	4,580	PIV	Sharp and Adrian, 2001
Rushton	Flow profile, holdup, bubble diameter,	Gas in water	Newtonian	$33 \times 10^4$	CFD	Lane <i>et al.</i> , 2002
Rushton	Flow structures, <i>Poincaré</i> maps	Glycerine-water mixture	Newtonian	$20 < Re < 200$	CFD and Fluorescent dye visualization	Zalc <i>et al.</i> , 2002
Rushton	Flow field, vortex structures, energy rate dissipation.	Liquid phase	Newtonian	$4 \times 10^3$	CFD and PIV	Yoon <i>et al.</i> , 2003
Rushton	Velocity field, velocity fluctuant gradients, Reynold stress and turbulent energy dissipation,	Water	Newtonian	$15 \times 10^3 < Re < 40 \times 10^3$	PIV	Baldi and Yianneskis. 2004

Rushton	Flow macroinstabilities (low frequency mean flow variation)	Liquid phase	Newtonian	$20 \times 10^3 < Re < 30 \times 10^3$	CFD	Hartmann <i>et al.</i> , 2004
Rushton	Breakup, coalescence and phase inversion	Oil in water (silicone oil)	Newtonian	$12 < Re < 6 \times 10^4$	No specified	Nienow, 2004
Rushton	Energy dissipation	Water	Newtonian	$20 \times 10^3 < Re < 40 \times 10^3$	Two point LDA	Ducci and Yianneskis 2005
Rushton	Drop size distribution, effects of the rotational impeller speed and the oil fraction.	Oil in water (aromatic oil, 10 % v/v < $\varphi$ < 60 % v/v )	Newtonian	$24 \times 10^3 < Re < 39 \times 10^3$	High speed video-endoscopy and Optical reflectance	Lovick <i>et al.</i> , 2005
Rushton	Turbulent flow features.	Liquid phase.	Newtonian	$30 \times 10^3$	CFD	Alcamo <i>et al.</i> , 2005
Rushton and PBT	Velocity patterns, power and pumping numbers and the mixing times,	Liquid phase.	Newtonian	$46.7 \times 10^3$	CFD	Moštek <i>et al.</i> , 2005
Rushton	Mixing variables.	Liquid phase	Newtonian	$40 \times 10^3$	CFD	Yeoh et al, 2005
Rushton	Flow field, gas holdup, bubble size distribution.	Gas dispersion	Newtonian	$71 \times 10^3$	CFD	Kerdouss <i>et al.</i> , 2006
Rushton	Silicon oil drop size distribution	Silicon oil with different viscosities dispersed in water	Newtonian	$2.1 \times 10^4 < Re < 3.6 \times 10^4$	Video recordings	Podgórska., 2006.
Rushton	Gas-liquid mass transfer	Gas liquid dispersions	Newtonian	$2.2 \times 10^5 < Re < 3.3 \times 10^5$	CFD and DO measurements	Laakkonen <i>et al.</i> , 2007
Rushton	Flow field, gas hold-up, prediction of the gas cavities and the effects of the impeller speed and the gas flow rate.	Gas dispersions	Newtonian	$1.4 \times 10^5$	CFD	Scargiali <i>et al.</i> , 2007
Rushton	Velocity field, trailing vortices, turbulent kinetic energy dissipation and shear strain rate	Water	Newtonian	$40 \times 10^3$	PIV	Xinhong <i>et al.</i> , 2008
Rushton	Bubble size distribution, velocity field.	Gas-liquid dispersions	Newtonian	$2.0 \times 10^4 < Re < 4.6 \times 10^4$	CFD, image processing and two-phase PIV	Montante <i>et al.</i> , 2008
Rushton and CD-6 impeller	Velocity field, power consumption, the local bubble size, the mass transfer coefficient $k_{LA}$ , the bubble size distribution, the DO evolution.	Gas-liquid dispersions	Newtonian	$8.6 \times 10^4 < Re < 28.6 \times 10^4$	CFD	Gimbin <i>et al.</i> , 2009
Rushton	Mixing time influenced by object inserted in the vessel	Liquid phase	Newtonian	10	Photographs	Takahashi and Motoda, 2009

Rushton	Effects of the dispersion components in the flow pattern. Estimation of the impeller speed at which the drops appear below the impeller and where the oil is completely dispersed	Oil in water (aromatic oils, $\phi = 1 \% v/v$ )	Newtonian	$1.2 \times 10^4 < Re < 3.1 \times 10^4$	Images capture, PIV and CFD	Laurenzi <i>et al.</i> , 2009
Rushton	Bubbles size distribution, bubble and flow velocities distribution, flow velocity field	Air in water	Newtonian	49,000	CFD, PIV combined with Back lighting, digital masking and fluorescent tracer particles	Kamankhan, 2009
Rushton	Turbulent flow properties, toluene mother drops breakage	Oil in water (Oil: toluene)	Newtonian	$57 \times 10^3$	CFD and a Photographic method	Maaß <i>et al.</i> , 2009
Rushton	Size and velocity of the gas bubbles, flow velocity field.	Air in water	Newtonian	$49 \times 10^3$	CFD and PIV	Zamankhan, 2010
Rushton and Scaba	The influence of the impeller type on the flow structure and scalar transport	Liquid phase	Newtonian	$10 \times 10^4$	CFD	Revstedt <i>et al.</i> , 2000
Rushton	Axial profiles	Liquid phase	Newtonian	$45 \times 10^3$	PIV measurements and CFD simulations	Khopkar <i>et al.</i> , 2004
Scaba	Flow pattern, turbulent kinetic energy profiles and the gas holdup	Liquid phase and gas-liquid dispersion	Newtonian	$45 \times 10^3$	PIV measurements and CFD simulations	Khopkar <i>et al.</i> , 2004
Hydrofoil and Scaba	Effects of the impeller configuration, impeller speed and the solid concentration in the gas holdup and the power consumption	Gas, and a solids dispersed in water For the solid phase; Polypropylene beads	Newtonian	$7.2 \times 10^4 < Re < 42.4 \times 10^4$	Visual observations and liquid level measurements	Bao <i>et al.</i> , 2005
Scaba and Rushton	Gas dispersion (flooding-loading)	Gas-liquid and air-solid-liquid dispersions	Power law fluid (0.4 % CMC solution)	$309 < Re < 3456$	High speed video recordings	Cooke and Heggs, 2005
Scaba	Velocity fields and mixing caverns	Liquid phase	Pseudoplastic	$3 < Re < 81$	UDV and CFD	Pakzad <i>et al.</i> , 2008

**Abbreviations:** CFD, Computational Fluid Dynamics; DO, Dissolved Oxygen; LDA, Laser Doppler Anemometry; LDV, Laser Doppler Velocimetry; PBT, Pitched Blade Turbine; PDPA, Phase Doppler Particle Analyzer; PIV, Particle Image Velocimetry; FPIV, Fluorescent Particle Image Velocimetry; UDV, Ultrasonic Doppler Velocimetry.

CHAPTER 2

*Materials and  
methods*



This chapter provides the information concerned with the substances used in the dispersion, describes the setup where the experiments were made, details the image capture process and the equipment employed, and references the equations valid in the data processing.

## 2.1 Studied dispersions

### 2.1.1 Liquid-liquid dispersion

Distilled water ( $\rho_{H_2O} = 1,000 \text{ kg m}^{-3}$ ,  $\mu_{H_2O} = 1.0 \text{ mPa s}$ , surface tension  $\sigma_{H_2O} = 72 \text{ mN m}^{-1}$ ) was used as continuous phase and Castor oil ( $\phi = 1\% \text{ v/v}$ ,  $\rho_{Oil} = 960 \text{ kg m}^{-3}$ ,  $\mu_{Oil} = 560 \text{ mPa}\cdot\text{s}$ ,  $\sigma_{Oil} = 39 \text{ mN m}^{-1}$ ) as the dispersed viscous phase. The viscosity ratio of the oil to water was 550. The interfacial tension between the oil and water is  $\sigma_{o-w} = 21 \text{ mN m}^{-1}$  at  $20^\circ\text{C}$  (Fisher *et al.*, 1985). In the beginning of the experiments the oil was suspended on the surface of the water.

### 2.1.2 Gas-liquid dispersion

The gas flow was supplied from a 4 mm diameter pipe placed in the bottom of the tank, aligned with the center of the impeller disk. The superficial gas velocity  $v_s$  is defined as follows (Cooke *et al.*, 2005):

$$v_s = \frac{4Q_G}{\pi T^2} \quad (2.1)$$

For a volumetric gas flow rate  $Q_G = 0.5 \text{ L/min}$ ,  $v_s$  was  $0.002 \text{ m/s}$ . The interfacial tension between the air and water is  $\sigma_{a-w} = 72 \text{ mN}\cdot\text{m}^{-1}$  at  $20^\circ\text{C}$ . Warmoeskerken and Smith (1985) introduced two concepts to define the condition of dispersed gas in a stirred tank. The first one, flooding, refers to the regime in which there is an axial flush of gas through the impeller plane up to the liquid surface. Loading is the second one, it happens when the agitator pumps the gas into the impeller wall. The impeller performance to avoid flooding by radial impellers was evaluated by Cooke *et al.* (2005), by describing two dimensionless numbers: the " $g$ " force and the Froude number  $Fr$ . Both parameters will be defined in section 2.5.

### 2.1.3 Gas hold-up

The gas hold-up ( $\epsilon$ ) is gas fraction dispersed in the liquid (Zlokarnik, 2001), which is computed by considering the height of the gassed liquid ( $H_g$ ) and the height of the ungassed liquid ( $H$ ):

$$\epsilon = \frac{H_g - H}{H} \quad (2.2)$$

For the conditions tested in this study, the hold-up was  $\epsilon = 0.17$ .

### 2.1.4 Biomass-liquid dispersion

Fungus pellets are amorphous clusters of single cells. Fungus cells and its metabolites are industrially produced to obtain organic acids, antibiotics and recombinant enzymes. Edible fungus pellets of *Pleurotus ostreatus* CP50 –a widely distributed cultivar for commercial mushroom production- were used as a dispersed biomass; the strain was isolated by the “Colegio de Posgraduados” Puebla and the fungus pellets were produced in the pilot plant of “Instituto de Biotecnología”-UNAM following to the procedure detailed in Tinoco *et al.* (2011). Fresh biomass, harvested from the fermentation broth and kindly donated by R. Tinoco, was washed with cold water several times to remove the remains of the culture, thereafter the fungus pellets were separated by gravity. 20 ml (0.02 % v/v) of the washed pellets were put in the tank and filled with water. The system was stirred during 5 hours at  $Re = 24,000$ ; along this time several samples were taken to determine the influence of the flow pattern in the pellet size. The samples were diluted and photographed using a Finepix s1 photo camera (pro Fujifilm) with an AF micro Nikkor 60 mm 1:2.8D lens (Nikon, Japan). Thereafter, the images were analyzed to compare the pellets size accordingly to the following procedure: the pellet size is very heterogeneous with amorphous shapes, therefore that pellets were treated as an ellipse shape (Fig. 2.1 a and b). Two orthogonal radii were measured in each pellet. Then, the ellipse perimeter ( $p$ ) was approximated by

$$p = 2a\pi \left( 1 - \sum_{i=1}^{\infty} \frac{(2i)!^2}{(2^i \cdot i!)^4} \cdot \frac{e^{2i}}{2i-1} \right) \quad (2.3)$$

where  $a$  and  $b$  refer to the major and the minor radius of the ellipse (Fig. 2.1c), respectively;  $e$  is an eccentricity term defined as  $e = a^{-1} \cdot \sqrt{(a^2 - b^2)}$ , Eq. 2.3 was computed until  $i = 5$ .

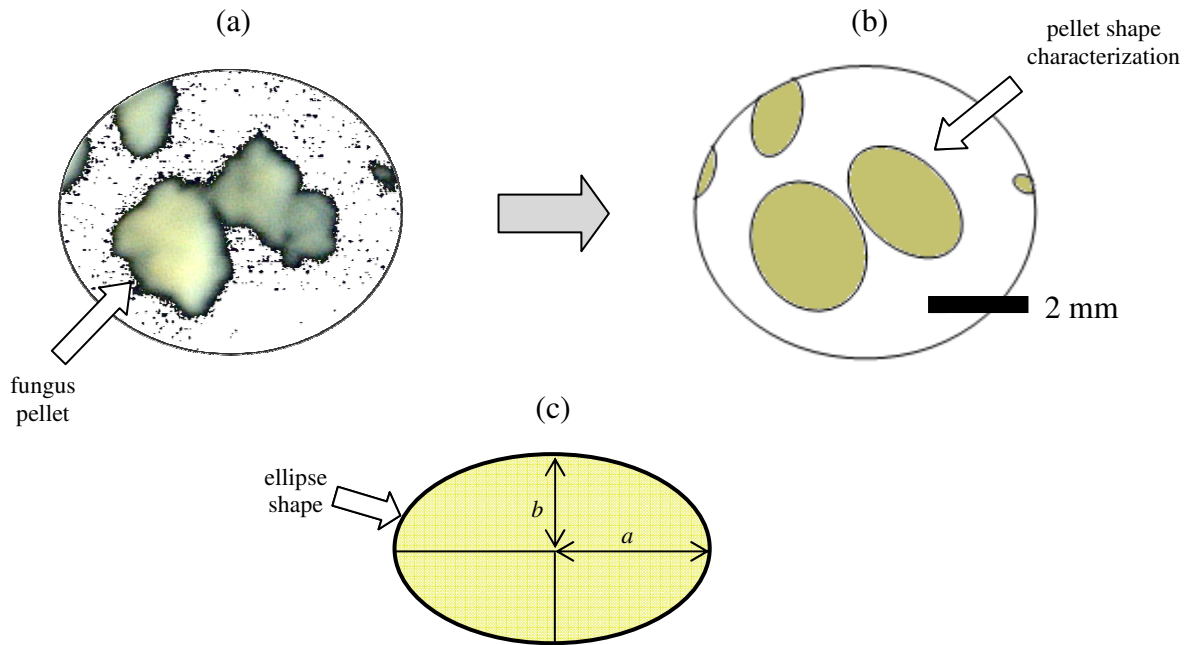


**Figure 2.1.** Procedure for the analysis of the fungus pellet shape (the bar length equals 2 mm). (a) A real image showing the fungus pellets. (b) Characterization of the pellet shapes as regular ellipses. (c) Major ( $a$ ) and minor ( $b$ ) radius of the ellipse considered for the perimeter estimation.

The perimeter of about 300 pellets was computed for each condition in order to have enough data to compare the evolution of the pellet size. The objective of this work discards monitoring any biological activity and exclusively the hydrodynamic phenomenon is considered; the results are discussed in section 4.1.5.

## 2.2 Experiment setup

### 2.2.1 Mixing equipment

Experiments were conducted in a cylindrical tank made in glass having an inner diameter of  $T = 0.135$  m and flat bottom. The liquid volume was  $V_L = 1$  L and four standard width baffles ( $T/10$ ) were equally spaced and fixed inside the tank. A Scaba impeller of diameter  $d_I = 0.5T$  composed by a thin disc and six half-tube blades was used. The shape and dimensions for the tank-impeller system are shown in Fig. 2.2a. The rotational impeller speed was fixed to  $N = 5 \text{ s}^{-1}$  (300 rpm). The impeller location from the tank bottom is  $c = 0.5H$ , where  $H$  is the liquid level. To avoid the optical distortion produced by the cylindrical tank walls, a square jacket filled with water was employed. All experiments were conducted at room temperature (22 °C) and no surfactants were added.

### 2.2.2 Power consumption

The specific power consumption was estimated from the torque produced when the impeller rotates and the tank rests in a frictionless surface (Ascanio *et al.*, 2004). For the Reynolds number considered in this study the specific power was  $P/V_L = 0.46 \text{ W}\cdot\text{m}^{-3}$ . It is well documented that the power consumption in mixing systems agitated with the Scaba impeller is not altered by the presence of gas flows (Cooke and Heggs, 2005).

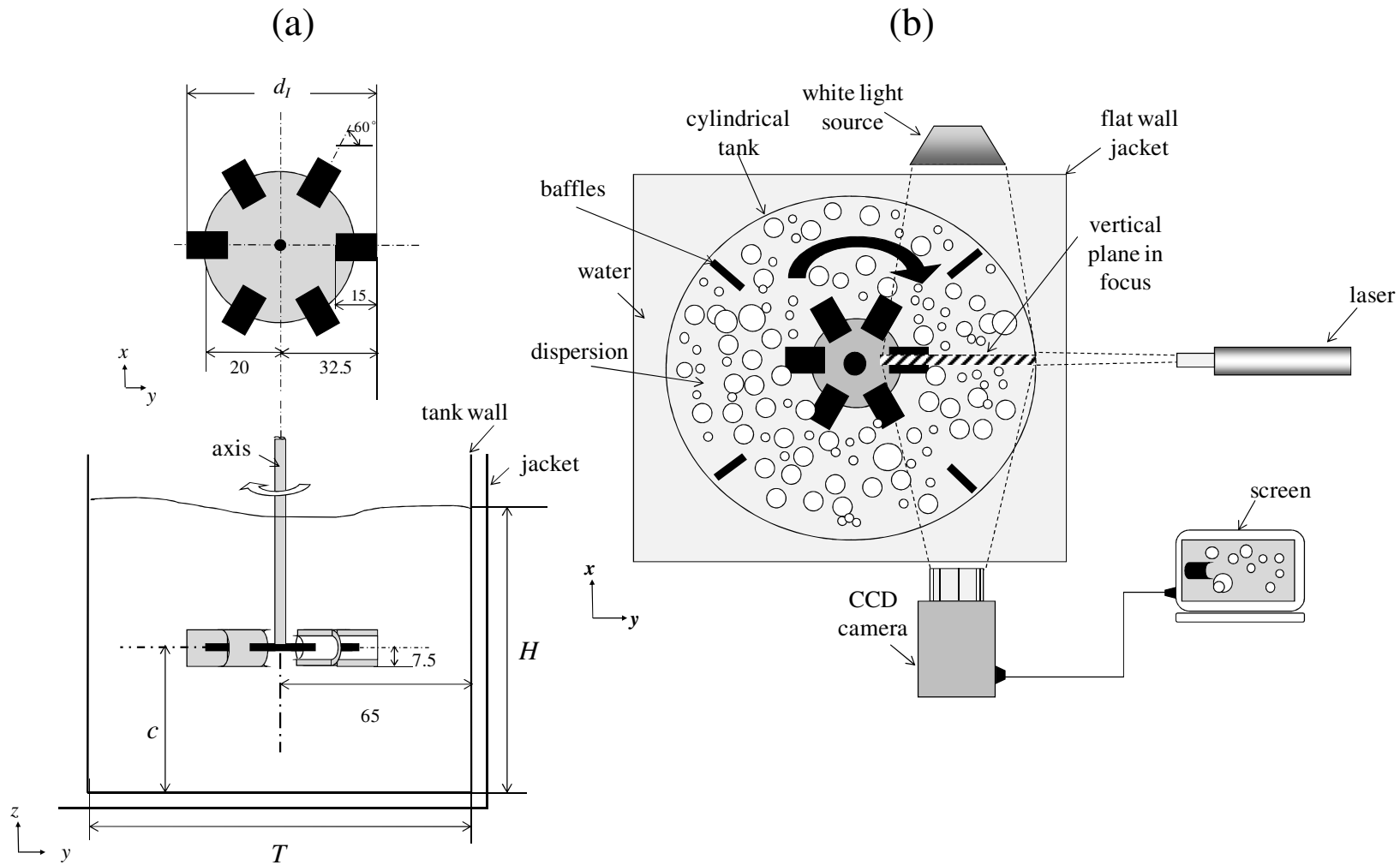


**Figure 2.2.** (a) Geometry and main dimensions of the impeller (mm), scheme not to scale. (b) Top view of the setup used for the capture of high-speed video and PIV. Nomenclature:  $T$ , tank diameter;  $d_I$ , impeller diameter;  $c$ , bottom clearance and  $H$ , liquid height.

## 2.3 Video recordings and velocity measurements

### 2.3.1 High speed video recordings

Image sequences of the dispersion were obtained using a high-speed CCD camera (Redlake Motion Pro HS-4) with an AF micro Nikkor 60 mm 1:2.8D lens (Nikon, Japan). The video recordings were made for a half vertical plane assuming vertical symmetry. The setup was illuminated with a back source of light, using a 300 Watts incandescent filament and a diffuser. All videos were taken at 400 frames/s and images size of  $512 \times 512$  pixels, which corresponds to an area of  $60 \text{ cm}^2$ . A sketch showing the region recorded with the high-speed camera is shown in Fig. 2.2b.

### 2.3.2 PIV measurements

The velocity fields for a single vertical plane were obtained with a Particle Image Velocimetry system (PIV), which consists of a digital camera Megaplus, Model ES 1.0 (*Roper Scientific MASD Inc.*) and a *AF Micro Nikkor* 60 mm 1:2.8 D lens (Nikon, Japan). The laser light is a *Solo III PIV (New-Wave)* with a frequency of 15 Hz and a wave length of 532 nm (green light). The experimental arrangement is also shown in Fig. 2.2b. Laser pulses were synchronized with the impeller rotation and the camera recordings (phase locking). The *Flow manager* software from Dantec Dynamics was used to control the system and to process the images. Silver coated glass hollow spheres of  $10 \mu\text{m}$  were used as light reflective tracers. The velocity fields were obtained with a standard cross-correlated technique considering  $32 \times 32$  interrogation windows, with an overlap of 50%. A total of 1,000 pairs of images were processed to obtain the average velocity field ( $\bar{v}$ ). The time step between photos was 300 ms. Moving average and filter validations were applied to the resulting fields.

## 2.4 Reduced scale visualizations

### 2.4.1 Individual drops visualized with high speed video

The instantaneous velocity for the individual droplets was measured in a region located near the tank wall. The area of study in this region is about  $6 \text{ mm}^2$ . The setup was rearranged as shown in Fig. 2.3a. Images were captured using an  $11\times$  magnification. The droplets appearing in the

sequence of 2,000 images were manually measured using the Image-Pro® Plus software (version 5.2, Media Cybernetics, USA) which allows tracing manually oil drops as circular objects. The diameter of about 300 droplets was measured twice in two consecutive frames, those measurements with an error larger than 10% were discarded. To gain accuracy, only those well focused objects were selected.

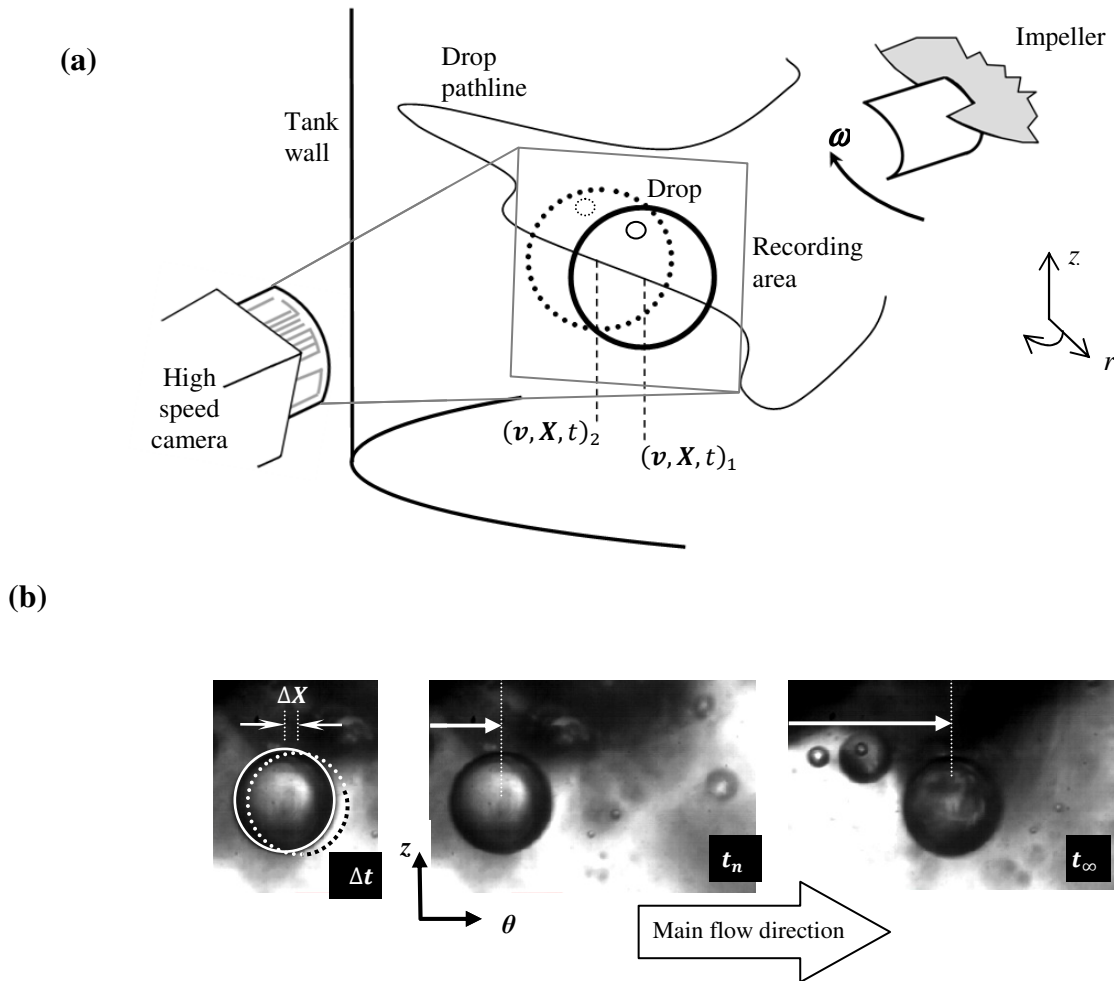


**Figure 2.3.** (a) Experimental setup to investigate the instantaneous displacement for the individual oil droplets. (b) Circles traced with a continuous line represent the initial droplet position ( $t_1$ ) and pointed circles represent the droplet position at  $t_2$ . Symbols:  $v$ ,  $X$ , and  $t$  represent the velocity vector, the position vector and time, respectively.  $r$ ,  $\omega$  and  $z$  represent the radial, the angular and the axial coordinates, respectively.  $\theta$  represents the tangential direction.

Only well focused drops were measured and those ones appearing bad defined were not considered. The droplet position in two times is differentiated with a continuous line for the initial time ( $t_1$ ) and with a dashed line for the final time ( $t_2$ ). The position vector for the droplet center was

defined as  $\mathbf{X} = f(x, z)$ .  $\Delta \mathbf{X}$  represents the droplet displacement in the time interval ( $\Delta t = 0.19$  ms) and the velocity vector was estimated as  $\mathbf{v} = \frac{\Delta \mathbf{X}}{\Delta t}$ .

### 2.4.2 PIV measurements for the oil phase

PIV measurements were obtained for the same local region in which the light scattered by the oil phase was monitored instead of using brilliant tracers. A similar procedure to follow oil reflectance was applied by Laurenzi *et al.* (2009), who used tetradecane as the dispersed phase. As Figure 2.4 shows, the PIV camera and the laser shoot were oriented to study the average velocity in the planes identified as  $\theta z$  and  $r z$ , located near the tank wall and aligned with the impeller disk, respectively. The plane  $r z$  is oriented in the same direction of the main direction of the impeller discharge flow. The area of study in each plane was about  $5 \text{ mm}^2$ .

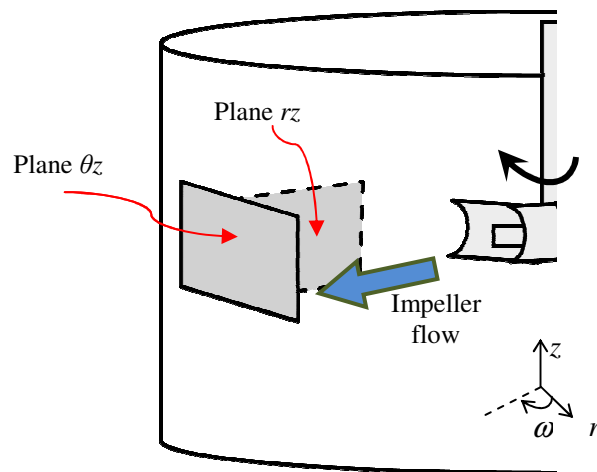


**Figure 2.4.** Orientation of the normal planes ( $r z$  and  $\theta z$ ) to investigate the local hydrodynamics.

### 2.4.3 Streamlines

Streamlines are defined as vector lines tangent to the velocity of the flow. They can be computed as follows:

$$\frac{dx_i}{v_i} = \frac{dx_j}{v_j} \quad (2.4) \quad \text{for } i \text{ or } j = r, \omega, z \quad \text{if } i \neq j$$



## 2.5 Variables of study

### 2.5.1 Pumping characterization

The pumping flow number ( $N_Q$ ) was calculated from the velocity field as a criterion to assess the stirring performance (Rivera *et al.*, 2009). Based on the flow direction  $N_Q$  can be defined by means of the following expression:

$$N_{Q_k} = \frac{Q_k}{Nd_I^3}, \quad \text{for } k = r, z \quad (2.5)$$

for this equation,  $d_I$  and  $N$  were defined above,  $Q_k = v \cdot dA$  is the volumetric flow and  $dA$  is the differential of the cross-sectional area normal to the flow. This area was computed in two different ways: (1) for the radial flow ( $Q_r$ ),  $A = 2\pi rz$  and, (2) for the axial flow ( $Q_z$ ),  $A = \pi r^2$ ; in these equations,  $r$  is the impeller radius and  $z$  is an axial dimension related to the impeller blade width. Considering the axial and radial velocity components, the global pumping number was estimated using:

$$N_Q = \sqrt{N_{Qr}^2 + N_{Qz}^2} \quad (2.6)$$

### 2.5.2 Turbulence intensity

The turbulence intensity was computed by

$$v' = \left\{ \overline{v^2} \right\}^{\frac{1}{2}} \quad (1.2)$$

where  $\overline{v^2}$  is the mean square spatial velocity fluctuation.

### 2.5.3 Vorticity

The vorticity field was computed as the rotational of the mean velocity:

$$\omega = \nabla \times \bar{v} \quad (1.3)$$

### 2.5.4 Sauter diameter

The Sauter diameter ( $d_{32}$ ) was introduced by J. Sauter in 1926 as the ratio of the sum of volumes of the spherically shaped fluid objects (air bubbles or oil droplets) to their surface area (Zlokarnik, 2001):

$$d_{32} = \frac{1 \sum d^3}{6 \sum d^2} \quad (2.7)$$

In spite of using this equation, many authors prefer to employ a reduced form (Yang *et al.*, 1986; Lovick *et al.*, 2005):

$$d_{32} = \frac{\sum d^3}{\sum d^2} \quad (2.8)$$

In order to compare our results, the present work uses Eq. 2.8.

### 2.5.5 Interfacial area

The Sauter diameter is related with the interfacial area per unit liquid volume:

$$a = 6 \frac{\varphi_V}{d_{32}} \quad (2.9)$$

where  $\varphi_V$  expresses the volume of the dispersed liquid phase or the gas hold-up ( $\epsilon$ ). To learn more about the dependence of the interfacial area, Eq. 2.7 was computed for the conditions most common found in the literature, for instance,  $0.01 \text{ mm} < d_{32} < 4 \text{ mm}$  and  $0.01 < \varphi_V < 0.2$ . As noticed in Fig. 2.5, the volume fraction of the dispersed phase ( $\varphi_V$ ) has a stronger influence on the interfacial area than the Sauter diameter has. This plot suggests that higher concentrated dispersion might overcome the effects of the flow forces intended for the fragmentation of the fluid elements present in the dispersion. However, in concentrated dispersions the probability for coalescence increases.

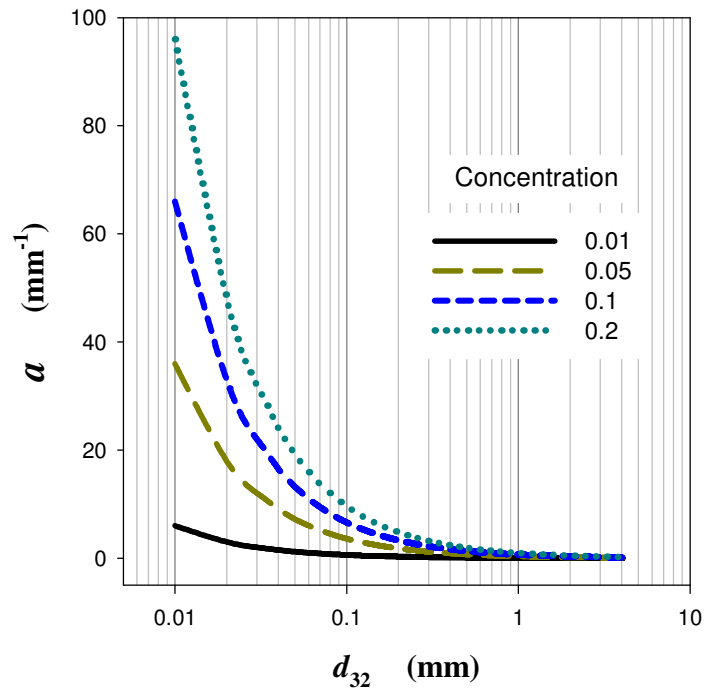


**Figure 2.5.** Interfacial area estimated for different diameters at different concentrations accordingly to Eq. 2.9.

### 2.5.6 Probability Density Function (PDF)

PDF was used to model the size distribution of the dispersed elements. The PDF for a normal distribution is computed as:

$$f(x) = \frac{1}{\sigma\sqrt{2\pi}} e^{-\frac{(x-\mu)^2}{2\sigma^2}} \quad (2.10)$$

$$\text{for } -\infty < x < \infty ; -\infty < \mu < \infty \text{ and } \sigma > 0$$

where  $\mu$  is the mean value,  $\sigma^2$  is the variance and  $\sigma$  is the standard deviation (Ramachandran and Tsokos, 2009). The PDF largest values correspond to the most likely values of the variable  $x$ , whilst the smallest values correspond for unlikely values.

### 2.5.8 Volume-related liquid-side mass transfer coefficient ( $k_L$ )

The liquid mass transfer coefficient,  $k_L$ , in the interface air-water was estimated accordingly to the equation proposed by Frössling (Alves *et al.*, 2004):

$$k_L = c \sqrt{\frac{v_s}{d}} D^{\frac{2}{3}} \nu^{-\frac{1}{6}} \quad (2.11)$$

where the constant  $c = 0.6$ ,  $v_s$  is the superficial gas velocity ( $v_s = f(T, Q_G)$ , Eq. 2.1),  $d$  is the bubble diameter ( $d_{32}$ ),  $D$  is the air diffusivity in water ( $2.11 \times 10^{-9} \text{ m}^2 \text{ s}^{-1}$ ), and  $\nu$  is the kinematic viscosity of the continuous phase ( $1 \times 10^{-6} \text{ m}^2 \text{ s}^{-1}$ ).

### 2.5.9 Turbulence energy rate dissipation

The specific local energy dissipation is defined as follows:

$$\varepsilon = \frac{P}{\rho V_L} \quad (2.12)$$

This property is known as the mean dissipation rate. For the present work  $\varepsilon = 0.00046 \text{ m}^2 \text{ s}^{-3}$ .

The turbulence energy rate dissipation ( $\varepsilon$ ) was determined in terms of a micro-scale and the turbulence velocity fluctuations (Sheng *et al.*, 2000):

$$\varepsilon = A \frac{v'^3}{l} \quad (2.13)$$

where  $A$  is a proportionality constant and  $l$  is the integral length scale.  $A = O(1)$  and the length scale can be determined in base of the impeller diameter:  $l = d_I / 10$ . The basis of the Eq. 2.13 is the energy cascade from large to small eddies (reference) and makes two assumptions: (1) exists local equilibrium between turbulence production (at the large, measurable scales) and dissipation (at the small, non-measurable scales) and, (2) as well as the existence of local isotropy at small scale nevertheless large scales are very anisotropic (Wu *et al.*, 1989). In practice, it is rather difficult to meet such conditions, especially in the flow produced in stirred tanks.

### 2.5.10 Kolmogorov micro-scale

The Kolmogorov micro-scale ( $\lambda$ ) was computed applying Eq. 1.3:

$$\lambda = \left( \frac{\nu^3}{\varepsilon} \right)^{\frac{1}{4}} \quad (1.3)$$

where the dynamic viscosity results from the relation between kinetic viscosity and density  $\nu = \mu/\rho$ .

## 2.6 Dimensional analysis

### 2.6.1 Reynolds number

Accordingly to Eq. 1.1, the flow regime in terms of the Reynolds number is  $Re = 24,500$ , which corresponds to the fully turbulent developed flow.

$$Re = \frac{\rho N d_I^2}{\mu} \quad (1.1)$$

where  $d_I$  is the impeller diameter,  $\rho$  and  $\mu$  are the water density and dynamic viscosity, respectively.

### 2.6.2 " $\phi$ " force

The " $\phi$ " force is given by

$$" \phi " = \frac{(2\pi N)^2 d_I}{2g} \quad (2.14)$$

where  $g$  is the gravitational acceleration ( $g = 9.81 \text{ m s}^{-2}$ ). To avoid flooding caused by radial impellers, Cooke *et al.*, (2005) suggested " $\phi$ "  $\geq 1$ . In the present work " $\phi$ " = 3.5.

### 2.6.3 Froude number

The Froude number is defined by

$$Fr = \frac{N^2 d_I}{g} \quad (2.15)$$

To avoid flooding caused by radial impellers, Cooke *et al.* (2005) proposed  $Fr \geq 0.05$ . In the present work is  $Fr = 0.18$ .

### 2.6.4 Weber number

Although the oil drops or the air bubbles interact between them through coalescence in highly concentrated dispersions. Hinze (1955) developed a theory for particle breakage, which established that drops and bubbles are fragmented as a function of the equilibrium between the external fluid force and the interfacial force:

$$We = \frac{\rho \overline{v^2} d}{\sigma_i} \quad (2.16)$$

where  $d$  is a characteristic length (i.e. the drop or bubble diameter,  $d_d$  or  $d_b$  respectively).

CHAPTER 3

*Hydrodynamics  
and  
viscous  
structures  
formation*

This chapter describes the flow pattern generated by the Scaba impeller and its hydrodynamics in terms of the 2D vector fields. The scalar of the velocity magnitude, the velocity fluctuation and the vorticity field are presented to investigate its influence on the viscous phase deformation and rupture. Visual recordings explain the oil immersion process and the filamentous viscous structures formed as a consequence of the hydrodynamics prevailing in the continuous phase flow. This subject introduces a new vision for the study of filaments generated in a mechanically stirred tank under turbulent flow conditions.

## 3.1 Flow field and oil filaments

### 3.1.1 Velocity patterns

The measurement of the velocity field around the impeller was obtained to understand the complex dynamics of the viscous phase. With these measurements we verified the advantages of the Scaba impeller as a stirrer device reported in the past by Kovács *et al.* (2001), Khopkar *et al.* (2004) and Cooke and Heggs (2005).

The velocity fields presented here for a single phase are not significantly affected by the presence of the viscous phase because the oil concentration is small (i.e. 1%  $v/v$ ), which is in good agreement with the findings reported by Laurenzi *et al.* (2009). The velocity field obtained for the plane  $rz$  at  $Re = 24,000$  is shown in Fig. 3.1a. Although some of the typical structures for the radial impellers are well reproduced (for instance, the toroidal structures), our attention focuses in the flow field produced in the core of the curved blades. In this region, the velocity vectors are highly convergent. Kovács *et al.* (2001) and Khopkar *et al.* (2004) observed that the flow discharged by a curved blade impeller is concentrated in the impeller centerline. One can notice that this structure does not occur for an impeller with flat blades such as the one produced by a Rushton Turbine, which produces mainly parallel velocity vectors (see for instance Baldi and Yianneskis, 2004; Laurenzi *et al.*, 2009). Cross flow is a good indication of the improvement of mass, momentum and energy transfer; shear rate and turbulence are also increased, and contribute to the deformation and breakage of dispersed structures like filaments, drops, bubbles or particles. Fig. 3.1b shows the magnitude of the velocity vectors for the plane  $rz$ . The largest velocity magnitude is found around



the blades discharge ( $|\bar{v}|_{max} \approx 0.5 \text{ m}\cdot\text{s}^{-1}$ ), whereas the flow in the rest of the tank is mainly characterized by  $|\bar{v}| \approx 0.1 \text{ m}\cdot\text{s}^{-1}$ . This value is low enough to suggest that the flow develops mainly in the  $r\theta$  plane. The impeller tip velocity was estimated as  $v_{tip} = d_I\pi N$ , resulting in  $v_{tip} = 1 \text{ m}\cdot\text{s}^{-1}$  (two times the maximum velocity of the liquid at the impeller discharge). The minimum velocities ( $|\bar{v}| < 0.05 \text{ m/s}$ ) were registered in the core of the eddies. Once the velocity profile was known, the pumping capacity was computed according to Eq. 2.4 and the resulting value  $N_Q = 0.46$  is in agreement with the values reported by Kovacs *et al.* (2001) and Khopkar *et al.* (2004).

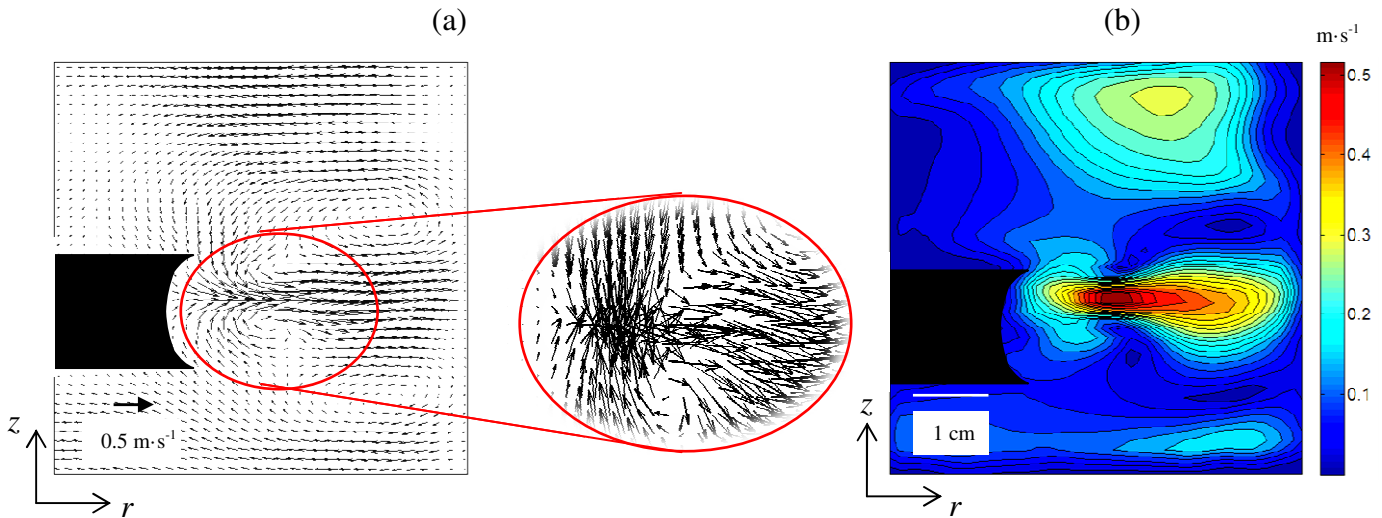


**Figure 3.1** (a) Velocity vector field and (b) Scalar field of velocity magnitude.  $Re = 24,000$ . Both cases represent the time average of the flow.

To understand the way in which the oil is transported and dragged towards the impeller, we analyzed the magnitude of the axial velocity component of the average velocity field. The time average velocity  $v_z$  is compared along the  $z$  direction for several radial positions in Fig. 3.2. Again, maximum values are obtained around the impeller zone, but the velocity direction in the upper zone is opposite to that located in the lower zone. The inflow ( $v_z^-$ ) generated in the upper zone explains why the oil, originally located at the water surface, is smoothly incorporated toward the tank center, around the impeller shaft once the rotation of the impeller starts. Then, the oil forms thick threads that are twisted and driven in a helical manner around the shaft. The process continues until the oil contacts the impeller blades. A visual description of this process is shown in Fig. 3.4.

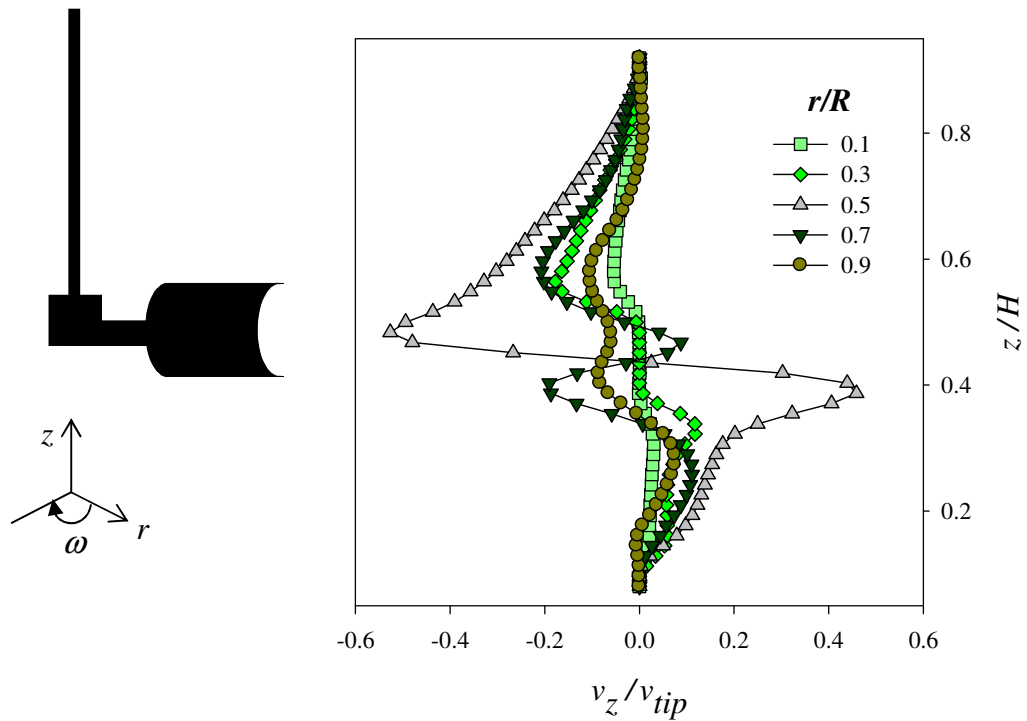


**Figure 3.2.** Axial velocity profiles along the  $z$  axis for selected radii ( $r/R$ ).  $v_{tip}$  and  $H$  refer to the impeller tip velocity and the liquid maximum height, respectively.

### 3.1.2 Oil dragging

This process takes place mainly in the region near the impeller shaft, in which the oil phase is submerged and dragged into the liquid bulk as thick oil threads, which are twisted and driven in a helical manner around the shaft. The process continues until the oil contacts the impeller blades. A visual description of the dragging process is showed in Fig. 3.3. There is a good agreement between the oil dragging and the velocity profile as shown in the last photograph of such a figure.

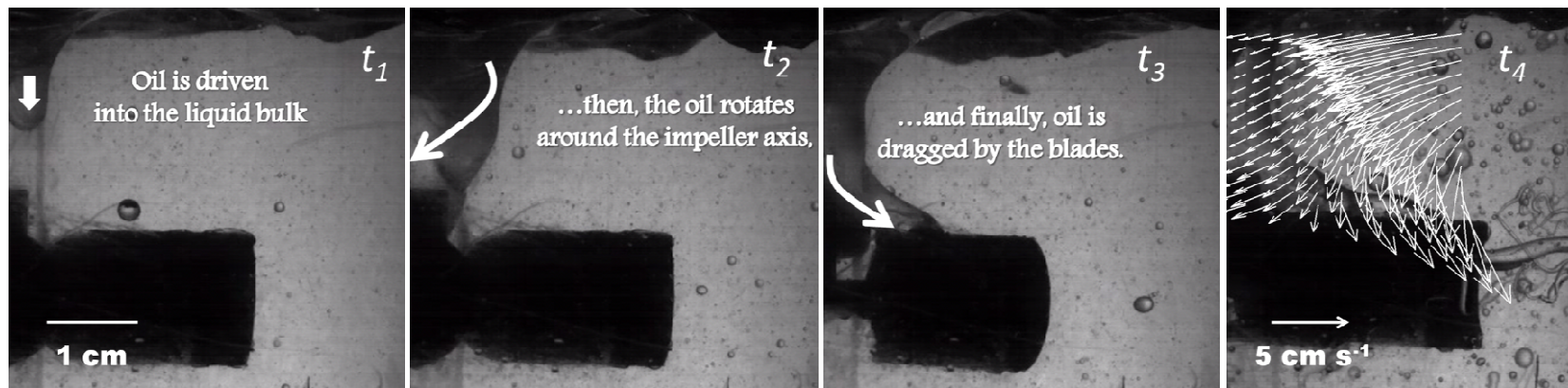


**Figure 3.3.** Oil dragged from the surface to the impeller tips. ( $t_1 = 0$  ms,  $t_2 = 195$  ms,  $t_3 = 210$  ms and  $t_4 = 385$  ms). In the last photograph, the mean velocity pattern governing the process is also shown.

### 3.1.3 Filamentous structures

The radial flow from the impeller is highly stretched. Elongated and thin filaments as well as other amorphous thicker structures are formed and expelled from the impeller blades to the turbulent flow. Shinjo and Umemura (2010) observed similar structures, which were described as fungus-like shapes. We have observed that in the impeller zone, inertial forces elongate the filaments and fold them in all directions. These elongated filaments undergo a very interesting process (Fig. 3.4) that resembles the description of Yarin (1997) for hairpin vortices.

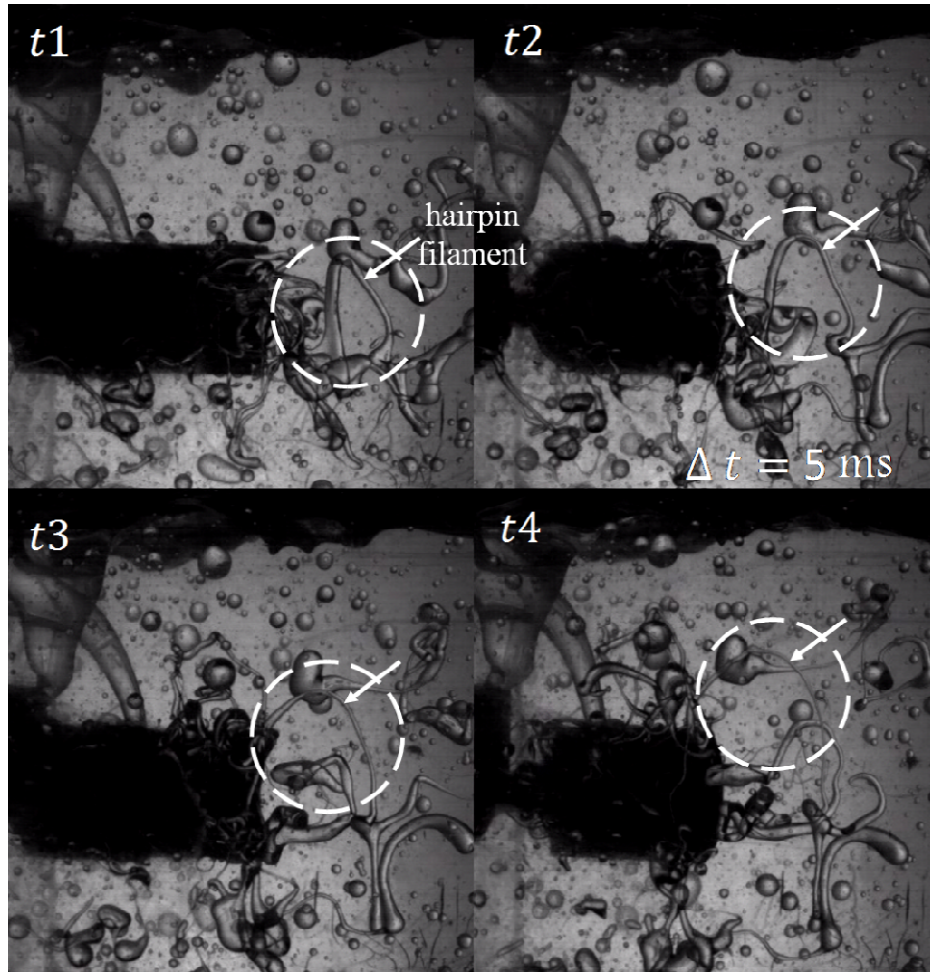


**Figure. 3.4.** Deformation process of a hairpin filament. Time difference between frames is 5 ms.

Furthermore, the radial flow produced at the impeller discharge is not steady. In fact, it is composed by intermittent jets. The strength of each jet depends on the tangential and radial position of the blade, as shown in Fig. 3.5. The jet velocity increases depending on two parameters: the number of blades ( $n$ ) and the rotational speed ( $N$ ) [ $f = \frac{1}{n}N = 0.8 \text{ s}^{-1}$ ]. The oil filaments

dragged by the impeller blades are expelled in the radial direction towards the tank wall as a result of these periodic fluid pulses. However, once expelled, the jet energy ceases and the impulse that initially pushed the filament vanishes.

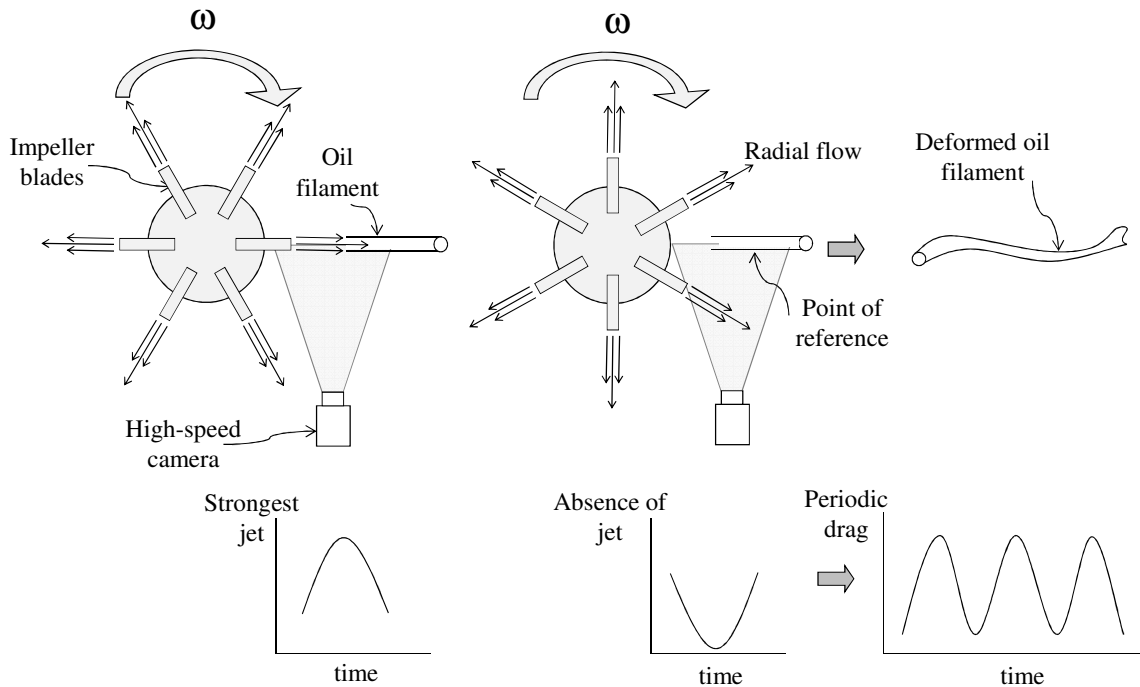


**Figure 3.5.** Schematic representation of the intermittent flow produced by the rotation of the impeller (top view).

In Fig. 3.6a, the normalized velocity measured during 60 ms after two filaments were injected onto the liquid in the plane  $rz$  is presented. The crests correspond to the instant when the jets drive out the maximum strength and the valleys correspond to the moments when the blades are not generating a jet. Once the filament escapes from the zone of high turbulence (i.e.  $r/R = 0.8$ , near the tank wall), the jet has no further influence and the radial displacement of the filament disappears. Such intermittences cause the filament to fold and break. An example of folding produced by this periodic perturbation is shown in Fig. 3.6b. Such detailed observations showing the dynamics of viscous filaments have not been yet reported for the case of mixing tanks. For a better understanding, the complete image sequence is available in the following website <http://arxiv.org/abs/1010.4195v1> hosted by the American Physics Society, Division of fluids (Sanjuan-Galindo *et al.*, 2010). This video shows how oil elements are deformed, randomly elongated, folded and stretched in the stirred tank. These events have been reported in the specialized literature in liquid mixing (Iranshahi *et al.*, 2007, Sanjuan-Galindo *et al.*, 2011) but visual evidence of the process is still limited.

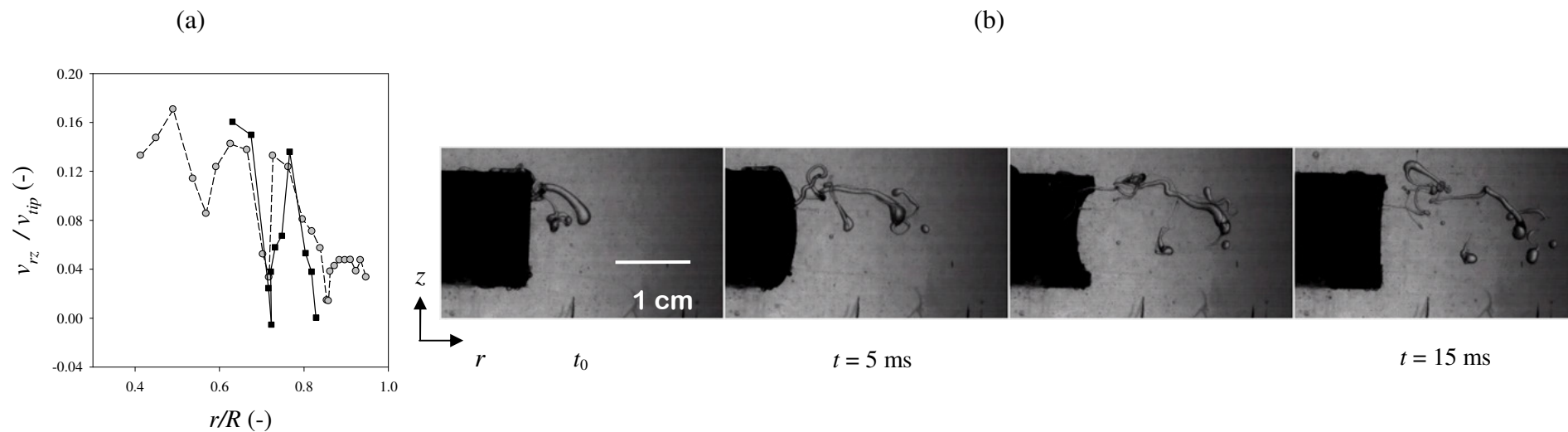


**Figure 3.6.** (a) Normalized velocity of two filament points displaced in the plane  $rz$  measured during 60 ms ( $v_{tip}$  refers to the impeller tip velocity, and  $R$  represents the tank radius). (b) Velocity intermittence effect in the filament stability.

## 3.2 Turbulent flow effects

### 3.2.1 Turbulence intensity

In previous works some authors discussed that in the impeller neighborhood the flow is governed by shear forces and turbulence fluctuations (Calabrese *et al.*, 1986a). Our experiments support this statement and provide evidence of the influence of turbulence on the deformation and breakage of viscous filaments, which lead to drops formation.

Fig. 3.7a shows a scalar map and the mean fluctuating velocity field,  $v'$ , in the plane  $rz$  in the impeller neighborhood. High turbulent motion values, i.e.  $v' = 0.5 \text{ m s}^{-1}$ , are present near the impeller discharge. Fig. 3.7b shows a typical viscous structure produced randomly as a result of the turbulent flow.

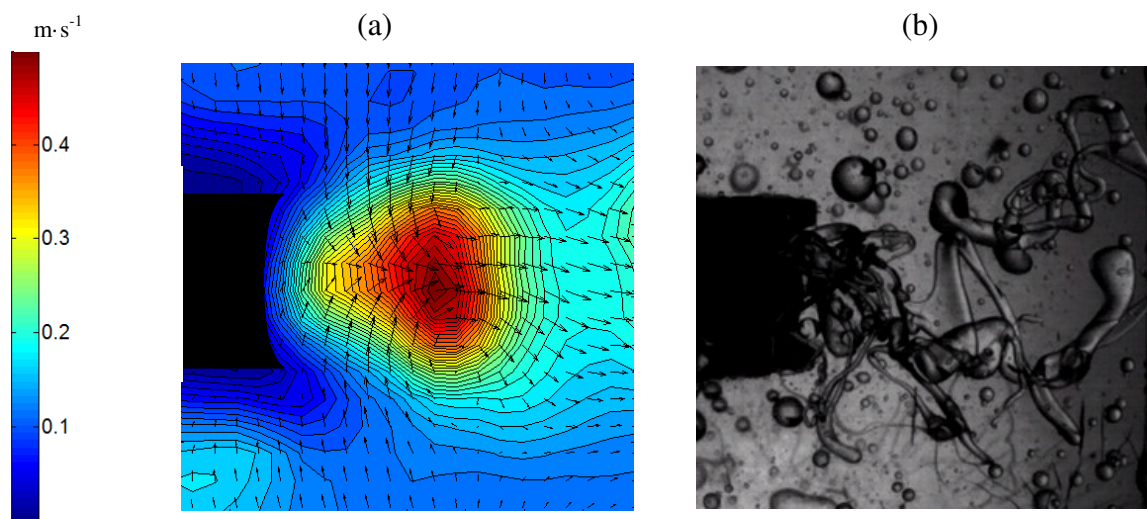


**Figure 3.7.** (a) Turbulence intensity and velocity fields. (b) Filament instability.

Filaments can be observed in the tank only in the beginning of the process (during the first 60 s); thereafter, they are broken and the continuous media becomes saturated with drops. The comparison of the turbulence intensity in the different zones helps to explain the evolution process of the drops size (as will be described below). Outside of the impeller discharge, the liquid turbulence decreases drastically (i.e.  $v' < 0.2 \text{ ms}^{-1}$ ) and surface forces become stronger than inertial ones allowing the recoil of broken filaments (drop formation).

### 3.2.2 *Vorticity field*

In Fig. 3.8a two vorticity regions of opposite sign (with absolute magnitudes of  $0.06 \text{ s}^{-1}$ ) can be identified. A similar interaction was reported by Shinjo and Umemura (2010), who studied the influence of the vortices on the filament surface and breakage. The vortices in our stirred tank are generated in a similar way; they are located symmetrically in both sides of the impeller centerline. The oil phase expelled by the impeller is attracted by the low pressure region of the vortex cores and driven by the radial flow discharged by the impeller. The result is the formation of complex structures like those shown in Fig. 3.8b. In this image the velocity vectors were superposed to the image in order to explain the influence of the radial flow. These structures are unstable and result from a process of tridimensional stretching; thin viscous sheets are also produced but they are unstable and highly sensitive to rupture. After breakage the superficial forces become dominant allowing the recoiling of broken filaments, especially in the region of low turbulence (as explained above). This process ends with the formation of numerous drops of widely different sizes. Quickly afterwards, these drops are dispersed in the liquid bulk.



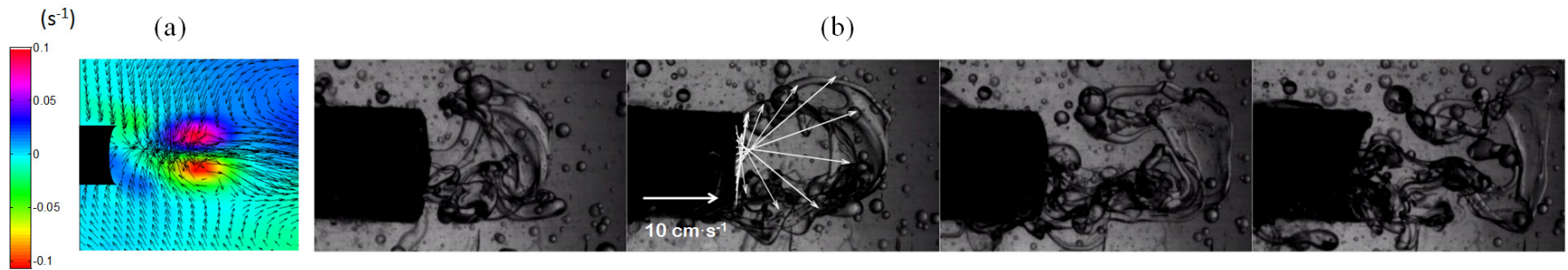


**Figure 3.8.** (a) Vorticity and velocity field, (b) Filament expelled by the impeller blades.

CHAPTER 4

*Mass transfer  
and  
fragmentation*

This chapter describes the particle size distribution of the dispersion components. Variables related with the mass transfer process were estimated like the interfacial area and the  $k_{La}$  coefficient from *in situ* measurements. During the stirring process, the oil fraction or the biomass content remained constant while the gas flow was supplied continuously. The dimensionless Weber number was estimated in two zones of the liquid bulk with different turbulence properties. The size of the air bubbles, oil drops and fungus pellets was measured; however, the oil drops and the fungus pellets experienced fragmentation as a function of the stirring time. An explanation that describes the fragmentation process is also given at the end of this chapter.

## 4.1 Stretching, breakage and mass transfer

### 4.1.1 Air bubbles and distribution

There are many studies where gas bubbles are considered as buoyant objects moving in still liquid columns (Bouaifi *et al.*, 2001; Soto *et al.*, 2006; Van den berg *et al.*, 2006); under such conditions, the gas bubble movement supplies the only flow perturbation and the gas transport is preferentially ascendant, promoted by the air low density and pressure gradients. Oppositely, the bubbly flow developed in stirred tanks is more complex because the gas bubble buoyancy is extensively altered by the energy supplied by the impeller, so that the velocity gradients contribute to the bubble stretching and its eventual rupture.

Gas bubbles distribution in the liquid bulk in stirred vessels has been determined by experimental and numerical studies (Yang and Shen, 1986; Alves *et al.*, 2004; Taboada *et al.*, 2006); but the mechanism through the which, the gas bubbles disrupt has not been completely clarified. In particular, a visual documentation of the process has not been reported to date. The velocity gradients induced by the impeller discharge stretch and break the viscous fluid structures. An approach of the mechanism occurred in a stirred tank was proposed by Andersson and Andersson (2006), who described the deformation and breakage process of single bubbles injected in a turbulent flow in a straight pipe.

Fig. 4.1a shows an instant of the gas-liquid dispersion inside the reactor for an aeration rate of 0.5 vvm and  $Re = 24,500$ . Spheroidal gas bubbles are reshaped into lenticular ones. This fact occurs only in the zone of the impeller flow discharge where high levels of turbulence prevail, i.e.  $v' \approx 0.5 \text{ m s}^{-1}$ . Deformed drops are the previous step for rupture. Bubble breakage obeys the force balance represented by the Weber number.

$$We = \frac{\text{Inercial forces}}{\text{Interfacial forces}} = \frac{\overline{\rho v^2} d_b}{\sigma_i} \quad (2.16)$$

Bubbles are broken as the interfacial forces become lower than the inertial forces. Hinze (1955) reported that bubbles breakage when the Weber number reach a critical value; for instance,  $We_{crit} = 1.2$ . At higher Weber numbers, bubbles are deformed, whilst lower Weber values are not significant to disturb the equilibrium of the interfacial force. For the conditions here evaluated, the estimated values are  $We \approx 3$  around the high turbulent region (i.e. in the flow discharged by the impeller), while in the low turbulent zone (i.e. far away from the impeller discharge)  $We \approx 0.15$ . As Fig 4.1a shows far away from the impeller discharge, air bubbles keep a spheroidal shape due to the predominance of the surface forces. The mechanism to explain the deformation and the breakage of the fluid elements will be revisited at the end of this chapter.

The probability density function (PDF) versus the bubble diameter is plotted in Fig 4.1b. Bubble size distribution develops a Gaussian-like bell with a tail on the right side. The average diameter (and the standard deviation) obtained are:  $d_{av} = 1.2 \text{ mm}$  ( $\sigma = 0.6 \text{ mm}$ ). The maximum bubble diameter is  $d_{max} \approx 3.9 \text{ mm}$  (nearly three times the average magnitude  $d_{av}$ ). To enrich this information, the gas hold-up distribution in the liquid bulk is subsequently analyzed. The image for the gassed flow (0.5 vvm) showed in Fig. 4.1c corresponds to the overlapped sequence recorded during 1.5 s at 400 fps in the steady state. It should be noticed that air volume occupies mainly the upper part of the impeller and the neighborhood of the tank wall, while in the zone placed below the impeller, the gas is poorly distributed; which is a good agreement with the findings reported by Gimbut *et al.* (2009) with a numerical model for a similar impeller. The experimental results obtained in the present work confirm the theory proposed by Cook *et al.*, (2005), who evaluated two parameters to study the gas phase distribution produced by radial impellers in stirred tanks: the “ $\mathcal{G}$ ” force (Eq. 2.14) and the Froude number (Eq. 2.15). For the present work, “ $\mathcal{G}$ ” = 3.5 and  $Fr = 0.18$ . From this reference, the power supplied through the

agitator exceeds the gas buoyancy and disperses well the gas phase in the upper part of the tank; to increase the gas phase dispersion in the bottom tank higher power inputs are required.

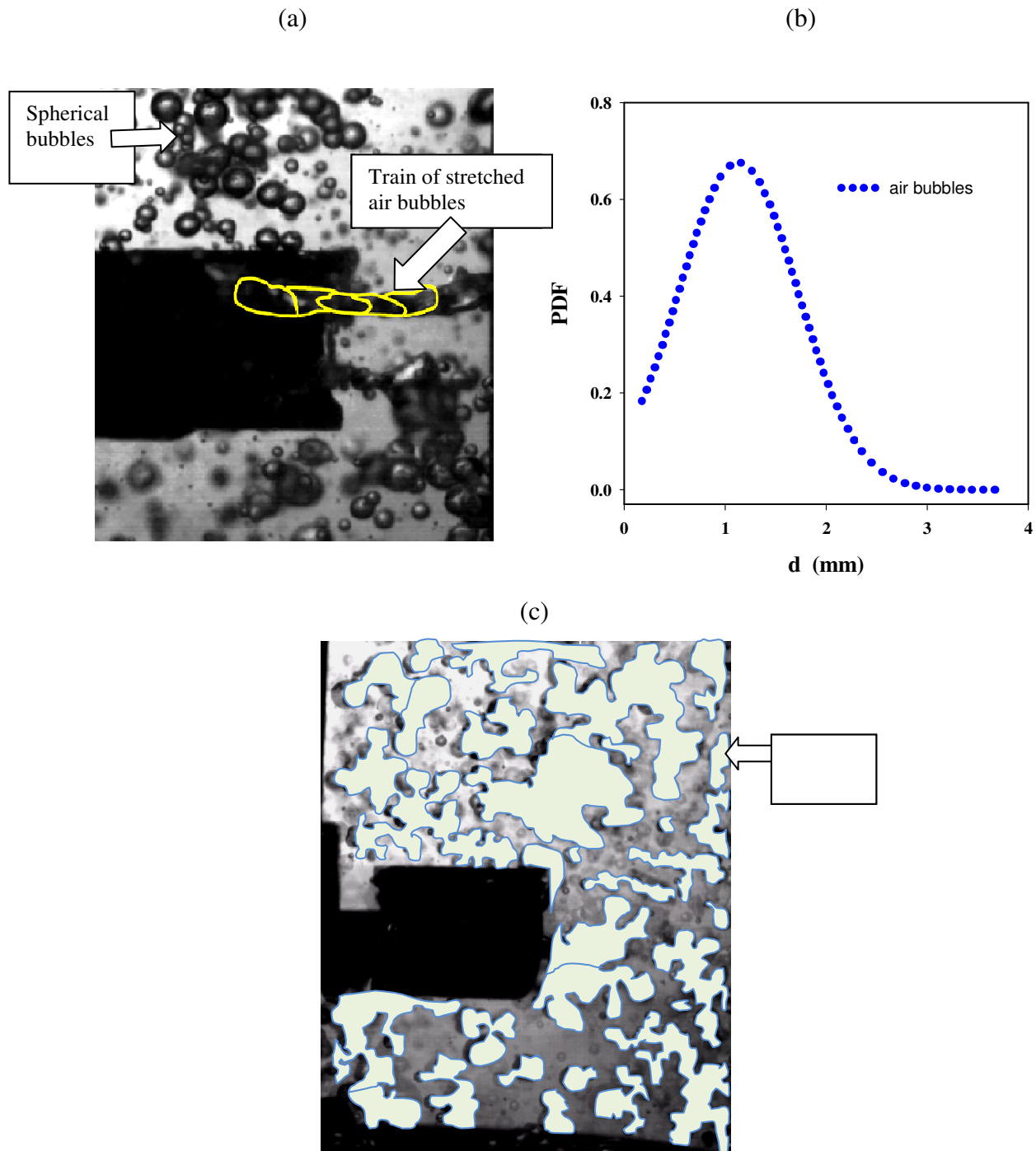


**Figure 4.1.** (a) A typical image of air-water dispersion showing deformed bubbles and (b) PDF distribution of air bubble diameters. (c) Overlapped images showing air distribution produced during 1.5 s in a stirred tank at  $Re = 24,500$  for an aeration rate of 0.5 vvm.

### 4.1.2 Gas-liquid mass transfer coefficient

In spite of reporting the arithmetic average ( $d_{av}$ ), many authors determined the Sauter diameter ( $d_{32}$ ) (Eq. 2.8) (Lucatero *et al.*, 2003; Gimbun *et al.*, 2009), which is the same obtained in this work. In the past, Laakkonen *et al.* (2007) found the range  $3.0 \text{ mm} < d_{32} < 3.6 \text{ mm}$ ; whilst Gimbun *et al.* (2009) reported  $2.8 \text{ mm} < d_{32} < 5.3 \text{ mm}$ . The Sauter diameter obtained in the present work is  $d_{32} = 1.82 \text{ mm}$ . Such value is smaller than those reported previously by Laakkonen *et al.* (2007) and Gimbun *et al.* (2009); however, the experimental conditions were not the same. In those works they used a Ruston turbine, unequal flow regimens and different aeration rates. Other authors have proposed empirical correlations to predict the Sauter diameter as a function of different parameters like the specific power input, the impeller rotational speed, the gas holdup, the liquid properties, the flow velocity, etc. (Clarke and Correia, 2008); nevertheless, these equations were obtained for experimental conditions not comparable to the present work.

The Sauter diameter was helpful in the estimation of the specific interfacial area  $a_{Air-H_2O} = 548 \text{ m}^{-1}$  (Eq. 2.9). Applying Eqs. 2.7 and 2.10, the overall mass transfer obtained from the experimental data is  $k_L a = 0.007 \text{ s}^{-1}$ . There is some difficulty to compare this value with the data published elsewhere due to the wide divergence of the methods used to determine the  $k_L a$  coefficient as well as in the experimental conditions reported by other authors. For example, using the peroxide decomposition technique, Alves *et al.* (2004) reported a  $k_L a = 0.017 \text{ s}^{-1}$  for a larger aeration rate, moreover, they employed a Rushton turbine at  $Re = 69,000$ . In a CFD model, Laakkonen *et al.* (2007) computed a vessel with higher aeration rates and predicted local values ranging from  $0.03 \text{ s}^{-1}$  to  $0.01 \text{ s}^{-1}$ . From a photographic method but different stirring conditions Pulido-Mayoral and Galindo (2004) determined a local coefficient  $k_L a = 0.005 \text{ s}^{-1}$ .

### 4.1.3 Time dependence of drop size

Oil drops break in the similar way as described above for the gas bubbles. Fig. 4.2 shows an image sequence of this process: a drop is pushed by the impeller jets (the oil content is 1% v/v and  $Re = 24,500$ ). Under shear forces, spheroidal drops are stretched and reshaped. If bulbous shapes are attained a necking process can cause breakage and give rise to smaller daughter droplets.

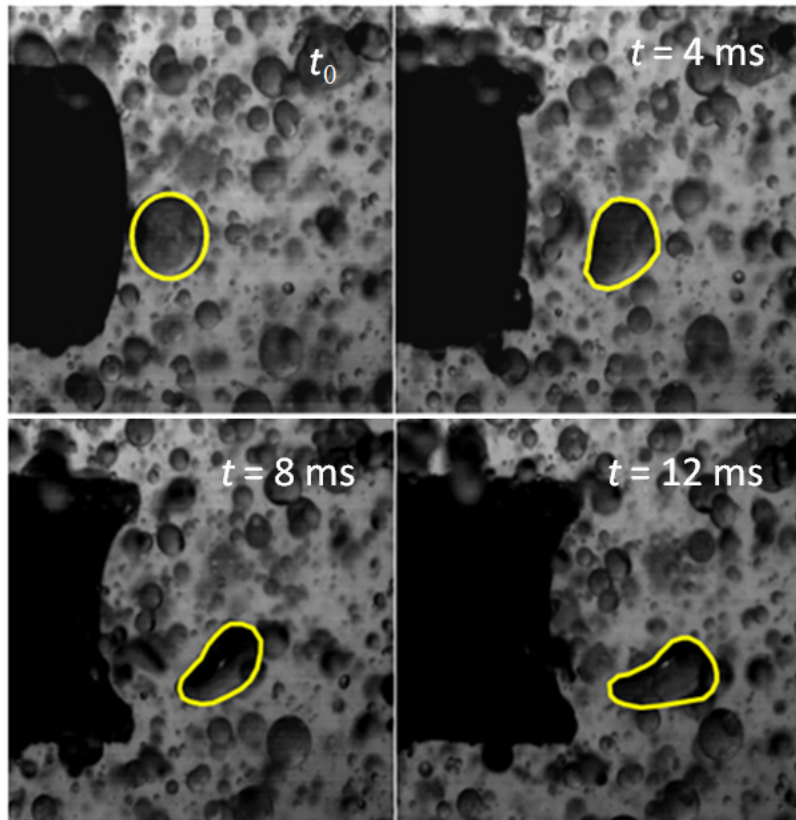


**Figure 4.2.** Image sequence of the deformation of an oil droplet near the impeller discharge.

Drops size distribution for different kinds of dispersions in the steady state produced in stirred contactor devices has been studied by Calabrese *et al.*, 1986a; Chatzi *et al.*, 1991, Zhou and Kresta, 1998b; Sajjadi *et al.*, 2002; Lovick *et al.*, 2005, among others. In the present work, the drop size was studied as time dependent. Two sets of photographs were obtained at different times during the tank operation for a fixed impeller speed. The first set of images was captured after the stirring process started and once filaments were disrupted ( $t = 120 \text{ s}$ ); the second set was taken one hour later. Fig. 4.4a compares both images. When the agitation has started, big drops are predominant and easily found.

The diameter of approximately 500 drops for each time was obtained and its size distribution exhibits a Gaussian-like distribution (Fig. 4.4b). As showed by Zhou and Kresta (1998b), the drop size is time dependent before a steady state can be reached. The widest curve describes the dispersion in the beginning of the process whilst the largest agitation time is described by the narrowest one. The PDF curve displaces towards the left (smaller diameters) as the stirring time

increases, confirmed by the curve's peak; i.e. the average diameter (and the standard deviation) obtained in the two stages are  $d_{av} = 1.1$  mm ( $\sigma = 0.41$  mm) at  $t = 2$  min, while  $d_{av} = 0.8$  mm ( $\sigma = 0.25$  mm) at  $t = 60$  min. The tail at the right side of the PDF corresponding to the earlier time is produced by the large size drops appearing in the beginning of the process. The ratio ( $d_{max}/d_{av}$ ) migrates from 2.7 to 2.3 as the stirring time increases, which leads to the increment of the interfacial area resulting in better mass transfer process. A disadvantage is that resolution discards the small droplets; to overcome this difficulty, drops measurement from a magnification view were carried out in the steady state. These results were integrated to estimate the Sauter diameter  $d_{32}$  and the oil-water interfacial area, which will be presented in the next chapter.

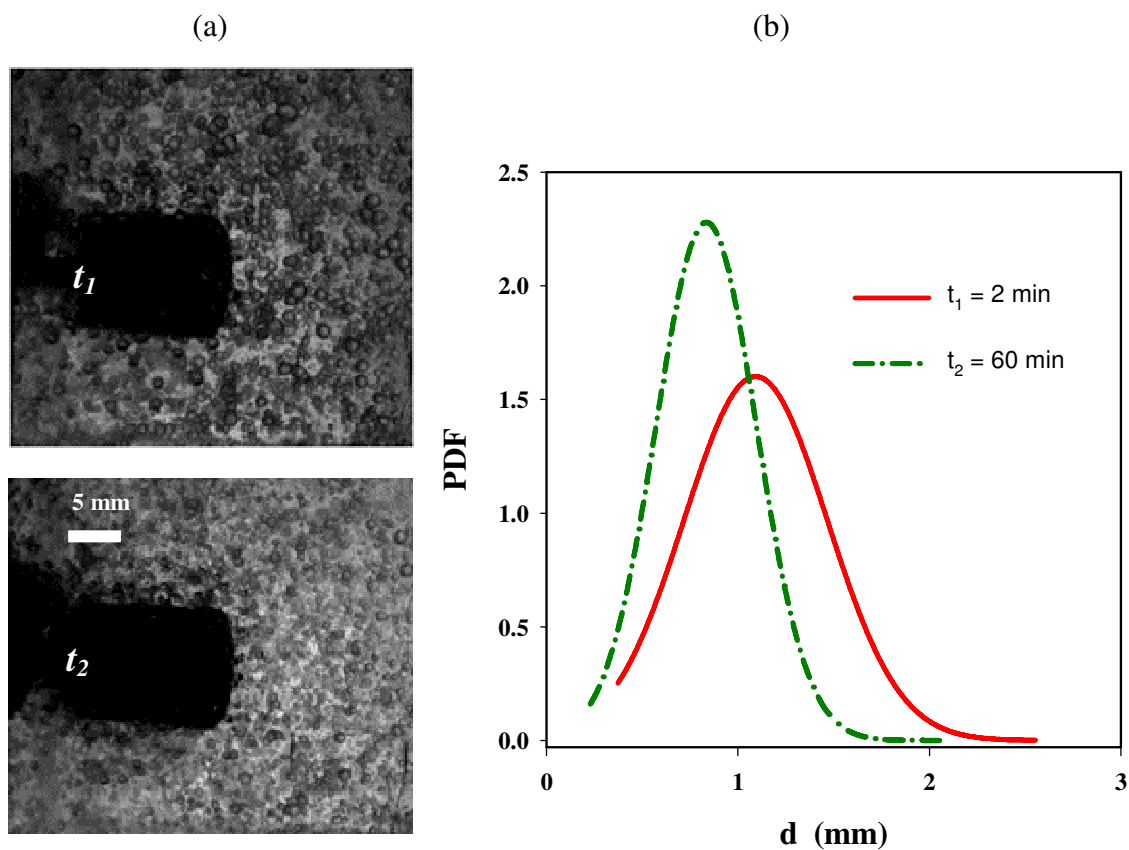


**Figure 4.3.** (a) High-speed images of an oil-in-water dispersion produced in a stirred tank. Pictures were taken at  $t_1 = 2$  min and  $t_2 = 60$  min after the agitation process started. (b) PDF of drop diameter obtained at  $t_1$  and  $t_2$ .

At the beginning of the process, oil drops breakage occurs more frequently because big drops are more unstable than the smaller ones. It is unlikely that all drops reach a uniform size but there is a



debate about drops size distribution. Some authors have predicted the minimum size considering the theory of Kolmogorov (Liu and Li, 1999), but others have discarded this prediction (Zhou and Kresta, 1998a; Cristini *et al.*, 2003). Several correlations have been developed to predict the biggest drop or the mean size, especially for several silicon oils or petroleum products (Coulaloglou and Tavlarides, 1976; Calabrese *et al.*, 1986b; Wang and Calabrese, 1986; Zhou and Kresta, 1998a) but not for oils used in biochemical processes, such as the Castor oil. It has also been suggested that mechanical impacts of the drops with the baffles or with the tank wall may also influence on the drop size distribution. However, we did not observe the occurrence of such events with enough frequency to be considered as a relevant factor. In agreement with the work of Cristini *et al.* (2003), we believe that drop breakage is caused mainly by the shear forces generated in the impeller discharge region. The dimensionless Weber number validates this fact:

$$We = \frac{\overline{\rho v^2} d_d}{\sigma_i} \quad (2.16)$$

As earlier mentioned, a critical value of the Weber number ( $We_{crit} = 1.2$ ) produces oil elements breakup; higher values induce strong deformation and for lower values, the drop shape remains unchanged. For the high turbulent region the resulting values are  $We \approx 4$ , while in the low turbulent zone  $We \approx 0.2$ , which supports that breakage is caused by the fluid forces.

#### 4.1.4 Biomass

Mechanical stirring in liquid fermentations plays two important functions: (1) to disperse the ingredients and (2) to keep them in contact. In the past, the hydrodynamic effects in the cellular growth have been investigated mainly based on the biomass production by comparing certain physiological functions or by testing the metabolic activity; for example, the proteins, enzymes or polymers production, DNA synthesis etc. (Abu-Reesh and Kargi, 1989). Under high agitation stress conditions, single cells can survive (Oh *et al.*, 1989; Wu, 1995; Maranga *et al.*, 2004) but cell clumps are more sensitive to strain, so they become fragmented (Rocha-Valadez, 2005; Rodríguez Porcel *et al.*, 2005). The effects of the nutrient sources in the fungus pellets size and morphology, grown in bioreactor, have been reported previously (Liao *et al.*, 2007); nevertheless, the influence of the flow patterns in the cluster size has received less importance.

This section analyzes the size alteration of fungus pellets of the strain *P. ostreatus* P50 exposed to constant stirring at  $Re = 24,500$ . Fig. 4.5a shows three gray-scale photographs of samples taken at different times: 15 min, 60 min and 300 min. The first photo represents the earliest time and exhibits largest size pellets. As the stirring time increase, the number of fragmented pellets increases also (Fig. 4.5a, right side photos).

The plot showing the PDF versus the pellet perimeter is presented for the three stirring times in Fig. 4.5b. The average values determined for the perimeter (and the standard deviation) are: 3.0 (1.7), 2.7 (1.3), 2.1 (1.0) (all magnitudes are given in mm) for the 15 min, 60 min and 300 min samples, respectively. In the three cases, the PDF shape remains unchanged; however, a clear displacement towards the smallest perimeter is observed and the curve width becomes narrower as the stirring time increases, which suggests that the pellet size reduction is caused by the flow pattern, particularly, by the vortices and the turbulence intensity produced in the impeller flow discharge.

The findings presented here are in agreement with the experiments of Rodríguez Porcel and coworkers (2005). They found that the maximum fungus clusters size is reached in the first hours of the fermentation process, but afterwards the fungus pellets size decreases. A possible explanation to this behavior is given next. Larger clumps are composed by young and healthy hyphae, while in mature cultures, the old hyphae are more sensitive to the flow forces.

The biomass here analyzed had the same maturity (because cell reproduction was inhibited). The results presented in the PDF curves suggest that pellets with a length larger than 2 mm (about 6 mm of perimeter) are fragmented as a consequence of the turbulence energy dissipation rate; higher levels of energy dissipation should produce smaller pellets.

Moreover, these results enhance the theoretical approach discussed by Li *et al.* (2002), who suggested that pellets fragmentation occurs when the local shearing forces are larger than the hyphal tensile strength; but until date, this rupture was not associated to a specific flow pattern. Larger fungus pellets are rather growth in shake flasks (Liao *et al.*, 2007) –which subject to medium to lower agitation stress and softer low turbulent conditions-, than in stirred tanks (Rocha-Valadez *et al.*, 2005).

It should be recalled that this experiment was performed in the absence of microbial activity. In a real fermentation process, cell growth and cell byproducts produce considerable increments in the culture broth viscosity, which reduces the agitation regime and increases the stagnant regions (Serrano-Carreón *et al.*, 1997; Rodríguez Porcel *et al.*, 2005; Sanjuan-Galindo, 2006) leading to larger sizes. Moreover, other factors like the fungus strain, the inoculation size and the carbon source, play an important role in the size of the fungal aggregates.

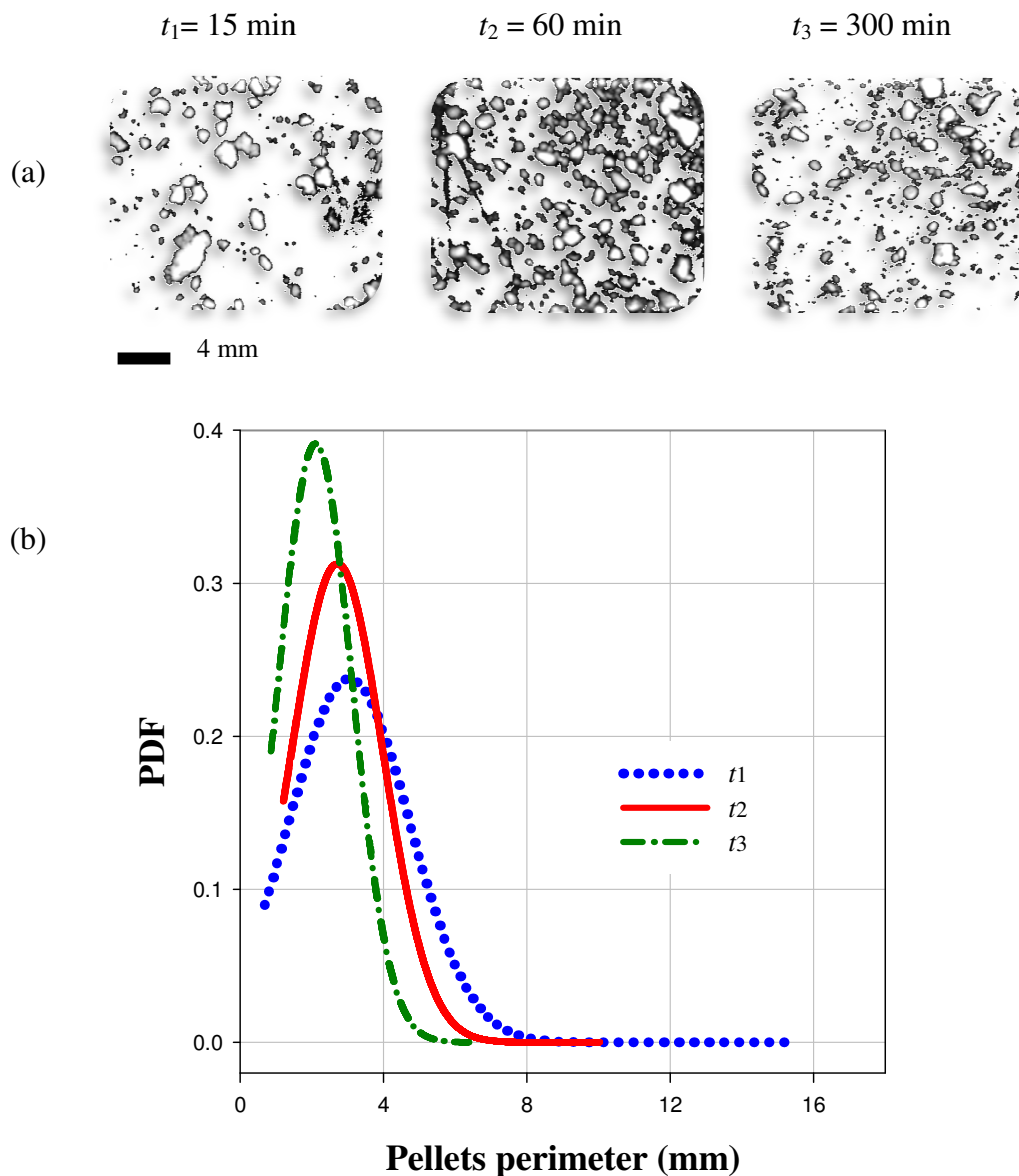


**Figure 4.4.** (a) Gray-scaled images of the pellets in agitation taken at  $t_1 = 15$  min,  $t_2 = 60$  min and  $t_3 = 300$  min after the agitation process started and (b) the corresponding PDF to compare the pellet perimeter in the three cases.

## 4.2 Mechanism to describe the particle size reduction

### 4.2.1 Force competition

The objects stability in a stirred dispersion depends on the equilibrium of the forces present in the turbulent flow: drag ( $F_d$ ), weight ( $mg$ ), pressure ( $F/A$ ), fluid acceleration plus mass effects ( $ma$ ), buoyancy ( $F_b$ ), surface tension ( $\sigma$ ), friction ( $F_f$ ), spinning ( $\omega$ ), shear forces ( $F_s$ ) fluid volume vorticity, lift force ( $F_l$ ) (which is responsible for the accumulation of bubbles in vortices) or impact ( $F_c$ ) (for instance, drops, bubbles or solid particles collide with each other or eventually with the solid parts of the agitations system or with the vessel) (Auton, 1987). A diagram showing these forces is depicted in Fig. 4.5. The ionic strength produced by salts, pH gradients or surfactants (i.e. proteins) are other factors, needed to be considered (Pulido-Mayoral and Galindo, 2004).

However, the effect of these forces is a function of some variables such as the particle size, the body inertia, the local dissipation rate, and the physical properties. In the process to reach the size equilibrium, objects are deformed or fragmented, producing smaller objects; this fact was corroborated with the dimensionless Weber number (Eq. 2.16) and the comparison of the PDF curves. Just after the most stable size is reached, higher energy should be supplied for a further size reduction. The interfacial tension for the air-water interface ( $\sigma_{a-w} = 72$  mN/m) is greater than the oil-water interface ( $\sigma_{o-w} = 21$  mN/m), which explains why the gas bubbles are bigger than the oil drops, when the two phases are submerged in the same flow pattern (compare the PDF curves shown in Fig. 4.1 and Fig. 4.4); for instance, the diameter ratio for the two phases in the equilibrium state, considering the average magnitude, is  $d_{gas}/d_{oil} = 1.96$  (dimensionless).

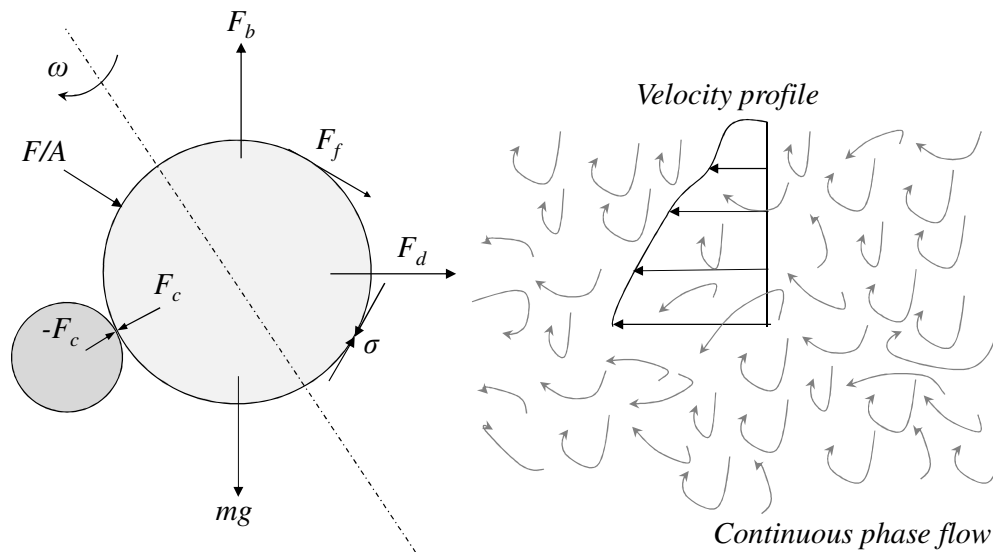


**Figure 4.5.** Free body diagram showing the presence of the forces acting in a stirred tank.

#### 4.2.2 Turbulent energy dissipation rate

Turbulent energy dissipation rate is transferred from the continuous phases to the non-miscible fluid elements (i.e. air bubbles or oil drops) to compensate the surface increment (size reduction), as proposed previously (Zhou and Kresta, 1998a). Fig. 4.6 shows the scalar field of the turbulence energy rate dissipation estimated from the dimensional analysis (Eq. 2.13). The flow in the impeller core is featured by  $\varepsilon = 18 \text{ m}^2 \text{ s}^{-3}$  (dark brown shade). This value is too large with respect to the specific energy dissipation in the tank volume:  $P/\rho V = 0.00046 \text{ m}^2 \text{ s}^{-3}$ , suggesting the predominance of other forces such as the interfacial tension; therefore, the dispersed elements might be rarely perturbed outside the impeller discharge. Table 2 are a comparison of the maximum dissipation rate reported in the literature for different agitator designs; as can be inferred, calculation of the turbulent energy dissipation rate is sensitive to the method and procedure (Sheng *et al.*, 2000).

According to Eq. 1.3, the local Kolmogorov micro-scale is  $\lambda \approx 1.5 \times 10^{-2} \text{ mm}$ . This value references the smallest eddy where energy is converted into heat and describes the predominance of the turbulent inertial regime; in other words, dispersed elements are larger than the smallest turbulent eddies and fragment into smaller elements.

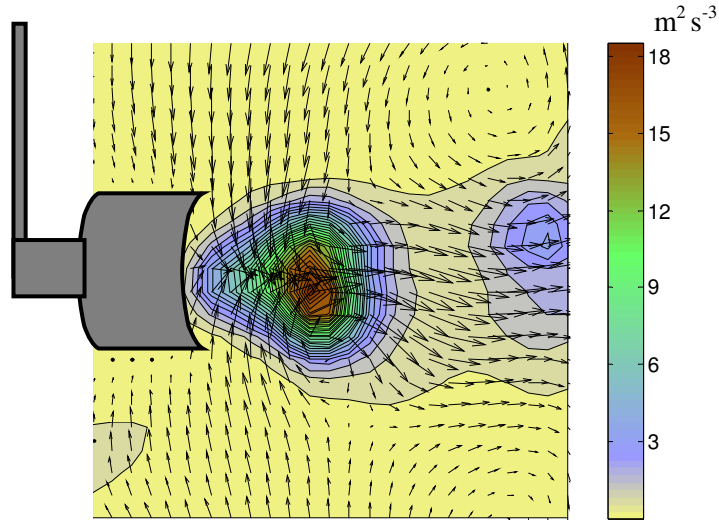


**Figure 4.6.** Turbulence energy dissipation rate in the impeller flow discharge.

**Table 2.** Maximum values reported in the literature for the turbulent energy dissipation rate.

Impeller design, ( $Re \cdot 10^3$ )	Maximum turbulent energy dissipation rate $\varepsilon_{max}$ ( $m^2 s^{-3}$ )	* Method	Reference
Scaba, (24)	18	<sup>1</sup> Dimensional analysis	The present work
Rushton,(4.6)	0.07	<sup>2</sup> Triple decomposition of Reynolds and Hussein's	Sharp and Adrian, 2001
Rushton (40)	311	<sup>3</sup> Reynolds stress gradients	Baldi <i>et al.</i> , 2004
Rushton, (32)	3.5	<sup>1</sup> Dimensional analysis	Ducci and Yianneskis, 2005
Rushton, (40)	0.12	<sup>4</sup> Reynolds average subgrid scale	Xinhong <i>et al.</i> , 2008
Hydrofoil, (13)	2.2	<sup>5</sup> Large Eddy PIV approach	Kilander and Rasmuson, 2005
Pitched Blade Turbine, (30)	1,074	<sup>4</sup> Reynolds average subgrid scale	Unadkat <i>et al.</i> , 2009

\* The equations used to estimate the turbulent energy dissipation rate are:

$$\begin{aligned}
 {}^1 \varepsilon &= A \frac{u'^3}{l} ; & {}^2 \varepsilon &= 15 \overline{v u'_{r,r}{}^2} \\
 {}^3 \varepsilon &= \nu \left\{ 2 \overline{\left( \frac{\partial u_r}{\partial r} \right)^2} + 2 \overline{\left( \frac{\partial u_z}{\partial z} \right)^2} + 3 \overline{\left( \frac{\partial u_r}{\partial z} \right)^2} + 3 \overline{\left( \frac{\partial u_z}{\partial r} \right)^2} + 2 \frac{\partial u_r}{\partial z} \frac{\partial u_z}{\partial r} \right\} \\
 {}^4 \varepsilon &= -2 \tau_{ij} \bar{S}_{ij} & {}^5 \varepsilon &= -\tau_{ij} \bar{S}_{ij}
 \end{aligned}$$

### 4.2.3 Mechanism to describe the elements size reduction

Zhou and Kresta (1998a) suggested that drops are broken when they gain enough energy to compensate the increment of the total surface area. Andersson and Andersson (2006) modeled the fragmentations process of single drops or bubbles injected into a turbulent flow developed in a straight pipe. For the case of stirred tank, a mechanism to describe the breakage of the elements in the dispersion is proposed here.

According to the information presented until now, air bubbles, oil drops or fungus pellets are fragmented in a similar manner. The mechanism proposed to explain this process consists of four steps (as shown in Fig. 4.8). In step 1, a large object enters the high shear zone. Then, this object experiences stretching as a consequence of the shear forces (step 2,); such forces produce the instability and deformation of drops or bubbles whilst in the case of the fungus pellets, the fungal tensile strength is drained. Rupture is the third step. The cycle ends when smaller objects are dispersed in the liquid bulk (fourth step). Objects moving outside the turbulent zone are neither disrupted nor stretched. The cycle is repeated many times until the force equilibrium is reached; for instance, when the inertial forces are not enough to destabilize the surface forces in the case of the bubbles and droplets or the tensile strength in the case of the fungus pellets. To produce further reduction the spectral energy must be amplified and higher turbulence should be produced.

At the beginning of the process, breakage occurs more often because big objects are more unstable than the smaller ones. It is unlikely that all objects reach a uniform size. For the case of oil droplets there is a debate about its size distribution. Some authors have predicted the minimum size considering the theory of Kolmogorov (Liu and Li, 1999), but others have discarded this prediction (Zhou and Kresta, 1998b; Cristini *et al.*, 2003). There are many relationships suggested to predict the biggest drop or the mean size, especially for several silicon oils or petroleum products (Calabrese *et al.*, 1986b; Wang and Calabrese, 1986; Zhou and Kresta, 1998a) but not for oils used in biochemical processes, such as the Castor oil.

Among other factors to consider, the collision of drops or bubbles modifies the object size; however, this phenomenon is particularly important in highly concentrated dispersions (Coulaloglou and Tavlarides, 1976). It is recalled that the use of surfactants (not used in our study)

inhibit coalescence and stabilize the emulsion (Bibette *et al.*, 1992; Pulido-Mayoral and Galindo, 2004).

Finally, it has also been suggested that also mechanical impacts of drops with the baffles or with the tank wall may influence the drop size distribution. However, the occurrence of such events was not observed with enough frequency to be considered as a relevant factor. In agreement with the work of Cristini *et al.* (2003), it is believed that objects fragmentation is caused mainly by the shear forces generated in the impeller discharge region.

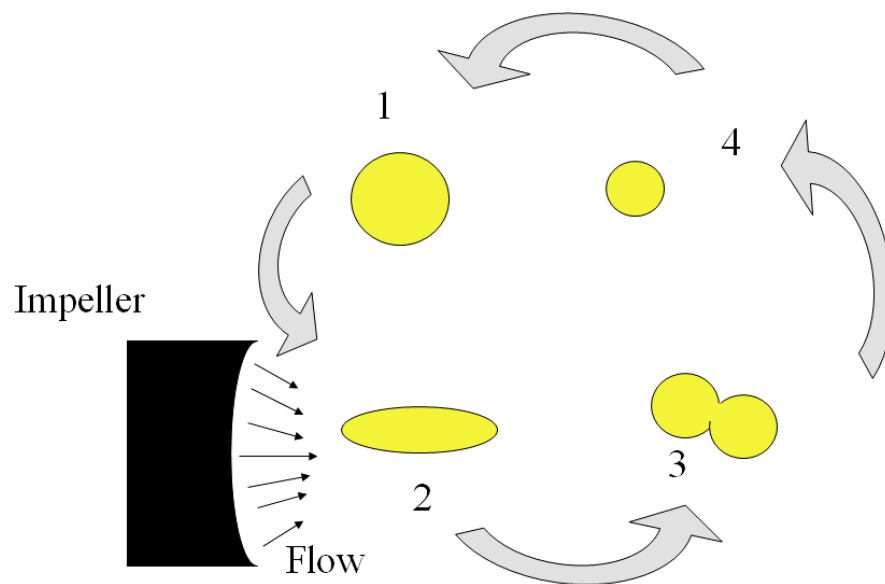


**Figure 4.7.** Schematic representation of the process of object size reduction (1) A large object enters the high shear region. (2) The large object deforms and elongates. (3) The large object fragments. (4) Two objects of smaller size are produced.



CHAPTER 5

*Drops  
flow  
pattern*

The studied zone in the last two chapters was the area occupied by a half vertical plane of the whole system (approximately  $60 \text{ cm}^2$ ). A smaller area of about  $4 \text{ cm}^2$  located in the vicinity of the tank wall will be analyzed in the present chapter. The flow in this zone has not been studied in a detailed manner, not even for a dispersed phase. Discussion focuses on the average vector field obtained from the oil drops light reflectance (no fluorescent tracers were needed) monitored in two normal planes: the first one oriented in a tangential direction (“parallel” to the tank wall) and the other one oriented in the radial direction. Oil droplets were photographed with a high-speed camera to determine the mean diameter and the instantaneous velocity of individual droplets.

## 5.1 Oil droplet dynamics

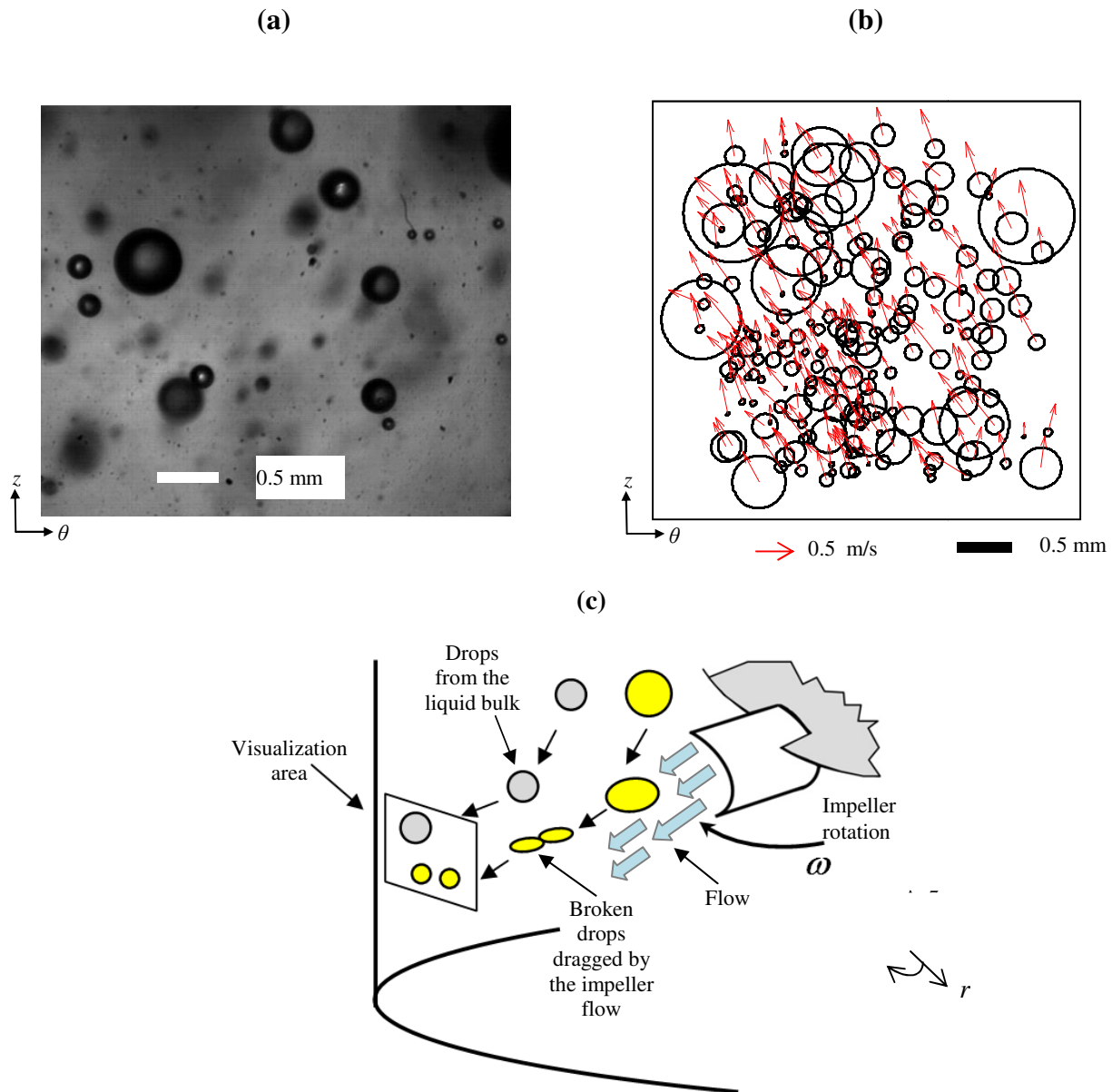
### 5.1.1 Oil droplets velocity comparison

Fig. 5.1a is an example of the drops photographed at 5,000 fps. Although few droplets appear in this image, the history of the total droplets crossing this area during 0.4 s is shown in Fig 5.1b. This map was constructed by drawing one circle for each droplet being the position of each circle represents the local site where each droplet crossed the surface; for example, the diameter of the same droplet was compared in two consecutive photographs ( $\Delta t = 0.2 \text{ ms}$ ), if the difference is larger than 5% the measurement is neglected. Circle saturation suggests the level of homogenization produced by the system; the map presented in Fig 5.1b corresponds to a blending time of 0.4 s, it can be observed that it is not completely covered.

The vectors located in the center of each circle (Fig 5.1b) represent the instantaneous velocity vector ( $\boldsymbol{v}$ ) for each drop displacement in the interval  $\Delta t = 0.2 \text{ ms}$ . This diagram explains the randomness of droplet displacements and the heterogeneity of the velocity vectors (direction and magnitude) in the neighborhood of the tank wall. However, the velocity vectors have a tendency towards the same direction; which will be discussed again in section 5.1.2.

What should call our attention is that larger droplets are preferentially placed in the top-left of the map. An explanation of this behavior is that the smaller drops (appearing in the bottom of the surface) might be the broken drops, dragged directly from the impeller blades and large droplets

might become from a different region (as suggested in Fig. 5.1c). This picture reinforces the explanation proposed to describe the elements size reduction given in section 4.2.3.



**Figure 5.1.** (a) A typical image of the sequence obtained on-line for the study of the oil-water dispersion in a stirred tank; (b) Map to compare the drops size and the instantaneous velocities for each drop crossing the zone in 0.4 s; (c) Scheme to explain the droplet distribution visualized in the map. Symbols:  $z$  for the axial coordinate,  $r$  for the radial coordinate,  $\omega$  for the angular coordinate and  $\theta$  for the tangential orientation.

A number of works dealing with homogenization in stirred vessels by using other kind of maps have been reported in the literature. Zalc *et al.*, (2002) reported a *Poincaré* section obtained from

fluorescent visualizations to provide information about the chaotic and nonchaotic regions of the flow at  $Re < 200$ . From a CFD model, Sanjuan-Galindo *et al.* (2011) presented the *Poincaré* maps corresponding to massless tracers at  $Re < 100$  in a large scale mixing tank. In these works, they were concerned only with the single phase fluid mixing and not with a dispersed phase, not even with the instantaneous velocity. Moreover, less attention has been paid to flows developed in turbulent regimes and the concept has not been applied for oil-water dispersions.

The drop size distribution from a perspective for the whole system has been compared in section 4.1.3. However, one disadvantage for this perspective is that the smallest droplets cannot be properly measured due to the low image resolution. The use of 11× magnification lens made possible to identify droplets smaller than 0.03 mm in a smaller area. The resulting PDF (Fig. 5.2a) is represented with a continuous blue line and compared with the green pointed line representing the old measurement, as shown in Fig 4.3b. An advantage gained with the 11× magnification is that the number of small droplets increases considerably, which increases the accuracy of the interfacial surface estimation. Considering both data groups, the arithmetic diameter is  $d_{av} = 0.62$  mm and the Sauter diameter is  $d_{32} = 0.94$  mm. According to Eq. 2.9, for an oil content of 1% v/v, the interfacial surface between the oil phase and the water is  $a_{oil-H_2O} = 64 \text{ m}^{-1}$ .

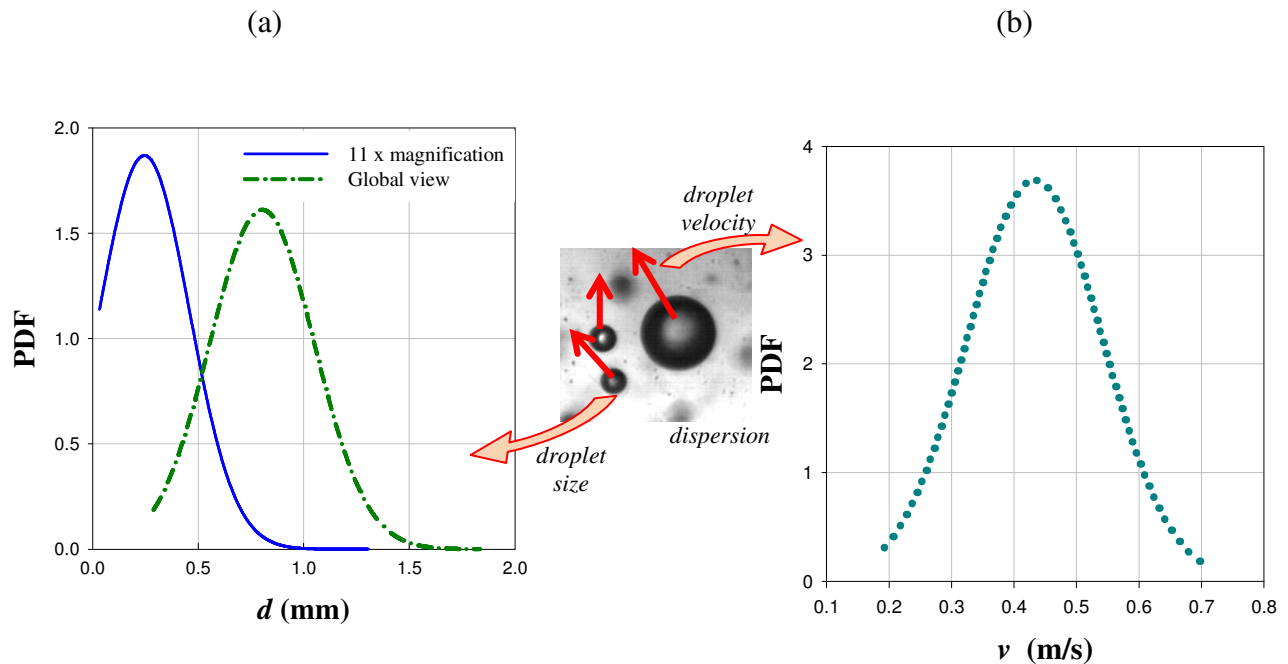


**Figure 5.2.** Probability density function (PDF) versus the (a) drop diameter and (b) instantaneous velocities for individual oil droplets. Measurements were made in a local region at  $Re = 24,500$ .

The drop size distribution is not enough to explain the convective mass transfer process in turbulent conditions; indeed, it is a complex process where the surface renewal is implied, promoted by turbulent eddy diffusion and the relative drops velocity. The instantaneous velocity distribution of individual droplets is plotted in Fig. 5.2b. The PDF exhibits a Gaussian distribution, where velocity ranges between  $0.2 \text{ m s}^{-1}$  to  $0.7 \text{ m s}^{-1}$ , the average value of the instantaneous measurements is  $v_{av} = 0.42 \text{ m s}^{-1}$ . A similar distribution was reported by Zamankhan (2010) for the velocity of gas bubbles moving in water in a stirred tank.

The instantaneous random movement of individual droplets has been previously discussed elsewhere (Guevara *et al.*, 2008). In such work, they reported the chaotic movement of oil droplets in a continuous phase with two different rheological properties: a constant viscosity continuous phase and a shear-thinning fluid ( $n = 0.77$ ,  $k = 0.11 \text{ Pas}^n$ ). The trajectory developed in the two cases is compared in Fig. 5.3, in which both images were obtained through a running-average routine overlapping the object trajectories. Objects transported in a Newtonian phase (Fig. 5.3a) corresponds to 30 images taken at 5,130 frames/s in an agitated system in the turbulent regime ( $Re = 16,800$ ). The dark channels correspond to the trajectories of the dispersed objects in the plane ( $\theta$ ,  $z$ ), i.e. tangential and axial references. As seen, objects exhibit an instantaneous chaotic movement with random directions and velocities in the turbulent regime.

Figure 5.3b shows the oil droplets transported in an aqueous solution containing 0.6 % of Carboxymethylcellulose (CMC) in the transition regime ( $Re = 582$ ). The running-average of 20 images taken at 800 frames/s was overlapped with the droplet position in a short interval (1.2 ms). The oil droplets are displaced homogeneously in a parallel way oriented with a slope of 22 degrees from the vertical reference in counterclockwise. Although movement is mainly unidirectional, oil droplets move at different speeds depending on the deepness of the plane. The droplet displacement is represented with the arrows. The arrow width represents the object diameter and the arrow length is related to the object speed. The well-focused objects, located in the foreground, are represented with the continuous arrows (short arrows), and the trajectories of those non-focused objects, located in the background, are presented with discontinuous lines (larger arrows). Differences in the arrow length means that objects are transported in different planes. The droplets in the background move at higher velocities (0.06 m/s), while the droplets in the foreground move at lower velocities (0.026 m/s). It is believed that viscosity effects are mainly responsible for the velocity gradient. The shear rate is smaller over the wall and increases in the zones closer to the

impeller. In general, the velocity magnitudes for the droplets moving in the non-Newtonian phase were smaller respect to the velocity of drops moving in the Newtonian phase.

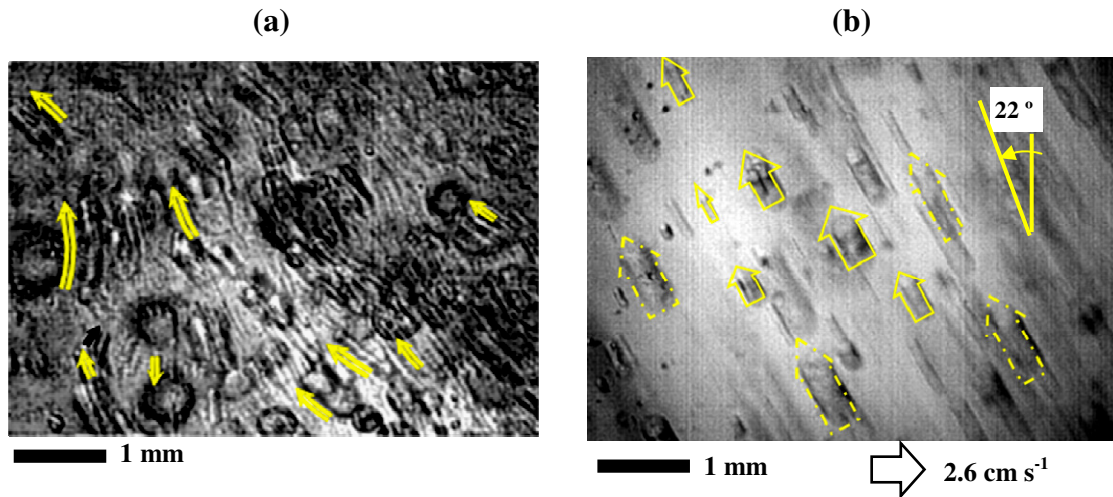


**Figure 5.3.** Overlapped images captured in dispersions agitated in different regimens: (a) Constant viscosity continuous phase. (b) Non-Newtonian dispersion (CMC solution).

### 5.1.2. Oil phase velocity

The instantaneous velocity of individual drops captured with a high-speed camera was analyzed in the previous section. The average velocity obtained with PIV measurements following the light reflected by the oil phase in a local region is now presented. The average oil-phase velocity was obtained in two normal vertical planes, for instance, a radial oriented plane  $rz$  and a tangential plane defined by  $\theta z$ .

Two map contours showing the velocity magnitude and the vector field are shown in Fig 5.4a. In the plane  $z\theta$  (Fig. 5.4a) three zones can be identified: (a) in the lower part (light blue shades), the velocity component has low magnitudes, i.e.  $v_{z\theta} \approx 0.15 \text{ m s}^{-1}$ , (b) in the central zone a slight increment is noticed,  $v_{z\theta} \approx 0.20 \text{ m s}^{-1}$  (light green shades), and (c) in the upper zone the velocity reaches its maximum value,  $v_{z\theta} > 0.25 \text{ m/s}$  (dark green shades). The small spots (gray shades) correspond to oil drops adhered to the tank wall, which do not have a dynamic mean (the area of each spots is less than  $1 \text{ mm}^2$ ). The streamlines of the flow structure in the plane  $\theta z$  are shown in

Fig. 5.4b. They are parallel with an inclination of  $22^\circ$  counterclockwise from the vertical. The same behavior was observed for oil drops moving in a low viscous phase with non-Newtonian rheology in the transitory regime showed in Fig. 5.3b, what suggests that the Scaba impeller produces in this region very similar streamlines for a wide range of flow regimes (for instance,  $580 < Re < 24,000$ ).

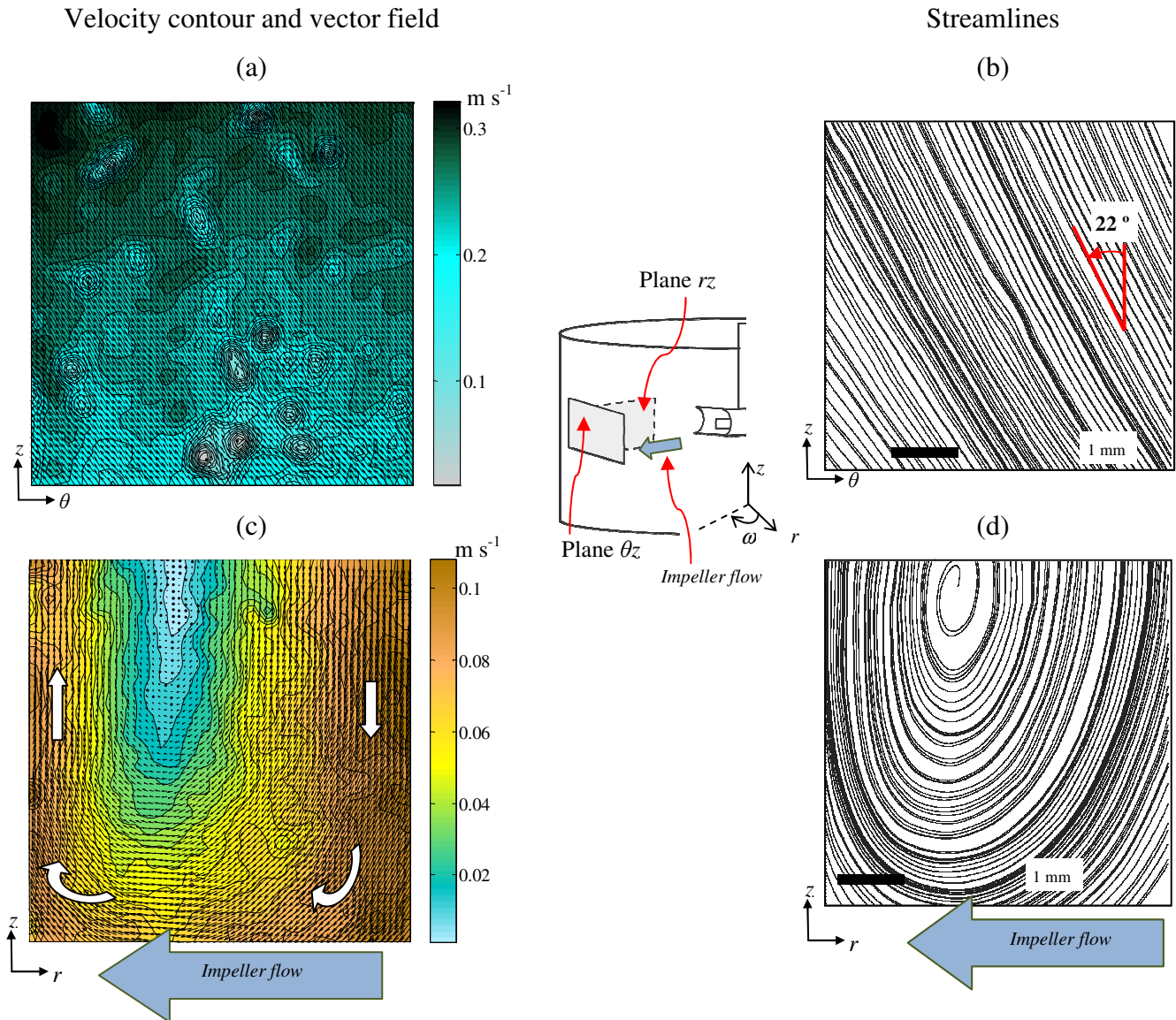


**Figura 5.4.** Contour maps for the velocity magnitude and vector field for the oil phase in the planes: (a)  $\theta z$  and (c)  $rz$ . Streamlines for the oil phase velocity in the plane: (b)  $z\theta$  and (d)  $rz$ .

The velocity field in the plane  $rz$  (Fig. 5.4c) follows a U-shape; in the right side, the flow descends, whilst in left side the flow ascends. Velocity magnitudes are distributed as follows: (a) In the

centre of the surface (light blue shades), the velocity flow is low ( $v_{rz} < 0.03$  m/s), which suggests oil segregation and poor mixing; (b) a transitional zone (green and yellow shades) is observed with larger velocities ( $0.04$  m/s  $< v_{rz} < 0.06$  m/s); (c) The two vertical extreme sides of the surface (pink and light brown shades) develop the largest velocities ( $0.065$  m/s  $< v_{rz} < 0.11$  m/s). Fig. 5.4d shows the streamlines for the plane  $\theta z$ , in which it is noticed again the U-shape described by the velocity magnitudes.

### 5.1.3. Isotropy and energy dissipation rate in the tank wall region

Velocity fluctuates quite uniformly in the planes  $\theta z$  and  $rz$  (Fig. 5.5a), i.e.  $v'_{\theta z} \approx 0.10$  m s<sup>-1</sup> and  $0.06$  m s<sup>-1</sup>  $< v'_{\theta z} < 0.08$  m s<sup>-1</sup>. Low fluctuations support the structured flow presented by the streamlines of Fig 5.4 b and d. The flow structure suggests good transport, while low fluctuations suggest poor mixing.

To evaluate the influence of the local flow in the elements in the dispersion, it is useful to analyze the turbulent properties. It is well known that isotropy is the simplest case of turbulent flow; for instance, it implies spatial homogeneity independently of the direction. In other words, it is valid the product  $v'_i v'_j \approx 0$  for  $i$  or  $j = r, \theta, z$ , if  $i \neq j$ . In the neighborhood of the tank wall, defined by the normal planes  $\theta z$  and  $rz$ , it was found that flow approaches to isotropy ( $v'_r v'_z \rightarrow 0$  as well as  $v'_\theta v'_z \rightarrow 0$ ); what suggest that elements are neither deformed nor perturbed. The contour map showing the turbulent energy dissipation rate for the planes  $\theta z$  and  $rz$  is presented in Fig. 5.5b. Although certain variations are appreciated, the turbulent energy dissipation rate for the  $\theta z$  and  $rz$  planes are approximated equivalent; i.e.  $0.1$  m<sup>2</sup> s<sup>3</sup>  $< \varepsilon_{\theta z} < 0.6$  m<sup>2</sup> s<sup>3</sup> and  $0.1$  m<sup>2</sup> s<sup>3</sup>  $< \varepsilon_{rz} < 0.5$  m<sup>2</sup> s<sup>3</sup>, respectively. These values are considerably reduced respect the values obtained in the region close to the impeller ( $\varepsilon \approx 18$  m<sup>2</sup> s<sup>3</sup>) and approximate the mean dissipation rate ( $0.00046$  m<sup>2</sup> s<sup>-3</sup>). It is inferred that the energy dissipation rate in this zone has little influence on the processes like the collisions rate, mass transfer, cellular activity, cell damage and mass transfer.

According to Eq. 1.3, the resulting Kolmogorov scale is  $\lambda \approx 4 \times 10^{-2}$  mm in the neighborhood of the tank wall. The value of this scale is more than 3 times larger than the micro-scale determined previously in the region of the impeller discharge (i.e.  $\lambda \approx 1.5 \times 10^{-2}$  mm), such difference makes



that the smallest turbulent eddy is larger than the size of many objects and as a consequence, the turbulent viscous regime prevails.

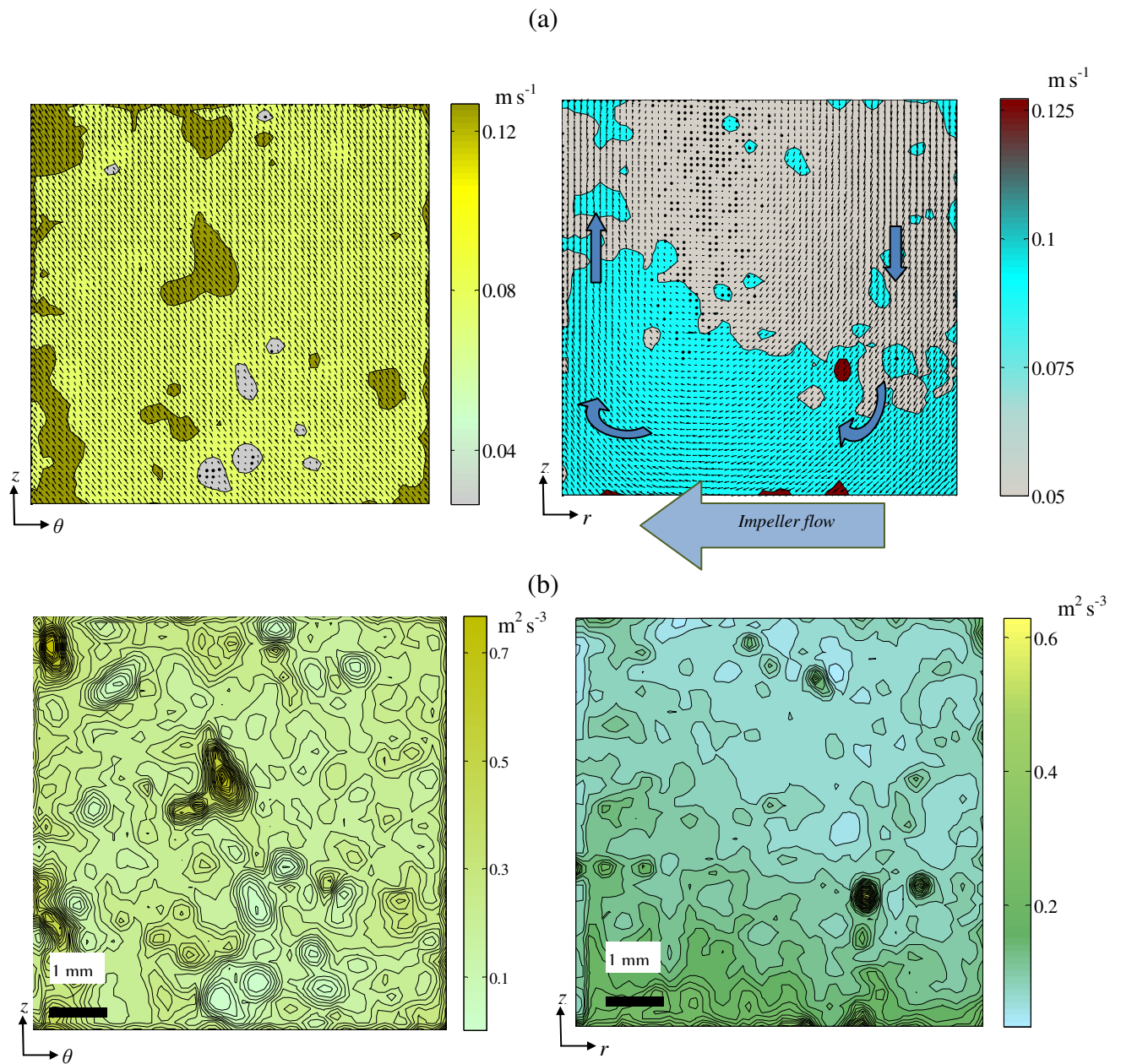


**Figure 5.5.** (a) Contour map for the velocity fluctuation ( $v'_{oil}$ ) and vector field for the oil phase. (b) Turbulence energy rate dissipation ( $\epsilon_{oil}$ ) experienced by the oil phase.

*C o n c l u s i o n s*  
*a n d*  
*F u t u r e*  
*w o r k*

The hydrodynamics generated by a Scaba impeller in a flat-bottom cylindrical tank was discussed in order to find out the effects in the dispersed components. Castor oil -as an immiscible liquid-, an air stream –as a gaseous phase-, and fungus pellets –as a solid phase- were dispersed (one per time) in aqueous phase. Such components are common substrates in liquid fermentations.

Two stages were identified in the dispersion process of any of these components. The first stage has a short duration and consists of pumping the dispersed phase; for instance, the solid phase must be pumped upwards from the bottom and suspended, the low-density liquid-phase must be pumped downwards from the top and submerged, and the gas-phase must be retained and increase the hold-up. Fragmentation is the second stage identified in the dispersion process, promoted by the turbulent flow properties. The axial pumping produced by Scaba impeller promotes well the dispersion and the size reduction of the phases in dispersion, which suggests the use of this agitator to improve many other industrial processes.

The viscous liquid phase, initially suspended in the free surface of the liquid phase, is dragged into liquid bulk and elongated, as a result of the stretched flow. This is the earliest step of the dispersion process between two immiscible liquids and is performed by the dragging of the viscous phase in a helical way around the impeller axis until the impeller flat-disk. Then, filamentous-like viscous structures are produced and expelled from the impeller blades into the liquid bulk. Such filaments have an amorphous and unstable shape and they are easily elongated and perturbed by the flow properties. The impeller flow periodicity, the high levels of the velocity fluctuation, the vortex field and the turbulent energy dissipation rate among others, participate in the filament rupture. Details of these variables were compared in two perspectives: initially, from a global point of view to understand the hydrodynamics in the whole system, and from a local region placed near the tank wall at small scale.

The flow pattern obtained by the Scaba impeller is in agreement with other studies previously reported for radial impellers; two large eddies symmetrically distributed in the upper and the lower zone of the impeller were observed. However, special attention should be paid to the flow in the impeller discharge. This zone holds the largest velocity fluctuations in the tank and contains the major turbulent energy dissipation rate. Moreover, in the core of the impeller blades, the velocity vectors are concentrated in the impeller centerline. Such effect is produced by the curvature of the impeller blades (remember that the blades of the Rushton turbine are flat) but this has not received

enough consideration. The importance of this phenomenon is the turbulence promoted in the zone, reflected in the fluid elements elongation and reshaping.

Another characteristic of this zone is the formation of two vortices of the same size and opposite rotation, separated by the radial centerline of the impeller blades axis. This flow behavior deforms and elongates the amorphous filaments expelled by the impeller blades and the core of each vortex (low pressure zones) tense the elements.

The purpose of making dispersions is the improvement of the mass transfer process, which is enhanced by promoting the size reduction of the elements in the dispersion. The mechanism to explain the fragmentation process has been proposed considering the turbulent flow properties, in accordance to the high-speed video registers and comparing the object size reduction. This mechanism assumes that large objects are perturbed and reshaped exclusively in the zone of the impeller discharge; if inertial forces overcome the superficial forces the fragmentation takes place. Only those elements receiving enough energy to increase the surface are fragmented. The maximum turbulent energy dissipation rate is located in the impeller flow discharge. This fact suggests that mixing and mass transfer in the micro scale occurs mainly in the impeller flow discharge; in the rest of the tank, isotropy is more evident.

In the rest of the liquid bulk, far away from the impeller discharge, both drops and bubbles recoil and adopt spheroidal shapes due to the predominance of the superficial forces, the small velocity fluctuations and the lost of energy in the fluid. It was shown that the size reduction process depends on the stirring time and is limited by the equilibrium among inertial, viscous and interfacial forces. Although fragmentation is more frequent in the beginning of the stirring, the object size tends to achieve the steady state after certain time.

The gas phase distribution has been evaluated from visual registers and analyzed quantitatively with the dimensionless Froude number. Gas flooding was avoided, but the gas phase was poorly distributed; i.e. the air bubbles occupy mainly the upper part of the tank and higher power inputs are needed to improve the gas phase dispersion below the impeller. In contrast, the oil phase is better distributed, i.e. the oil drops occupy the entire system. In order increase accuracy in obtaining the drop size distribution, drops were measured from two perspectives: a global view of

the system and a small zone captured with a magnification lens in the neighborhood of the tank wall.

It was learned that the castor oil disruption is faster than the gas phase fragmentation or the fresh biomass breakup when they are exposed to the same flow pattern; for instance, the average oil drops diameter is smaller than the average gas bubbles diameter. One reason is that the interfacial tension between the oil-phase and the water-phase is smaller than the corresponding one between the air-phase and the water-phase.

Previous reports have demonstrated that live cells have certain resistance to the hydrodynamic stress; however, the sensitivity of the cells aggregates –like the fungus pellets or multi-cellular microorganisms-, and the effects of the shear stress have received less attention. It was showed that inertial forces overcome the fungal tensile strength and limit the size of the fungus pellets in the absence of other components that could modify the rheological properties.

The small region that was studied in the neighborhood of the tank wall revealed interesting points. The instantaneous velocity of the individual objects, like the oil drops, was documented as a factor involved in the surface renewal, one condition in the turbulent mass transfer process. The flow pattern observed in the plane  $\theta z$  remained unchanged when the rheological properties were varied, which suggests flow regime independence. This fact could be explained on the basis of the low energy that prevails in the zone, which suggests that energy could be spent mainly in the transport of the elements rather than in the mass transfer process.

The specific area that is available for the mass transfer process was estimated for both the oil-water interface and the gas-water interface. Such property had been estimated in the past, but rarely was related with the velocity field that prevails in the system. The influence of the vortices, velocity fluctuations and the dissipation rate has not been discussed. This scheme opens the possibility to investigate other regimes as well as the application of the photographic technique to measure *in situ* the object size or the individual velocities. It is also suggested to explore the filaments production formed with an oil phase that exhibits different rheological properties.

# *Bibliography*

- Abu-Reesh I., Kargi F. 1989. Biological responses of hybridoma cells to define hydrodynamic shear stress. *J. Biotechnol.* 9: 167-178
- Alcamo R., Micale G., Grisafi F., Brucato A., Ciofalo M. 2005. Large-eddy simulation of turbulent flow in an unbaffled stirred tank driven by a Rushton turbine. *Chem. Eng. Sci.* 2303-2316
- Alves S. S., Maia C. I., Vasconcelos J. M. T. 2004. Gas-liquid mass transfer coefficient in stirred tanks interpreted through bubble contamination kinetics. *Chem. Eng. Proc.* 43: 823-830
- Andersson, R., Andersson, B. 2006. On the breakup of fluid particles in turbulent flows. *AIChE J.* 52, 2020-2030.
- Armenante P. M., Huang T. Y. 1992. Experimental determination of the minimum agitation speed for complete liquid-liquid dispersion in mechanically agitated vessels. *Ind. Eng. Chem. Res.* 31: 1398-1406
- Ascanio G., Castro B., Galindo E. 2004. Measurement of power consumption in stirred vessels- a review. *Chem. Eng. Res. Des.* 82(A9): 1282-1290
- Aubin J., Le Sauze N., Bertrand J., Fletcher D. F., Xuereb C. 2004. PIV measurements of flow in an aereated tank stirred by a down- and an up-pumping axial flow impeller. *Exp. Thermal Fluid Sci.* 28: 447-456
- Auton T. R., 1987. The lift force on a spherical body in a rotational flow. *J. Fluid Mechanics.* 183: 199-
- Baldi S., Yianneskis M. 2003. On the direct measurement of turbulence energy dissipation in stirred vessels with PIV. *Ind. Eng. Chem. Res.* 42: 7006-7016
- Baldi S., Yianneskis M. 2004. On the quantification of energy dissipation in the impeller stream of a stirred vessel from fluctuating velocity gradient measurements. *Chem. Eng. Sci.* 59: 2659-2671
- Bao Y., Hao Z., Gao Z., Shi L., Smith J. M. 2005. Suspension of buoyant particles in a three phase stirred tank. *Chem. Eng. Sci.* 60: 2283-2292
- Basmadjian D. 2004. Mass transfer, principles and applications. CRC Press. USA.
- Benchapattarapong N., Anderson W. A., Bai F., Moo-Young M. 2005. Reology and hydrodynamic properties of *Tolypocladium inflatum* fermentation broth and its simulations. *Bioprocess Biosyst. Eng.* 27: 239-247
- Bhattacharya S., Hebert D., Kresta S. M. 2007. Air entrainment in baffled stirred tanks. *Chem. Eng. Res. Des.* 85 (A5): 654-664

- Bibette J., Morse D. C., Witten T. A., Weitz D. A. 1992. Stability criteria for emulsions. *Phys. Rev. Lett.* 69: 2439-2442
- Bouaifi M., Hebrard G., Bastoul D., Roustan M. 2001. A comparative study of gas hold-up, bubble size, interfacial area and mass transfer coefficients in stirred gas-liquid reactors and bubble columns. *Chem. Eng. Proc.* 40: 97-111
- Calabrese, R.V., Chang T.P.K., Dang P.T. 1986a. Drop breakup in turbulent stirred-tank contactors. Part I: Effect of dispersed-phase viscosity. *AIChE J.* 32, 657-666
- Calabrese R.V., Chang T. P. K., Dang P. T. 1986b. Drop breakup in turbulent stirred-tank contactors. Part II: Effect of dispersed-phase viscosity. *AIChE J.* 32, 657-666
- Campolo M., Sbrizzai F., Soldati A. 2003. Time-dependent flow structures and Lagrangian mixing in Rushton-impeller baffled-tank reactor. *Chem. Eng. Sci.* 58: 1615 – 1629
- Chatzi E. G., Boutris C. J. Kiparissides C. 1991. On-line monitoring of drop size distribution in agitated vessels. 1. Effects of temperature and impeller speed. *Ind. Eng. Chem. Res.* 30: 536-543
- Chin C-C., Yiaccoumi S., Tsouris C. 1998. Shear-induced flocculation of colloidal particles in stirred tanks. *J. Colloid Interface Sci.* 206: 532-545
- Clarke K. G. Correia L. D. C. 2008. Oxygen transfer in hydrocarbon–aqueous dispersions and its applicability to alkane bioprocesses: a review. *Biochem. Eng. J.* 39: 405-429
- Cooke M., Heggs P. J. 2005. Advantages of the hollow (concave) turbine for multi-phase agitation under intense operating conditions. *Chem. Eng. Sci.* 60: 5529-5543
- Coulaloglou C. A., Tavlarides L. L. 1976. Drop size distributions and coalescence frequencies of liquid-liquid dispersions in flow vessels. *AIChE J.* 22: 289-297.
- Cristini V., Blawdziewicz J., Loewenberg M., Collins L. R. 2003. Breakup in stochastic Stokes flows: sub-Kolmogorov drops in isotropic turbulence. *J. Fluid Mech.* 492: 231–250
- Demain A. L. 2000. Small bugs, big business: the economic power of the microbe. *Biotech. Advances.* 18: 499-514
- Ducci A., Yianneskis M. 2005. Direct determination of energy dissipation in stirred vessels with two-point LDA. *AIChE J.* 51: 2133-2149
- Duclaux V., Clanet C., Quéré D. 2006. The effects of gravity on the capillary instability in tubes. *J. Fluid Mech.* 556: 217–226
- Dumont E., Delmas H. 2003. Mass transfer enhancement of gas absorption in oil-in-water systems: a review. *Chem Eng. Proc.* 42: 419-438



- Eggers, J., Villermaux, E. 2008. Physics of liquid jets. *Rep. Prog. Phys.* 71, 036601
- Fisher L. R., Mitchell E. E. Parker N. S. 1985. Interfacial tensions of commercial vegetable oils with water. *J. Food Sci.* 50: 1201-1202
- Fradette L., Tanguy P. A., Bertrand F., Thibault F., Ritz J. B., Giraud E. 2007. CFD phenomenological model of solid-liquid mixing in stirred vessels. *Computers Chem. Eng.* 31: 334-345
- Freund J., Moin P., Lele S. 2011. Supersonic sound free-shear flows. *Gallery of turbulent flows*. In: Center for turbulence research. <http://www.stanford.edu/group/ctr/gallery.html> (Last visit: June 2011)
- Galindo E., Pacek A. W., Nienow A. W. 2000. Study of drop and bubble sizes in a simulated mycelia fermentation broth of up to four phases. *Biotechnol. Bioeng.* 69: 213-221
- Galindo E., Larralde-Corona C. P., Brito T., Córdova-Aguilar M. S., Taboada B., Vega-Alvarado L., Corkidi G., 2005. Development of advanced image analysis techniques for the *in situ* characterization of multiphase dispersions occurring in bioreactors. *J. Biotechnol.* 116: 261-270
- Gimbun J., Rielly C. D., Nagy Z. K. 2009. Modelling of mass transfer in gas-liquid stirred tanks agitated by Rushton turbine and CD-6 impeller: A scale-up study. *Chem. Eng. Res. Des.* 437-451
- Guevara-López E., Sanjuan-Galindo R., Córdova-Aguilar M. C., Corkidi G., Ascanio G., Galindo E. 2008. High-speed visualization of multiphase dispersions in a mixing tank. *Chem. Eng. Res. Des.* 86: 1382-1387
- Hagedorn J. G., Martys N. S. Douglas J. F. 2004. Breakup of a fluid thread in a confined geometry: droplet-plug transition, perturbation sensitivity, and kinetic stabilization with confinement. *Phys. Rev. E* 69 056312
- Hartmann H., Derksen J. J. van den Akker H. E. A. 2004. Macroinstability uncovered in a Rushton turbine stirred tank by means of LES. *AIChE J.* 50: 2383-2393
- Hinze, J. O. 1955. Fundamentals of the hydrodynamic mechanism of splitting in dispersion processes. *AIChE J.* 1 : 289-295
- Iranshahi A., Devals C., Heniche M., Fradette L., Tanguy P. A., Takenaka K. 2007. Hydrodynamics characterization of the Maxblend impeller. *Chem. Eng. Sci.* 62: 3641-3653.
- Jahoda M., Tomáková M., Moštek M., 2009. CFD prediction of liquid homogenization in a gas-liquid stirred tank. *Chem. Eng. Res. Des.* 87: 460-467

- Kerdouss F., Bannari A., Proulx P. 2006. CFD modeling of gas dispersion and bubble size in a double turbine stirred tank. *Chem. Eng. Sci.* 61: 3313-3322.
- Khan F. R., Rielly C. D., Brown D. A. R. 2006. Angle-resolved stereo-PIV measurements close to a down-pumping pitched-blade turbine. *Chem. Eng. Sci.* 61: 2799-2806.
- Khopkar A., Aubin J., Rubio-Atoche C., Xuereb C., Le Sauze N., Bertrand J., Ranade V. V. 2004. Flow generated by radial flow impellers: PIV measurements and CFD simulations. *Internal. J. Chem. Reactor Eng.* 2: A18
- Khopkar A. R., Rammohan A. R., Ranade V. V. Dudukovic M. P. 2005. Gas-liquid flow generated by a Rushton turbine in stirred vessel: CARPT/CT measurements and CFD simulations. *Chem. Eng. Sci.* 60: 2215-2229
- Khopkar A. R., Kasat G. R., Pandit A. B., Ranade V. V. 2006. CFD simulation of mixing in tall gas-liquid stirred vessel: role of local flow patterns. *Chem. Eng. Sci.* 61: 2921-2929
- Kovács T., Trägårdh C., Fuchs L. 2001. Flow and turbulence in the discharge of radial pumping turbines: influence of the turbine type. *Chem Eng. Technol.* 24: 1035-1044.
- Kumar S., Gonzalez B., Probst O. 2011. Flow past two rotating cylinders. *Phys. Fluids.* 23 : 014102
- Laakkonen M., Moilanen P., Alopaeus V., Aittamaa J. 2007. Modeling local gas-liquid mass transfer in agitated vessels. *Chem. Eng. Res. Des.* 85: 665-675
- Lane G. L., Shwarz M. P., Evans G. M., 2002. Predicting gas-liquid flow in a mechanically stirred tank. *Applied Math. Modelling.* 26 : 223-235
- Laurenzi F., Coroneo M., Montante G., Paglianti A., Magelli F. 2009. Experimental and computational analysis of immiscible liquid-liquid dispersions in stirred vessels. *Chem. Eng. Res. Des.* 87: 507-514
- Liao W., Liu Y., Frear C., Chen S. 2007. A new approach of pellet formation of a filamentous fungus – *Rhizopus oryzae*. *Bioresource Technol.* 98: 3415-3423
- Li M., White G., Wilkinson D., Roberts K. J. 2005. Scale up study of retreat curve impeller stirred tanks using LDA measurements and CFD simulation. *Chem. Eng. J.* 108: 31-90
- Li Z. J., Shukla V., Wenger K., Fordyce A., Pedersen A. G., Marten M. 2002. Estimation of hyphal tensile strength in production-scale *Aspergillus oryzae* fungal fermentations. *Biotechnol Bioeng.* 77:601-613.
- Liu S., Li D. 1999. Drop coalescence in turbulent dispersions. *Chem. Eng. Sci.* 54: 5667-5675

- Lovick J., Mouza A. A., Paras S. V. Lye G. J., Angeli P. 2005. Drop size distribution in highly concentrated liquid-liquid dispersions using a light back scattering method. *J. Chem. Technol. Biotechnol.* 80: 545-552
- Lucatero S., Larralde-Corona C. P., Corkidi G., Galindo E. 2003. Oil and air dispersion in a simulated fermentation broth as a function of mycelial morphology. *Biotechnol. Prog.* 19: 285-292
- Maaß S., Wollny S., Sperling R., Kraume M. 2009. Numerical and experimental analysis of particle strain and breakage in turbulent dispersions. *Chem. Eng. Res. Des.* 87: 565-572
- Maranga L., Cunha A., Clemente J., Cruz P., Carrondo M. J. T. 2004. Scale-up of virus-like particles production: effects of sparging, agitation and bioreactor scale on cell growth, infection kinetics and productivity. *J. Biotechnol.* 107: 55-64
- Martín M. Montes F. J. Galán M. A. 2008. Bubbling process in stirred tank reactors I: Agitator effect on bubble size, formation and rising. *Chem. Eng. Sci.* 63: 3212 - 3222
- Mathieu J., Scott J. 2000. An introduction to turbulent flow. Cambridge University press. USA. P. 51
- Montante G., Moštek M., Jahoda M., Magelli F. 2005. CFD simulations and experimental validation of homogenization curves and mixing time in stirred Newtonian and pseudoplastic liquids. *Chem. Eng. Sci.* 60: 2427-2437
- Montante G., Horn D., Paglianti A. 2008. Gas-liquid flow and bubble size distribution in stirred tanks. *Chem. Eng. Sci.* 63: 2107-2118
- Moštek M., Kukuková A., Jahoda M., Machon V. 2005. CFD Prediction of flow and homogenization in a stirred vessel: part II vessel with three and four impellers. *Chem. Eng. Technol.* 28: 1134-1143
- Murthy B. N., Ghadge R. S., Joshi J. B. 2007. CFD simulation of gas-liquid-solid stirred reactor: Prediction of critical impeller speed for solid suspension. *Chem. Eng. Sci.* 62: 7184-7195
- Nienow A. W. 2004. Break-up, coalescence and catastrophic phase inversion in turbulent contactors. *Advances Colloid Interface Sci.* 108-109: 95-103
- Oh S. K. W., Nienow A. W., Al-Rubeai M., Emery A. N. 1989. The effects of agitation intensity with and without continuous sparging on the growth and antibody production of hybridoma cells. *J. Biotechnol.* 12: 45-62

- Oliveira, M. S. N., McKinley, G.H. 2005. Iterated stretching and multiple beads-on-a-string phenomena in dilute solutions of high extensible flexible polymers. *Phys. Fluids* 17, 071704
- Pacek A. W., Nienow A. W. 1995. A problem for the description of turbulent dispersed liquid-liquid systems. *Int. J. Multiphase Flow*. 21: 323-328
- Pacek A. W., Man C. C., Nienow C. C. 1998. On the Sauter mean diameter and size distributions in turbulent liquid/liquid dispersions in a stirred vessel. *Chem. Eng. Sci.* 53: 2005-2011
- Pakzad L., Ein-Mozaffari F., Chan P. 2008. Using computational fluid dynamics modeling to study the mixing of pseudoplastic fluids with a Scaba 6SRGT impeller. *Chem Eng. Proc.* 47: 2218-2227
- Podgórska W. 2006. Modelling of high viscosity oil drop breakage process in intermittent turbulence. *Chem Eng. Sci.* 61: 2986-2993
- Pulido-Mayoral N., Galindo E. 2004. Phases dispersion and oxygen transfer in a simulated fermentation broth containing Castor oil and proteins. *Biotechnol. Prog.* 20: 1608-1613
- Ramachandran L. M., Tsokos C. P. 2009. *Mathematical statistics with applications*. Academic Press. USA.
- Revstedt J., Fuchs L., Kovács T., Trägårdh C. 2000. Influence of impeller type on the flow structure in a stirred reactor. *AIChE J.* 46: 2373-2382
- Ribe N. M. 2004. Coiling of viscous jets. *Proc. R. Soc. Lond. A.* 460: 3223-3239
- Rivera C., Heniche M., Ascanio G., Tanguy P. 2004. A virtual finite element model for centered and eccentric mixer configurations. *Comp. Chem. Eng.* 28: 2459-2468
- Rivera, C., Heniche, M., Takenaka, K., Tanguy, P. 2009. Finite element modeling of the laminar and transition flow of the Superblend dual shaft coaxial mixer on parallel computers. *Chem. Eng. Sci.* 64: 4442-4456
- Roberts P. J. W., Webster D. R. 2002. Turbulent diffusion. In: *Environmental fluid mechanics: theories and applications*. Shen H. H. Ed. ASCE publications. Ch. 2. Pp 7-45
- Rocha-Valadez J. A., Hassan M., Corkidi G., Flores C., Galindo E., Serrano-Carreón L. 2005. 6-pentyl- $\alpha$ -pyrone production by *Trichoderma harzianum*: the influence of energy dissipation rate and its implications on fungal physiology. *Biotechnol. Bioeng.* 91: 54-61
- Rodríguez Porcel E. M., Casas López J. L., Sánchez Pérez J. A., Fernández Sevilla J. M., Chisti Y. 2005. Effects of pellet morphology on broth rheology in fermentations of *Aspergillus terreus*. *Biochem. Eng. J.* 26: 139-144

- Sahu A. K., Kumar P., Joshi J. B. 1998. Simulation of flow in stirred vessel with axial flow impeller: zonal modeling and optimization of parameters. *Ind. Eng. Chem. Res.* 37: 2116-2130
- Sajjadi S. Zerfa M., Brooks B. W. 2002. Dynamic behaviour of drops in oil/water/oil dispersions. *Chem. Eng. Sci.* 57: 663-675
- Sanjuan-Galindo R. 2006. Producción del nematodo entomopatógeno *Steinernema carpocapsae* en cultivo monoxénico sumergido en biorreactor Air-lift. *Master Sci. Thesis*. Universidad Autónoma del Estado de Hidalgo.
- Sanjuan-Galindo R., Soto E. Ascanio G., Zenit R. 2010. Making emulsions. Image Gallery. American Physics Society, Division of Fluids. <http://arxiv.org/abs/1010.4195v1>  
<http://www.aps.org/units/dfd/pressroom/gallery/zenit10b.cfm>
- Sanjuan-Galindo R., Heniche M., Ascanio G., Tanguy P. A. 2011. CFD investigation of new helical ribbon mixers bottom shapes to improve pumping. *Asia-Pac. J. Chem. Eng.* 6, 181-193
- Sardeing R., Aubin J., Xuereb C. 2004. Gas-liquid mass transfer. A comparison of down- and up pumping axial flow impellers with radial impellers. *Chem Eng. Res. Des.* 82: 1589-1596
- Scargiali F., D'Orazio A., Grisafi F., Brucato A. 2007. Modeling and gas simulation of gas-liquid hydrodynamics in mechanically agitated stirred tanks. *Chem Eng. Res. Des.* 85: 637-646
- Serrano-Carreón L., Flores C., Galindo E. 1997.  $\gamma$ -Decalactone production by *Trichoderma harzianum* in stirred bioreactors. *Biotechnol. Prog.* 14: 205-208
- Sharp W. V., Adrian R. J. 2001. PIV study of small-scale flow structure around a Rushton turbine. *AIChE J.* 47: 766-778
- Sheng J., Meng H., Fox R. O. 2000. A large eddy PIV method for turbulence dissipation rate estimation. *Chem. Eng. Sci.* 55: 4423-4434
- Shinjo, J., Umemura, A. 2010. Simulation of liquid jet primary breakup: dynamics of ligament and droplet formation. *Int. J. Multiphase Flow* 36, 513-532
- Shoot C. M., Calabrese R. V. 1995. Mean velocity field relative to a rushton turbine blade. *AIChE J.* 41: 1-11
- Soto E., Goujon C., Zenit R., Manero O. 2006. A study of velocity discontinuity for single air bubbles rising in an associative polymer. *Phys. Fluids.* 18: 121510

- Taboada B., Vega-Alvarado L., Córdova-Aguilar M. S., Galindo E., Corkidi G. 2006. Semi-automatic image analysis methodology for the segmentation of bubbles and drops in complex dispersions occurring in bioreactors. *Exp. Fluids*. 41:383-392
- Takahashi K., Motoda M. 2009. Chaotic mixing created by object inserted in a vessel agitated by an impeller. *Chem. Eng. Res. Des.* 87: 386-390
- Tinoco R., Acevedo A., Galindo E., Serrano-Carreón L. 2011. *J. Ind. Microbiol Biotechnol.* 38: 531-540
- Tsinober A. 2009. An informal conceptual introduction to turbulence. Second edition. Madyam R. M. Ed. New York
- Unadkat H., Rielly C. D., Hargrave G. K., Nagy Z. K. 2009. Application of fluorescent PIV and digital image analysis to measure turbulence properties of solid-liquid stirred suspensions. *Chem. Eng. Res. Des.* 87: 573-586
- Vakili M. H., Esfahany M. N. 2009. CFD analysis of turbulence in a baffled stirred tank, a three-compartment model. *Chem. Eng. Sci.* 64: 351-362
- Vankova N., Tcholakova S., Denkov N. D., Ivanov I. B., Vulchev V. D., Danner T. 2007. Emulsification in turbulent flow. 1. Mean and maximum drop diameters in inertial and viscous regimes. *J. Colloid Interface Sci.* 312: 363-380
- Van den berg T. H., Luther S., Mazzitelli I. M., Rensen J. M., Toschi F. Lohse D. 2006. Turbulent bubbly flow. *J. Turbulence.* 7: 1-12
- Villermaux J. 1988. The role of energy dissipation in contacting and mixing devices. *Chem. Eng. Technol.* 11: 276-287
- Wang C. Y. Calabrese R. V. 1986. Drop breakup in turbulent stirred-tank contactors. *AIChE J.* 32: 667- 1986
- Warmoeskerken, M. M. C. G., Smith, J. M., 1985. Flooding of disc-turbines in gas-liquid dispersions: a new description of the phenomenon. *Chem. Eng. Sci.* 40: 2063–2071
- Wu J. 1995. Mechanisms of animal cell damage associated with gas bubbles and cell protection by medium additives. *J. Biotechnol.* 43 : 81-94
- Wu J. Z, Ma H. Y., Zhou M. D. 2006. *Vorticity and vortex dynamics*. Springer-Verlag Berlin Heidelberg. Germany. P. 71
- Xinhong L., Yuyun B., Zhipeng L., Zhengming G., Smith J. M. 2008. *Chinese J. Chem. Eng.* 16: 700-708
- Yang N. S., Shen Z. Q. 1986. Pressure drop, gas holdup, and interfacial area for gas-liquid contact in Karr columns. *Ind. Eng. Chem. Process Des. Dev.* 25: 660-664

- Yarin A. L. 1997. On the mechanism of turbulent drag reduction in dilute polymer solutions: dynamics of vortex filaments. *J. Non-Newtonian Fluid Mech.* 69: 137-153
- Yeoh S. L., Papadakis G., Yianneskis M. 2005. Determination of mixing time and degree of homogeneity in stirred vessels with large eddy simulation. *Chem. Eng. Sci.* 60: 2293- 2302
- Yoon H. S., Balachandar S., Ha M. Y., Kar K. 2003. Large eddy simulation of flow in a stirred tank. *J. Fluids Eng.* 125: 486-499
- Zalc J. M., Szalai E. S., Alvarez M. M., Muzzio F. J. 2002. Using CFD to understand chaotic mixing in laminar stirred tanks. *Fluid Mechanics Transport Phenomena.* 48: 2124-2133
- Zamankhan P. 2010. Large Eddy simulation and PIV experiments of air-water mixing tanks. *Commun Nonlinear Sci. Numer. Simulat.* 15: 1511–1525
- Zhao M., Niranjani K., Davidson J. F. 1994. Mass transfer to viscous liquids in bubble columns and air-lift bioreactors: influence of baffles. *Chem. Eng. Sci.* 49: 2359-2369
- Zhou G., Kresta S. M. 1998a. Correlation of mean drop size and minimum drop size with the turbulence energy dissipation and the flow in an agitated tank. *Chem. Eng. Sci.* 53: 2063-2079
- Zhou G., Kresta S. M. 1998b. Evolution of drop size distribution in liquid-liquid dispersion for various impellers. *Chem. Eng. Sci.* 53: 2099-2113
- Zieverink M. M. P., Kreutzer M. T., Kapteijn F., Moulijn J. A. 2006. Gas-liquid mass transfer in bench scale stirred tanks-fluid properties and critical impeller speed for gas induction. *Ind. Eng. Chem. Res.* 45: 4574-4581
- Zlokarnik M. 2001. *Stirring, theory and practice.* Wiley-VCH. Germany. pp 126-205, 244-271

# APPENDIX

## A-1 MatLab programs

### 1. Algorithm to process the drops diameter

```

%% Algorithm to process the drops diameter
% drops were measured using Image-Pro® Plus V. 5.2
(Media Cybernetics, USA)
%
%           Last modified: 24 August 2011
%
%% Processing drops
%Program to plot the individual diameters and
velocity vectors

% This section is to process drops radius
clear all
load('oillrpm300.mat');
    %this file contains x,y,area, lengt and
radius
xyr=unnamed(:, [1:2,5]); % only x y and radius
q=size(xyr);           % lengths of rows and
columns
datos=q(1);           % the number of data

% Estimation of error between the radius of the same
drop
m=1; n=1; b=[]; % b => indicates where error is
greater than 35%
for i=1:2:datos;
    j=i+1;
    a(m)=abs((xyr(i,3)-xyr(j,3))/(xyr(i,3)));
    if a(m)>0.30; b(n,1)=i; n=n+1;
    else n=n;
    end
    m=m+1;
end
clear m n a q i j datos
%% This section eliminates false measurements
n=length(b);
xyrbis=xyr;

for i=n:-1:1;
    k=b(i);
    xyrbis(k+1,:)=[];
    xyrbis(k,:)=[];
end

q=size(xyrbis);
datos=q(1);

% Estimation of error between the radius of the same
drop
m=1; n=1; b=[]; % b => indicates where error is
greater than 30%
for i=1:2:datos;
    j=i+1;
    a(m)=abs((xyrbis(i,3)-
xyrbis(j,3))/(xyrbis(i,3)));
    if a(m)>0.30; b(n,1)=i; n=n+1;
    else n=n;
    end
    m=m+1;
end

clear i n m xyr
% This section eliminates those diameters with
errors greater than 30%
m=length(xyrbis);
n=1;
for i=1:2:m;
    xyr(n, [1:2])=xyrbis(i, [1:2]);
    xyr(n,3)=(xyrbis(i,3)+xyrbis(i+1,3))/2;
    % this file contains x y and the average of
radius
    n=n+1;

end
clear m n a b q i j k datos

%% This section plots diameters of drops along the
images sequence

a=size(xyr);
values=0:0.001:10;

figure('Color',[1 1 1]);
for i=1:(a(1)) %This cycle plots the individual
drops
r= xyr(i,3);
xa=r*cos(pi*values); yb=r*sin(pi*values);
%plot((xyr(i,1)+xa), (xyr(i,2)+yb), 'k', 'Color',[0 0
0], 'LineWidth',2)

i=i+1;
axis square
hold on
end
box('on');
hold('all');
clear a i r xa xb yb values

%% Plot the PDF vs diameter
d=2*xyr(:,3)./1000; %drops diameter in mm
clear var
var=d;
clear X; clear Y;
X=min(var):0.001:max(var); X=X'; %
rango de la variable
Y=normpdf(X,mean(var),std(var)); %
calcula la PDF
figure
%plot(X,Y,'k') % grafica pdf
vs la variable
%% estimates d32
d(:,2)=d(:,1).^3; d(:,3)=d(:,1).^2;
d32=sum(d(:,2))/(sum(d(:,3)))

%% This section prepares the vectors vx and vy
%Estimates vx en m/s
t=1/5130; % difference time between frames
q=length(xyrbis);
m=1;
for i=1:2:q;
    j=i+1;
    vx(m)=(xyrbis(j,1)-xyrbis(i,1))/t/1000000;
%units: m/s
    m=m+1;
end
%plot(vx)
clear m i j

%Estimates vy en m/s
m=1;
for i=1:2:q;
    j=i+1;
    vy(m)=(xyrbis(j,2)-xyrbis(i,2))/t/1000000;
%units: m/s
    m=m+1;
end
clear m i j
x=xyr(:,1); y=xyr(:,2);
quiver(x,y,vx,-vy,'r','LineWidth',1) %Quiver
plot of vectors vx and vy
clear xyrbis q t
%% This section estimates the magnitud of v
v=sqrt(vx.^2+vy.^2);
v=v';
max(v);

```



```

%% Plot the PDF vs velocity
var=v;
clear X; clear Y;
X=min(var):0.001:max(var); % rango de la
variable

```

```

Y=normpdf(X,mean(var),std(var)); % calcula la
PDF
plot(X,Y,'r') % grafica pdf
vs la variable

```

## 2. Algorithm to study the flow field

```

% Algorithm to study the flow field
% Last Modified: August 2th 2011
%
%
%% Load the file and define properties
% The file contains x z positions vx and vz
clear all

% C:\Users\Rene\Documents\Proyecto Doc\TESIS\Matlab
load xyuvstd300rpm

%ro=1000; mu=1e-3; po=101e3; % water density,
water viscosity power????

%% Prepare the vector field (using the quiver
function)

clear x y u v dsu dsv y1 y2 x1 x2 b

unnamed=xyuvstd300rpm;
x=reshape (unnamed(:,1),62,62); y=reshape
(unnamed(:,2),62,62);
u=reshape (unnamed(:,3),62,62); v=reshape
(unnamed(:,4),62,62);
dsu=reshape (unnamed(:,5),62,62);
dsv=reshape (unnamed(:,6),62,62);

clear xyuvstd300rpm unnamed

y1=6; y2=58;
%y1=6; y2=44;
x1=3; x2=36;

b=(x2:-1:x1);
x=x(b,y1:y2)'; y=y(x1:x2,y1:y2)';
u=-u(x1:x2,y1:y2)'; v=v(x1:x2,y1:y2)';
dsu=-dsu(x1:x2,y1:y2)'; dsv=dsv(x1:x2,y1:y2)';

clear x1 x2 y1 y2 b

%% plot the velocity
vel=sqrt(u.^2+v.^2);
velfluct=sqrt(dsu.^2+dsv.^2);
contourf(x,y,vel,20)
hold on
quiver(x,y,u,v,'k','AutoScaleFactor',6)
axis square off
title 'vel'
colorbar

% plot the velocity fluctuation
figure
contourf(x,y,velfluct,20)
hold on
quiver(x,y,u,v,'k','AutoScaleFactor',6)
axis square off
colorbar
title 'velfluct'
%print -dtiff vectorfield

%% zoom in in the impeller discharge

y7=4; y8=28;
x7=12; x8=33;
figure
xzoom=x(x7:x8,y7:y8); yzoom=y(x7:x8,y7:y8);

```

```

uzoom=u(x7:x8,y7:y8); vzoom=v(x7:x8,y7:y8);
dsuzoom=dsu(x7:x8,y7:y8); dsvzoom=dsv(x7:x8,y7:y8);

clear x7 x8 y7 y8

% plot the velocity in the zoomed area
hold on
vel=sqrt(uzoom.^2+vzoom.^2);
contourf(xzoom,yzoom,vel,20)
quiver(xzoom,yzoom,uzoom,vzoom,'k','AutoScaleFactor',2)
colorbar
title 'vel_zoom'

% plot the velocity fluctuation in the zoomed area
figure
velfluct=sqrt(dsuzoom.^2+dsvzoom.^2);
contourf(xzoom,yzoom,velfluct,20)
hold on
quiver(xzoom,yzoom,uzoom,vzoom,'k','AutoScaleFactor',2)
colorbar
title 'vel_fluct_zoom'

clear y7 x7 y8 x8 x y u v dsu dsv
%print -dtiff zoomvectorfield
%% Kinetic energy (ke) in the zoomed area

ke=3/4*(dsuzoom.^2+dsvzoom.^2);
figure
contourf(xzoom,yzoom,ke,30)
colormap summer
title 'ke'

hold on
quiver(xzoom,yzoom,uzoom,vzoom,'w','AutoScaleFactor',2)
colorbar
%('peer',axes1,'LineWidth',1,'FontWeight','light',...
.
% 'FontUnits','centimeters',...
% 'FontSize',0.8,'FontName','times');
axis square
axis off

%% Energy dissipation rate (edr) in the zoomed area

clear A L edr edrbis
A=1; L=0.07/10;
edr=(velfluct.^3).*(A/L);
figure
contourf(xzoom,yzoom,edr,30)
colormap summer
title 'edr'

hold on
quiver(xzoom,yzoom,uzoom,vzoom,'w','AutoScaleFactor',2)
colorbar
%('peer',axes1,'LineWidth',1,'FontWeight','light',...
.
% 'FontUnits','centimeters',...
% 'FontSize',0.8,'FontName','times');
axis square
axis off

clear A L

```

### 3. Algorithm to prepare the PDF function for the bubbles or drops diameter

```
%% Algorithm to prepare the PDF function for the bubbles or drops diameter
%
%'      Last modification: August 24th, 2011
%
%%
% C:\Users\Rene\Documents\Proyecto Doc\TESIS\Matlab
load airbubbles.mat % This file contains the bubbles diameters
%                   300 rpm full vision
%
%% This section estimates and plots the PDF function vs the bubbles diameter
var=b(:,1);
X=min(var):0.01:max(var); % rango de la variable
Y=normpdf(X,mean(var),std(var)); % calcula la PDF
hold on
plot(X,Y,'-b') % grafica pdf vs la variable
mean(var)
std(var)
%clear X Y
```

## A-2 Statistical tools

The mean ( $\bar{x}$ ) of a data set is defined by Eq. A.1 (Ramachandran and Tsokos 2009). Considering that  $n$  is the number of elements, then

$$\bar{x} = \frac{1}{n} \sum_{i=1}^n x_i \quad (\text{A.1})$$

The variance ( $\sigma^2$ ) is defined as (Ramachandran and Tsokos 2009):

$$\sigma^2 = \left( \frac{1}{n-1} \sum_{i=1}^n (x_i - \bar{x})^2 \right) \quad (\text{A.2})$$

The standard deviation ( $\sigma$ ) was computed as (Ramachandran and Tsokos 2009)

$$\sigma = \left( \frac{1}{n-1} \sum_{i=1}^n (x_i - \bar{x})^2 \right)^{\frac{1}{2}} \quad (\text{A.3})$$

But some authors use

$$\sigma = \left( \frac{1}{n} \sum_{i=1}^n (x_i - \bar{x})^2 \right)^{\frac{1}{2}} \quad (\text{A.4})$$

The single difference between A.3 and A.4 is the factor  $n - 1$ .

The average deviation ( $\bar{\sigma}$ ) (Ramachandran and Tsokos 2009):

$$\bar{\sigma} = \frac{1}{n} \sum_{i=1}^n |x_i - \bar{x}| \quad (\text{A.5})$$

### References for this section:

- Mathieu J., Scott J. 2000. An introduction to turbulent flow. Cambridge University press. USA.  
P. 51
- Ramachandran L. M., Tsokos C. P. 2009. *Mathematical statistics with applications*. Academic Press. USA.

## A-1 Published work

ASIA-PACIFIC JOURNAL OF CHEMICAL ENGINEERING  
*Asia-Pac. J. Chem. Eng.* 2011; 6: 181–193  
 Published online in Wiley Online Library  
 (wileyonlinelibrary.com) DOI:10.1002/apj.537



Special Theme Research Article

## CFD investigation of new helical ribbon mixers bottom shapes to improve pumping

Rene Sanjuan-Galindo,<sup>1</sup> Mourad Heniche,<sup>2\*</sup> Gabriel Ascanio<sup>1</sup> and Philippe A. Tanguy<sup>2</sup>

<sup>1</sup>Centro de Ciencias Aplicadas y Desarrollo Tecnológico, Universidad Nacional Autónoma de México, México D.F. 04510, Mexico

<sup>2</sup>URPEI, Department of Chemical Engineering, École Polytechnique de Montréal, Montreal, Quebec H3C 3A7, Canada

Received 27 October 2009; Revised 12 November 2010; Accepted 14 November 2010

**ABSTRACT:** It is well known that helical ribbon (HR) impellers exhibit poor bottom pumping properties. Three different HR impeller geometries, varying in their bottom design, are compared in terms of their mixing performance. Particular emphasis is given to the improvement of pumping capabilities. The selected bottom geometries were a standard bottom termination, an anchor-type termination and a paddle-type termination. The investigation was based on the use of 3D finite-element simulation to assess the hydrodynamics and mixing performance using various distributive and dispersive criteria. Analysis of Poincaré maps showed that an HR with a paddle-type termination operating in a down-pumping mode offered the best performance. © 2011 Curtin University of Technology and John Wiley & Sons, Ltd.

**KEYWORDS:** CFD; helical ribbon; paddle bottom; mixing; Poincaré map

### INTRODUCTION

Vessel-based mechanical mixing involving viscous media is an essential operation in industrial sectors such as pharmaceuticals, chemistry, oil and many others. In such processes, the quality of the final product depends on the homogenization obtained, which is a consequence of the operating conditions. This topic has been previously investigated using numerical and experimental methods.<sup>[1–3]</sup>

In practice, the mixing of viscous liquids in stirred tanks is often done using close-clearance impellers such as helical ribbons (HRs). Although open impellers are sometimes used for the agitation of moderately viscous fluids (less than a few tens of Pascal seconds), macromixing with HR-type impellers is well accepted even if the lower side of the mixing vessel is prone to spurious flow phenomena, such as segregated and compartmentalized regions, as a consequence of the low pumping capacity.

The available literature investigating the HR mixing performance is quite diverse. The geometrical features of the HR are one of the most studied aspects: single ribbon, double ribbon, impellers with or without an inner

screw fixed along the central shaft, even used in flat-bottom cylindrical tanks or in dished-bottom tanks, have all been analyzed in previous works.<sup>[4,5]</sup> Beckner and Smith<sup>[6]</sup> and Brito-de la Fuente *et al.*<sup>[7]</sup> have reported on the power drawn for HR agitating both Newtonian and non-Newtonian liquids. Delaplace *et al.*<sup>[8]</sup> provided a detailed description of the application of HR in industrial processes, emphasizing the effects that geometrical parameters, such as the number of ribbons, pitch size ( $p$ ), blade width ( $w$ ) or bottom/wall clearance, have on the circulation and mixing times.

Experimental studies of macroscopic parameters for small mixing volumes (<75 L) have been the main topic of many published reports, including both Newtonian and non-Newtonian fluids.<sup>[1,7–11]</sup>

From the perspective of numerical analysis, one of the pioneering CFD works focused on the mixing performance of HR impellers in cylindrical vessels is the contribution made by Tanguy *et al.*<sup>[2]</sup> They developed a three-dimensional model (validated experimentally) based on the finite-element method for the analysis of an HR-screw impeller. The authors reported good liquid circulation at low impeller speeds (10 rpm) and showed evidence of poor pumping in the vessel bottom. They noticed that the segregation increased upon increasing the impeller speed. In subsequent numerical works developed for diverse HR geometries and fluids of several rheological behaviors, Rauline *et al.*<sup>[12]</sup> and

\*Correspondence to: Mourad Heniche, URPEI, Department of Chemical Engineering, École Polytechnique de Montréal, Montreal, Quebec H3C 3A7, Canada. E-mail: mourad.heniche@polymtl.ca



ELSEVIER

Contents lists available at ScienceDirect

Chemical Engineering Research and Design

IChemE

journal homepage: [www.elsevier.com/locate/cherd](http://www.elsevier.com/locate/cherd)

## High-speed visualization of multiphase dispersions in a mixing tank

Eliane Guevara-López<sup>a</sup>, René Sanjuan-Galindo<sup>b</sup>, Ma. Soledad Córdova-Aguilar<sup>a</sup>, Gabriel Corkidi<sup>a</sup>, Gabriel Ascanio<sup>b</sup>, Enrique Galindo<sup>a,\*</sup>

<sup>a</sup> Instituto de Biotecnología, Universidad Nacional Autónoma de México, Apdo. Postal 510-3, 62250 Cuernavaca, Mor., Mexico

<sup>b</sup> Centro de Ciencias Aplicadas y Desarrollo Tecnológico, Universidad Nacional Autónoma de México, Apdo. Postal 70-186, 04510 México D.F., Mexico

### ABSTRACT

A high-speed video system was used for studying multiphase dispersions by image analysis. A high-speed video camera, coupled to a stereomicroscope was used to record the dispersion occurring in a mixing tank. A high intensity direct light probe submerged in the liquid was used for illumination. Sequences of 200 images (512 × 384 pixels) at rates up to 5130 frames/s (fps) and magnification up to 11× were obtained and analyzed. A detailed observation of the mixing dynamics at a high video rate allowed visualizing how oil drops and air bubbles move and interact. Velocity of the objects could be calculated at different focal planes. Rotational movement and trajectories in different directions, depending on the physicochemical properties of the system could be observed and recorded. The implemented methods also allowed the recording of the deformation of complex drops and were useful to discern situations of inclusions of objects (i.e. bubbles inside oil drops) in multiphase dispersions under power inputs up to 0.50 kW/m<sup>3</sup>.

© 2008 The Institution of Chemical Engineers. Published by Elsevier B.V. All rights reserved.

**Keywords:** High-speed video; Multiphase dispersion; Drop and bubble trajectories

### 1. Introduction

Two or more phases (gas–liquid, immiscible liquid–liquid and solid–liquid dispersions) are involved extensively in the chemical, biochemical, petroleum, mining, pulp and paper industries (Leng and Calabrese, 2004), as well as in other industrial processes which carry out oxidations, hydrogenations and aerobic fermentations (Paul et al., 2004). The gas and the immiscible liquid are present in the form of small bubbles and drops to yield a large surface area, as well as to improve the mass transfer efficiency, which is a key parameter for the successful performance of the process. The composition of the dispersion and the operational parameters of the bioreactor control the coalescence-breakup events (Lagisetty et al., 1986) and hence they determine the size distribution of drops and bubbles (Leng and Calabrese, 2004).

Image analysis techniques are valuable tools that can provide insights of interesting hydrodynamic phenomena occurring in multiphase systems, since these techniques have

allowed the observation of phase interactions resulting in complex structures (e.g. inclusion of air bubbles and aqueous droplets inside oil drops) (Larralde-Corona et al., 2002), phenomena not evidenced with studies focused only in the hydrodynamics or even with non-high-speed visualization techniques. This is why the use of high-speed camera systems to evaluate dispersion processes by image analysis has been recently reported (Lovick et al., 2005). However, the experiments performed have been limited to characterize two-phase systems.

Our research group has been working with image analysis systems for the characterization of complex multiphase dispersions, using as a model system a fungal fermentation process that produces natural aroma compounds (e.g. coconut and peach) (Serrano-Carreón et al., 1997). The image analysis system used in previous works (Galindo et al., 2005) consisted of a 30 fps-CCD (frames/s, charge-coupled device) camera adapted to a stereomicroscope and a high-energy stroboscope lamp which feeds a submergible light probe placed

\* Corresponding author. Tel.: +52 55 56227651.

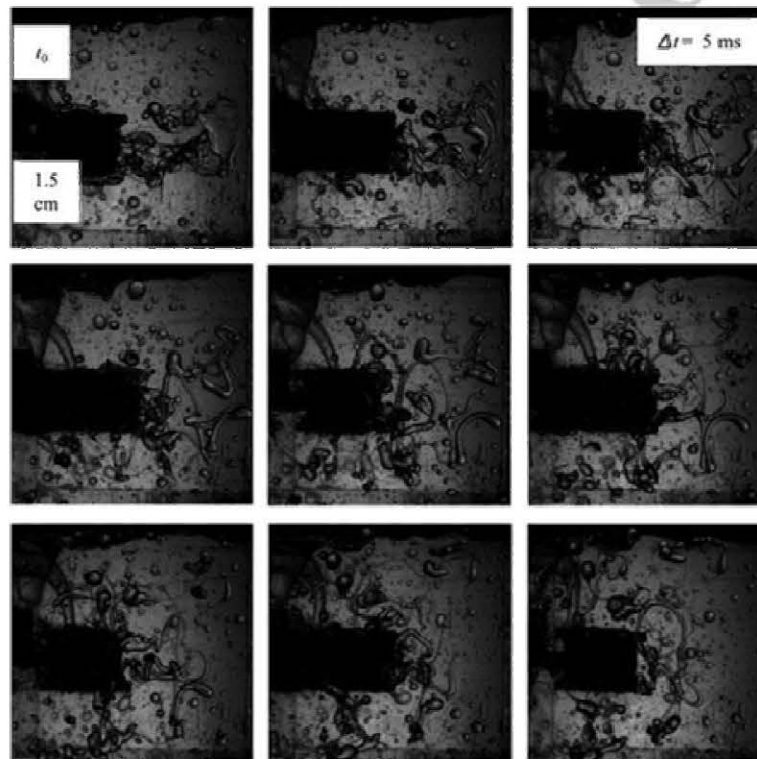
E-mail address: [galindo@ibt.unam.mx](mailto:galindo@ibt.unam.mx) (E. Galindo).

Received 28 July 2008; Accepted 29 July 2008



# 1 Oil Filaments Produced in a Stirred Tank

2 Rene Sanjuan-Galindo, Enrique Soto, Gabriel Ascanio  
3 and Roberto Zenit



R. Sanjuan-Galindo · E. Soto · G. Ascanio  
Centro de Ciencias Aplicadas y Desarrollo Tecnológico, Universidad Nacional  
Autónoma de México, Apdo. Postal 70-186, 04510 México City, D.F., México

R. Zenit (✉)  
Instituto de Investigaciones en Materiales, Universidad Nacional Autónoma  
de México, Apdo. Postal 70-360, 04510 México City, D.F., México  
e-mail: zenit@servidor.unam.mx

J. Klapp et al. (eds.), *Experimental and Theoretical Advances in Fluid Dynamics*,  
Environmental Science and Engineering, DOI: 10.1007/978-3-642-17958-7\_51,  
© Springer-Verlag Berlin Heidelberg 2011

1



### USO DE VIDEO DE ALTA VELOCIDAD PARA ENTENDER LA FORMACIÓN Y DINÁMICA DE ESTRUCTURAS MULTIFÁSICAS EN TANQUES DE MEZCLADO

Enrique Galindo, Alfonso Rojas, René Sanjuan, María Soledad Córdova\*, y Gabriel Corkidi  
Instituto de Biotecnología -UNAM, Apdo. Postal 510-3, Cuernavaca, Morelos, 62250, México. fax:  
(777)3138811, email: [cordova@ibt.unam.mx](mailto:cordova@ibt.unam.mx)

Palabras clave: *análisis de imágenes, dispersión, gotas, burbujas*

**Introducción.** Nuestro grupo de investigación ha trabajado desde hace varios años en el diseño y aplicación de metodologías de análisis de imágenes para la caracterización cuantitativa y dinámica de las dispersiones que ocurren dentro de un sistema modelo multifásico (1). De esta manera, se ha podido visualizar la presencia de gotas multifásicas (burbujas y pequeñas gotas de la fase acuosa, dentro de las gotas de aceite), lo que implica fenómenos complejos de transferencia de masa (1).

El objetivo del presente trabajo es presentar nuevos enfoques experimentales implementados en nuestro laboratorio para estudiar detalladamente la formación y el movimiento de las estructuras complejas en sistemas modelo multifásicos.

**Metodología.** Se adquirieron videos con una cámara de alta velocidad (Motion Pro HS-4, Redlake, USA) utilizando los diferentes arreglos experimentales presentados previamente (1, 3). La caracterización dinámica de la dispersión se realizó siguiendo la metodología reportada en (2), con el medio de cultivo para *Trichoderma harzianum* (1) como fase dispersa y 0.25 vvm de aire, así como una solución de 0.6 % w/v carboximetilcelulosa como sistema no Newtoniano. La observación de los mecanismos de formación de estructuras, se hizo de acuerdo a la metodología reportada en (3), modificando la tensión superficial de algunos sistemas con 0.2 g/L de BSA. La distribución de tamaños y las trayectorias de gotas de aceite y burbujas de aire se determinaron con las herramientas del programa Image-Pro Plus v.5.1 (Media Cybernetics, USA) (1, 2).

**Resultados y discusión.** En el sistema Newtoniano se visualizó que los objetos se mueven en diferentes direcciones (*figura 1a*), calculándose una velocidad promedio de 27 cm/s. En el sistema no-Newtoniano, las gotas mostraron un movimiento lineal con inclinación de  $-22^\circ$  con respecto al eje vertical. Las velocidades fueron menores con respecto al sistema Newtoniano y los objetos del primer plano (enfocados) se mueven más lentamente que los del fondo (no enfocados) (*figura 1b*). En otro ensayo se visualizó que las gotas de aceite se deforman por impacto al entrar en el agua y tocar fondo y cuando recuperan su forma esférica dentro del agua, incorporan gotas de agua en su interior, siendo éste uno de los mecanismos probables que contribuyen a la formación de estructuras multifásicas en el tanque de mezclado (*figura 2*) ya que este tipo de deformación

puede ocurrir al chocar las gotas con las paletas del impulsor. Las burbujas de aire pueden introducirse en las gotas de aceite por contacto y coalescencia entre gotas y burbujas (*datos no mostrados*).

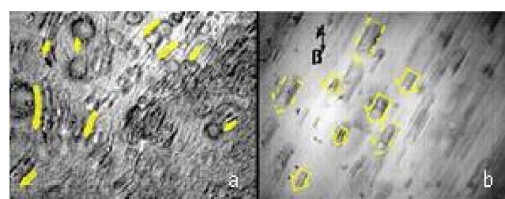


Fig. 1. Trayectorias de estructuras: a) Sistema Newtoniano; b) Sistema no Newtoniano

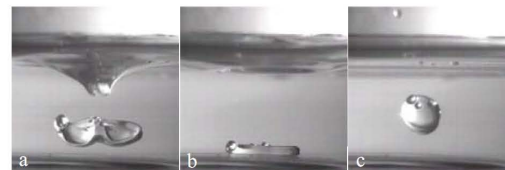


Fig. 2. Gota de aceite deformada e inclusión de la fase continua.

**Conclusiones.** Utilizando video de alta velocidad se visualizó la forma en que las gotas de aceite y las burbujas de aire se mueven e interactúan. La velocidad y trayectoria de estos objetos se pueden calcular en los diferentes planos de enfoque, las cuales varían dependiendo de las propiedades fisicoquímicas del sistema. Las pequeñas gotas de agua dentro de las gotas de aceite se introducen por impacto y deformación, mientras que en algunos casos la presencia de burbujas se debe al contacto y coalescencia.

**Agradecimiento.** Apoyo financiero de CONACyT (proyecto 59807).

#### Bibliografía.

- Galindo, E., Larralde, P., Brito, T., Córdova, M.S., Taboada, B., Vega, L. y Corkidi, G. (2005) Development of advanced image-analysis techniques for the *in situ* characterization of multiphase dispersions occurring in bioreactors. *J. Biotechnol.* 116: 261-270.
- Guevara-López, E., Sanjuan-Galindo, R., Córdova-Aguilar, M.S., Corkidi, G., Ascanio, G. y Galindo, E. (2008) High-speed visualization of multiphase dispersions in a mixing tank. *Chem Eng. Res. Des.* 86: 1382-1387.
- Corkidi, G., Rojas, A., Córdova-Aguilar, M.S., Pimentel, A. y Galindo, E. (2009) Visualization of complex drop formation in multiphase fermentations. *Sometido al 8th World Congress of Chemical Engineering*, Montreal, 23 – 27 de Agosto, 2009.



**SOMI**XXIV  
Congreso de Instrumentación

La Sociedad Mexicana de Instrumentación

Otorga la presente



Mérida Yucatan, México, Octubre 2009

# CONSTANCIA

a: Rene Sanjuan Galindo, Gabriel Ascanio Gasca, Roberto Zenit Camacho

Por haber presentado en el Congreso de Instrumentación SOMI XXIV su trabajo:

**Determinación por PIV del Flujo Producido en un Sistema Tanque-Impulsor Scaba a Diferentes Números de Reynolds**



Dr. José Manuel Sanjer Blesa  
PRESIDENTE



Dr. Gabriel Ascanio Gasca  
SECRETARIO EJECUTIVO







American Physical Society Sites: [APS](#) [Journals](#) [PhysicsCentral](#) [Physics](#) [Focus](#)

<http://www.aps.org/units/dfd/pressroom/gallery/zenit10b.cfm>

Search

## Division of Fluid Dynamics

Governance

Newsletters

Meetings

News & Announcements

Education & Outreach

APS Fellowship

Prizes & Awards

**Virtual Press Room**

Press Releases

Image Gallery

Video Gallery

Information for Journalists

Lay Language Papers

Virtual Press Room Archive

Fluid Dynamics Video

Image Gallery

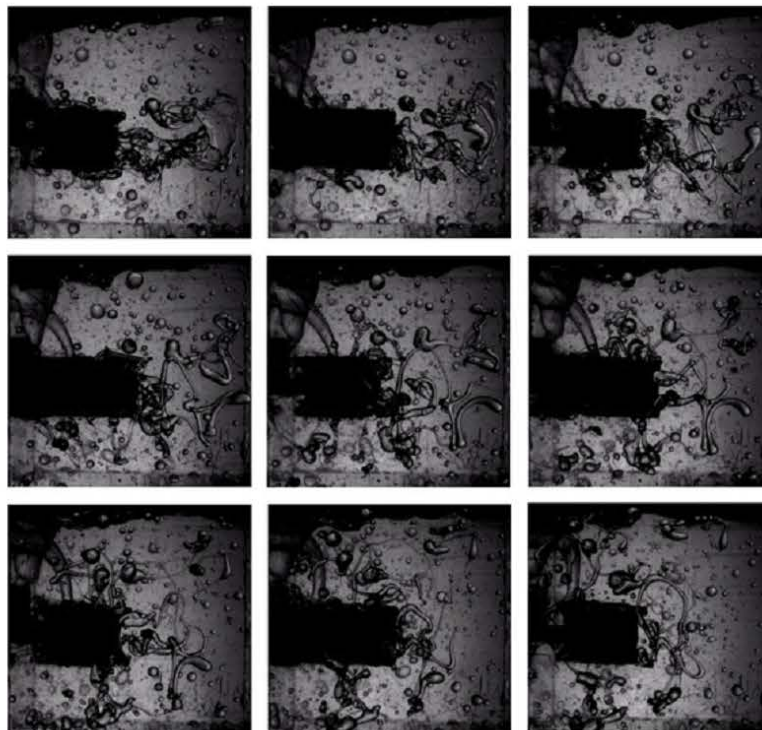
Resources

[DFD Home](#) | [Virtual Press Room](#) | [Image Gallery](#) | [Making Emulsions](#)

### Making Emulsions

**Rene Sanjuan-Galindo**  
**Enrique Soto, Gabriel Ascanio**  
**Roberto Zenit**  
 Universidad Nacional Autonoma de Mexico

Email Print Share



In these images we show the process through which an emulsion is formed. An emulsion is a mixture of liquid drops suspended in another liquid.

In the process to disperse a viscous oil in water in a stirred tank, filaments are produced before droplets became formed. The impeller blades drive the oil and pushed it radially into the liquid bulk. In this step, filaments suffer elongation due to the fluid forces that make them thinner. This set of photographs were obtained using a high speed camera, it can be noticed that filaments are highly unstable and easily deformed, what induces that breakage occurs unexpectedly. The broken filaments recoil at the time they are dispersed and finally droplets are produced.

#### Reporters and Editors

Reporters may freely use this image. **Credit: Universidad Nacional Autonoma de Mexico (UNAM) (2010).**